

# **Application of Oxygen Isotope to the Studies of Hydrothermal Mineral Deposits**

**March 2020**

**Luvsannyam OYUNJARGAL**

# **Application of Oxygen Isotope to the Studies of Hydrothermal Mineral Deposits**

A Dissertation Submitted to  
the Graduated School of Life and Environmental Sciences,  
the University of Tsukuba  
in Partial Fulfillment of the Requirements  
for the Degree of Doctor of Philosophy in Science  
(Doctoral Program in Earth Evolution Sciences)

**Luvannyam OYUNJARGAL**

## Table of Contents

Table of contents.....	i
Abstract.....	iii
List of figures.....	vi
List of tables.....	viii
Chapter 1. Introduction .....	1
Chapter 2: Geological, Mineralogical, and Oxygen Isotope Studies of the Chandmani Uul Iron Oxide–Copper–Gold (IOCG) Deposit in Dornogobi Province, Southeastern Mongolia.....	3
1. Introduction .....	3
2. Outline of geology and the ore deposit .....	5
2.1. Geological background.....	5
2.2. Alteration and mineralization .....	8
2.2.1 Wall rock alteration .....	8
2.2.2 Mineralization.....	12
3. Samples and analytical methods .....	17
3.1. Geochemistry of granitic rocks .....	18
3.2. Zircon U-Pb analyses .....	18
3.3. Electron Probe Micro Analyses.....	19
4.4. Oxygen isotope analyses of minerals .....	19
4. Analytical results.....	21
4.1 Major elements and trace elements of granitic rocks .....	21
4.2. Zircon U-Pb ages.....	24
4.3. Magnetite chemistry .....	29
4.4. Oxygen Isotope.....	31
5. Discussion .....	32
5.1. Oxygen isotope geothermometry of iron oxide ore.....	32
5.2. Source of ore-forming fluid.....	34

5.3. Comparison with other IOCG deposits .....	37
5.3.1. Tectonic setting and related igneous rocks.....	38
5.3.2. Wall rock alteration .....	39
5.3.4. Source of ore-forming fluid.....	42
6.Conclusions .....	43
Chapter 3: Oxygen Isotopic Study on the Date-Nagai Skarn-Type Tungsten	
Deposit, Northeastern Japan .....	45
1.Introduction .....	45
2.Geology .....	46
3.Ore deposit .....	48
3.1. Occurrence of skarn.....	49
3.2. Occurrence of scheelite .....	52
4.Chemical compositions of skarn minerals .....	54
5.Oxygen isotope.....	56
6.Discussion .....	58
6.1. Oxygen isotope value of skarn-forming fluid .....	58
6.2. Source of ore-forming fluid.....	60
7.Conclusions .....	62
Chapter 4: Summary and conclusions .....	63
Acknowledgments .....	64
References	67
Appendix I: Analytical data.....	83

## Abstract

This research focuses on the oxygen isotope study of the Chandmani Uul IOCG and the Date-Nagai W-skarn deposits in order to discuss origins of ore-forming fluids.

The Chandmani Uul deposit is located in Dornogovi province, southeastern Mongolia. Iron oxide ores are hosted in the andesitic rocks of the Shar Zeeg Formation of Neoproterozoic to Lower-Cambrian age. Middle- to Upper-Cambrian bodies of granitic rocks have intruded into the host rocks in the western and southern regions of the deposit. The wall rocks around the iron oxide ore bodies were hydrothermally altered to form potassic, epidote, and sericite–chlorite alteration zones, and calcite and quartz veinlets are ubiquitous in the late stage. Since granitic rocks also underwent potassic alteration, the activity of the granitic rocks must have a genetic relation to the ore deposit. The ore mineral assemblage is dominated by iron oxides such as mushketovite, euhedral magnetite with concentric and/or oscillatory zoning textures, and cauliflower magnetite. Lesser amounts of chalcopyrite and pyrite accompany the iron oxides. Among all these products, mushketovite is dominant and is distributed throughout the deposit. Meanwhile, euhedral magnetite appears in limited amounts at relatively shallow levels in the deposit. By contrast cauliflower magnetite appears locally in the deeper parts of the deposit, and is associated with green-colored garnet and calcite. Sulfide minerals are ubiquitously associated with these iron oxides.

The oxygen isotope ( $\delta^{18}\text{O}$ ) values of all types of magnetite, quartz, and epidote were found to be  $-5.9 - -2.8\text{‰}$ ,  $10.5 - 14.9\text{‰}$ , and  $3.6 - 6.6\text{‰}$ , respectively. The

$\delta^{18}\text{O}$  values of quartz–magnetite pairs suggest an equilibrium isotopic temperature near 300°C. The calculated values of  $\delta^{18}\text{O}$  for the water responsible for magnetite ranged from 2 to 10‰. All the data obtained in this study suggest that the iron oxide deposit at the Chandmani Uul is a typical iron oxide–copper–gold deposit, and that this deposit was formed at an intermediate depth with potassic and sericite–chlorite alteration zones under the oxidized conditions of a hematite-stable environment.

The  $\delta^{18}\text{O}$  range estimated implies that the ore-forming fluid was supplied by a crystallizing granodioritic magma exsolving fluids at depth with a significant contribution of meteoric water.

The skarn-type tungsten deposit of the Date-Nagai mine is genetically related to the granodiorite batholith of the Iitateyama body. Skarn develops along the contact between pelitic hornfels and marble that remains as a small roof pendant body directly above the granodiorite batholith.

Zonal arrangement of minerals is observed in skarn. The zonation consists of wollastonite, garnet, garnet-epidote and vesuvianite-garnet zones, from marble to hornfels. Scheelite is accompanied in garnet, garnet-epidote and vesuvianite-garnet zones. The oxygen isotope values of skarn minerals were obtained such as  $\delta^{18}\text{O} = 4.6\text{--}7.7\text{‰}$  for garnet,  $6.1\text{--}7.0\text{‰}$  for vesuvianite,  $0.2\text{--}3.7\text{‰}$  for scheelite,  $6.0\text{--}10.7\text{‰}$  for quartz and  $8.7\text{‰}$  for muscovite, respectively. Temperature of skarn-formation was calculated from oxygen isotopic values of scheelite-quartz pairs to be 288°C.

Calculated oxygen isotope values of fluid responsible for skarn minerals are  $6.1\text{--}9.5\text{‰}$  for garnet,  $1.2\text{--}4.8\text{‰}$  for scheelite,  $-1.3\text{--}3.6\text{‰}$  for quartz and  $4.5\text{‰}$  for muscovite, respectively. Garnet precipitated from the fluids of different  $\delta^{18}\text{O}$  values from scheelite, quartz and muscovite. These  $\delta^{18}\text{O}$  values suggest that origin of fluid

responsible for garnet was magmatic water, while the evidence of the presence of a meteoric component in the fluids responsible for middle to later stage minerals was confirmed.

**Key words:** Oxygen isotope; Hydrothermal deposit; IOCG; W-Skarn; Chandmani Uul; Date-Nagai; Southeastern Mongolia; Northeastern Japan

## List of figures

<b>Figure 1.1</b> Natural oxygen isotope reservoirs. ....	2
<b>Figure 2.1</b> Location of iron deposits in Mongolia from Metallogenic Map of Mongolia.....	4
<b>Figure 2.2</b> Location of the study area. (a) Sketched tectonic map of the CAOB. (b) Tectonic subdivision of southeastern Mongolia .....	6
<b>Figure 2.3</b> Geological map of the Chandmani Uul deposit. (a) Location of the study area. (b) Geology of the area surrounding the Chandmani Uul deposit ....	8
<b>Figure 2.4</b> Map illustrating the cross-sectional distributions of the host rocks and ore bodies.....	9
<b>Figure 2.5</b> Occurrences of hydrothermal alteration zones and magnetite–sulfide ore in andesitic and dioritic host rocks in the 150–234 m interval of drill hole core Z1622, Chandmani Uul deposit. ....	100
<b>Figure 2.6</b> Photomicrographs of common distal and proximal alteration assemblages in the Chandmani Uul deposit .....	111
<b>Figure 2.7</b> Typical ore samples from the Chandmani Uul deposit .....	133
<b>Figure 2.8</b> Photomicrographs showing the characteristic features of the ore assemblages in the Chandmani Uul deposit. ....	155
<b>Figure 2.9</b> Paragenetic sequence during hydrothermal alteration and mineralization at the Chandmani Uul deposit .....	177
<b>Figure 2. 10</b> Geochemical discrimination diagrams and petrochemical data for granitoids from the Chandmani Uul deposit.....	233
<b>Figure 2. 11</b> CL image of representative zircons from the samples. ....	277
<b>Figure 2. 12</b> U–Pb concordia diagrams and age distribution plot of result of LA-ICP-MS measurements of age-known zircon samples from granitoids ..	288
<b>Figure 2. 13</b> Correlations of elements in magnetite from the Chandmani Uul deposit.....	311
<b>Figure 2. 14</b> Oxygen isotope values of minerals from the Chandmani Uul deposit .....	322
<b>Figure 2. 15</b> Oxygen isotope values of water responsible for minerals calculated at 300°C .....	37



<b>Figure 3. 1</b> Geological map of the study area. a) Location of the Date-Nagai deposit in northeastern Japan. b) Regional geological map of the study area. c) Detailed geological map around the Date-Nagai deposit. ....	477
<b>Figure 3. 2</b> a) Underground geological map and b) cross section of the Date-Nagai deposit.....	49
<b>Figure 3. 3</b> Occurrence of skarn zones of the Date-Nagai deposit. ....	50
<b>Figure 3. 4</b> Macrographs of tungsten ores. ....	53
<b>Figure 3. 5</b> Paragenetic sequence of minerals. Thickness of bar indicates relative abundance of minerals. ....	544
<b>Figure 3. 6</b> Chemical compositions of garnet and clinopyroxene. ....	566
<b>Figure 3. 7</b> Oxygen isotope values of garnet, vesuvianite, scheelite, quartz and muscovite.....	588
<b>Figure 3. 8</b> Oxygen isotope values of water responsible for skarn minerals calculated at 288°C.....	611

## List of tables

<b>Table 2.1</b> Major element (in wt.% oxide) concentrations of the granitoids at the Chandmani Uul deposit. ....	83
<b>Table 2.2.</b> Trace element (in ppm) compositions of the granitoids at the Chandmani Uul deposit.....	84
<b>Table 2.3.</b> LA-ICP-MS analyzed data of age-known samples and calculated ages. ....	86
<b>Table 2.4.</b> Chemical composition of magnetite obtained by electron microprobe (EPMA) analyses at the Chandmani Uul deposit (in wt% oxide). ....	96
<b>Table 2.5</b> Oxygen isotope values of minerals and those for ore-forming fluid. .	100
<b>Table 2.6</b> Characteristics of IOCG mineralization of the Chandmani Uul deposit and major IOCG deposits in South America .....	104
<b>Table 3.1</b> Chemical composition of garnet. ....	106
<b>Table 3.2</b> Chemical composition of clinopyroxene. ....	108
<b>Table 3.3</b> Oxygen isotope values for minerals and skarn-forming fluid.....	109

## Chapter 1. Introduction

The oxygen isotope is commonly used in ore deposit studies; when combined with field relationships, petrographic and fluid inclusion studies, they provide information on: temperature of mineral deposition, source of ore-forming fluids, and process and degree of fluid-rock reactions.

There are three stable oxygen isotopes, such as  $^{16}\text{O}$  (99.76%),  $^{17}\text{O}$  (0.04%) and  $^{18}\text{O}$  (0.20%). The isotope ratio  $^{18}\text{O}/^{16}\text{O}$  is normally determined in oxygen isotope studies.  $\delta^{18}\text{O}$  values are calculated as,

$$\delta^{18}\text{O} = [(R_{\text{sample}}/R_{\text{standard}}) - 1] \times 1000 (\text{‰}), \text{ where } R \text{ refers } ^{18}\text{O}/^{16}\text{O}.$$

Vienna-SMOW isotopic standards in use for oxygen isotope measurements.

The fractionation factor is a function of temperature:

$$1000 \ln \alpha = A \times 10^6/T^2 + B \quad (T \text{ in Kelvin}), \text{ where } A \text{ and } B \text{ are constants.}$$

The origin of ore-forming fluids is explored by O isotopic compositions of ore-forming fluids. There are magmatic, meteoric, oceanic, and metamorphic waters in nature, and values of oxygen isotope components of water are described in Fig. 1.1 (Khashgerel, 2010).

I am investigated oxygen isotope analyses on the mineral and rock samples from Chandmani Uul IOCG deposit, on the garnet, scheelite, quartz and muscovite samples from Date-Nagai tungsten-skarn type deposit, respectively.

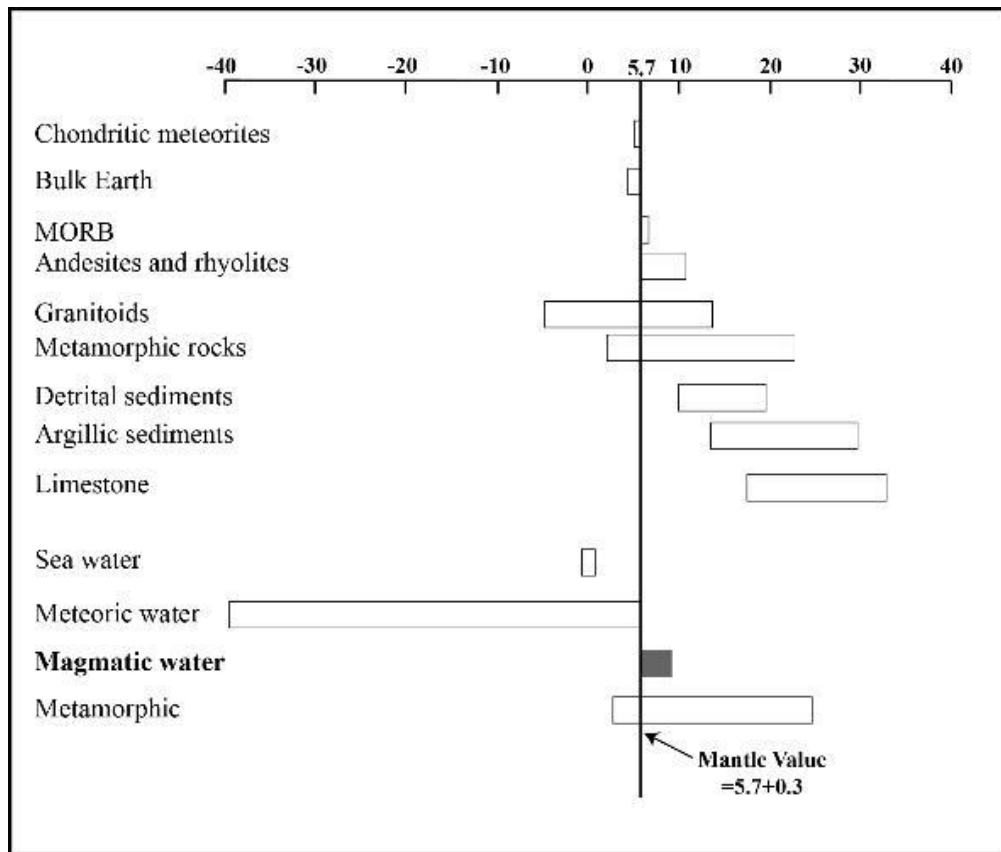


**Fig.1.1** Natural oxygen isotope reservoirs (Ksashgerel., 2010).

## **Chapter 2: Geological, Mineralogical, and Oxygen Isotope Studies of the Chandmani Uul Iron Oxide–Copper–Gold (IOCG) Deposit in Dornogobi Province, Southeastern Mongolia**

### **1. Introduction**

Magnetite ( $\text{Fe}^{2+}\text{Fe}^{3+}_2\text{O}_4$ ) and Hematite ( $\text{Fe}^{3+}_2\text{O}_3$ ) are the most common and abundant oxide in magmatic and metamorphic rocks and is commonly associated with sulphides and gold. Such magnetite or hematite as the major constituents deposits, classified as iron oxide-copper-gold (IOCG) deposits.

IOCG deposits are newly categorized deposit by Hitzman et al. (1992). IOCG deposits are the world's important source of Fe, and are major sources of Cu and Au. IOCG deposit is divided into magnetite IOCG and hematite IOCG subtypes by major iron oxide minerals.

Generally, there are three main alteration zones are recognized on the IOCG deposits. These are: 1) Sodium-Calcium or Sodium alteration, which is characterized by albite (scapolite),  $\pm$  actinolite, magnetite, 2) Potassic alteration, which is introduced by K-feldspar (biotite), magnetite, chlorite, quartz, actinolite, and 3) Sericitic-Chloritic alteration, which is characterized by hematite, sericite, chlorite, carbonate, quartz.

Ukhnaa & Baasan (2016) classified Mongolian iron deposits into 11 provinces (Fig. 2.1) by their geographical location. Several iron-producing metallogenic provinces are known in Mongolia, such as the Tesiin Gol province in western Mongolia, Khentii province in central Mongolia, and Kherlen and Dundgobi provinces in southeastern Mongolia. The iron deposits in these provinces have been

categorized as sedimentary (BIF), metamorphosed sedimentary, and skarn types (Dejidmaa et al., 1996; Ukhnaa & Baasan, 2016). The Chandmani Uul deposit is located in Dundgobi province, about 680 km southeast of Ulaanbaatar and about 210 km from the border with China. The ore reserves of this deposit have been estimated to include 25 Mt of Fe, 1,000 t of Cu, and 3 t of Au (Charlie & Rohan, 2006). Field geological surveys and exploration around this deposit were conducted between 1990 and 2006 by governmental and corporate geologist groups (Charlie & Rohan, 2006), and previous researchers have suggested that this deposit is skarn type in origin (Dejidmaa et al., 1996; Ukhnaa & Baasan, 2016). However, there are no carbonate strata in the host rocks of the iron ore, and minerals that typically appear in skarn deposits, such as wollastonite, clinopyroxene, and garnet, are not present.

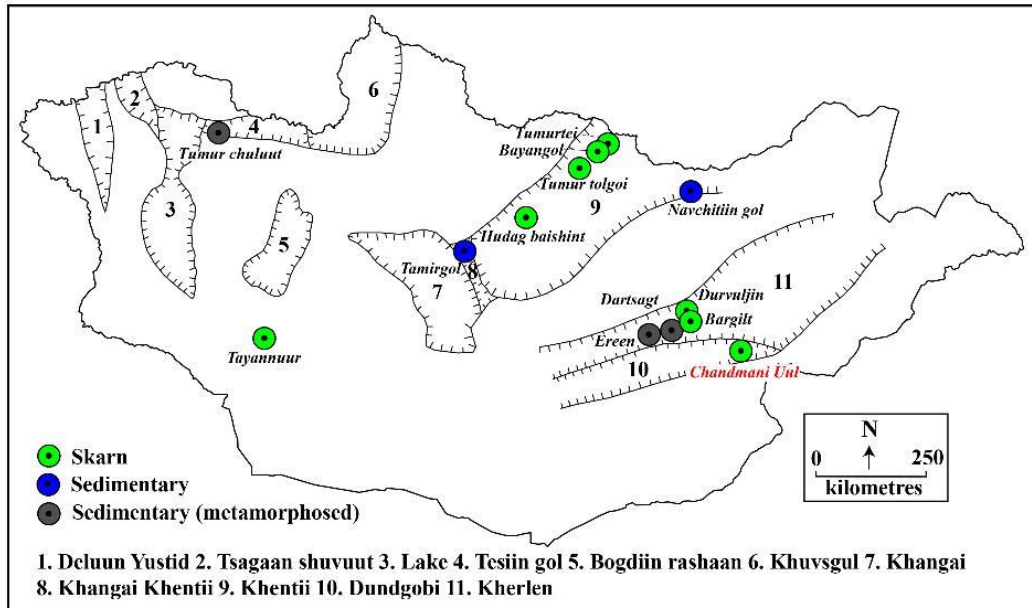


**Fig. 2.1** Location of iron deposits in Mongolia from Metallogenic Map of Mongolia (modified from Dejidmaa et al., 1996; Ukhnaa & Baasan., 2016).

Iron oxide–copper–gold (IOCG) deposits have become a major exploration target and focus for research since their proposal of new idea by Hitzman et al. (1992), and the mineralization style of the Chandmani Uul deposit is similar to those of IOCG deposits. Thus, the geological, mineralogical, and geochemical features of the Chandmani Uul deposit were clarified in this study and compared with those of IOCG deposits worldwide. This is the first report of IOCG-style mineralization in Mongolia and northeastern China to our knowledge.

## **2. Outline of geology and the ore deposit**

### **2.1. Geological background**

Most part of Mongolian geological territory lies within the Central Asian Orogenic Belt (CAOB), one of the largest provinces of Phanerozoic continental growth on Earth. The CAOB is sandwiched between the Precambrian Siberian craton to the north and the Tarim and North China cratons to the south (Fig. 2.2a). The orogen of the CAOB lasted from 600 to 250 Ma (Wilhem et al., 2012), and the CAOB formed by the accretion of Cambrian, Ordovician, and Devonian–Carboniferous arcs, back arcs, accretionary wedges, and Grenville microcontinents (Badarch et al., 2002; Windley et al., 2007; Rojas-Agramonte et al., 2011). The geological territory of Mongolia is subdivided into northern and southern domains, which correspond to Caledonian and Hercynian orogens, respectively. These domains are separated by the so-called Main Mongolian Lineament (MML; Amantov et al., 1970).

The Chandmani Uul deposit is located in the eastern segment of the Siberian craton and at the southern rim of the Idermeg terrane, which is bordered by the MML to the Gobi Altai terrane (Fig. 2.2b). The Idermeg terrane consists primarily of quartzite, conglomerate, sandstone, volcanic pyroclastic rocks, and limestone of Neoproterozoic to Cambrian age (Byamba et al., 1990). The Gobi Altai terrane is a long and narrow belt, located along the northern margin of the southern domain. It consists of greenschist facies metamorphosed sedimentary rocks, sandstone, siltstone, conglomerate, and limestone of Cambrian to Devonian age. The study area is suited near the MML, which is a NE-trending ~10-km-wide fault zone, and blocks of the Idermeg and Gobi Altai terranes appear to be in fault contact (Fig. 2.3b).

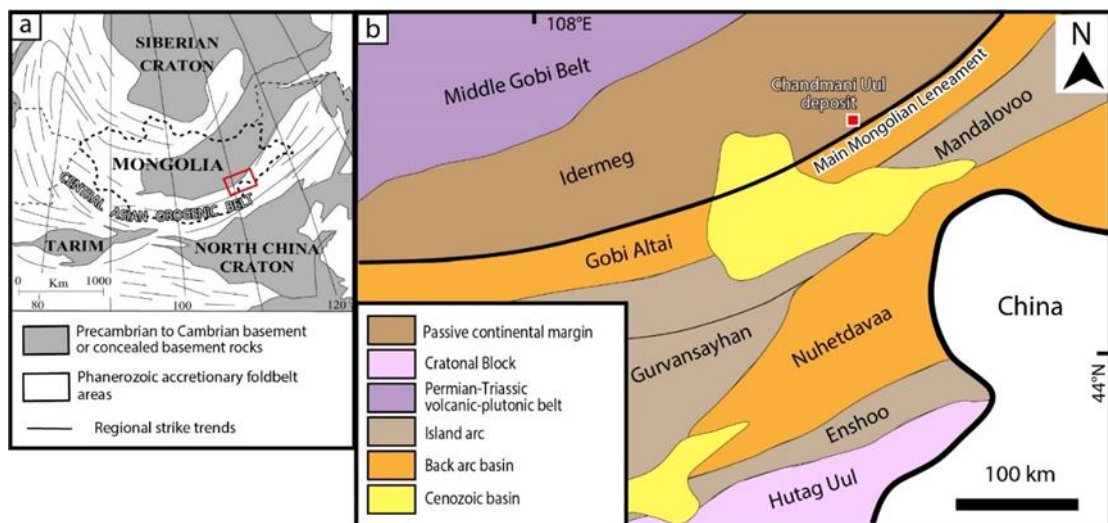


**Fig. 2.2** Location of the study area. (a) Sketched tectonic map of the CAOB (modified after Safanova & Santosh, 2014). (b) Tectonic subdivision of southeastern Mongolia (after Badarch et al., 2002; Rojas-Agramonte et al., 2011).

The strata of the Idermeg terrane in the study area correspond to the Shar Zeeg and the Bayanterem Formations; the former consists of sedimentary rocks,



including andesitic lava, breccia, and tuff of the passive continental margin, and the latter consists of limestone. The strata of the Gobi Altai terrane correspond to the Zeeriin Khural Formation, which consists of an alternation of sandstone, schist, and limestone within the back arc basin. Cretaceous sedimentary rock of the Shine Khudag Formation unconformably overlays the lower Neoproterozoic and Paleozoic strata (Fig. 2.3). Middle to Upper Cambrian intrusive bodies of mixed quartz diorite, biotite diorite, and granodiorite have intruded into the Shar Zeeg Formation (Bumburuu et al., 1990). The exact age of the plutonic rocks has not yet been obtained. These intrusive rocks are in fault contact with the Shar Zeeg Formation in this area.

The Chandmani Uul deposit is hosted within the Shar Zeeg Formation, as shown in the geologic map in Fig. 2.3. It consists of ~50 lenticular iron oxide ore bodies extending ~1,500 m in length in the NE–SW direction and 100–200 m in width (Fig. 2.3). The andesitic lava and pyroclastic rocks of the Shar Zeeg Formation are steeply dipping to the SE near the ore body. As shown in the cross section of Fig. 2.4, iron oxide ore lenses are hosted, nearly concordant (locally obviously discordant) to the strata of the Shar Zeeg Formation. The relationship of ore lenses with host rock shows the epigenetic nature of iron oxide mineralization. The nearly concordant dioritic sills with thicknesses of 10–20 m are recognized in drill holes.

There are two types of andesitic wall rock: andesitic schist and andesitic breccia, based on field appearance. It is difficult to distinguish whether the andesitic schist was originally in the form of lava or tuff, because of hydrothermal alteration. The andesitic breccia consists of rock fragments (65–70%) and matrix (30–35%).

Granitic rocks are exposed to the west and south of the Chandmani Uul deposit, and they make contact with sedimentary rocks with faults (Fig.2.3). Granitic rocks are commonly grayish in the least altered zone, and the color changes to reddish and pink in the hydrothermally altered zone.

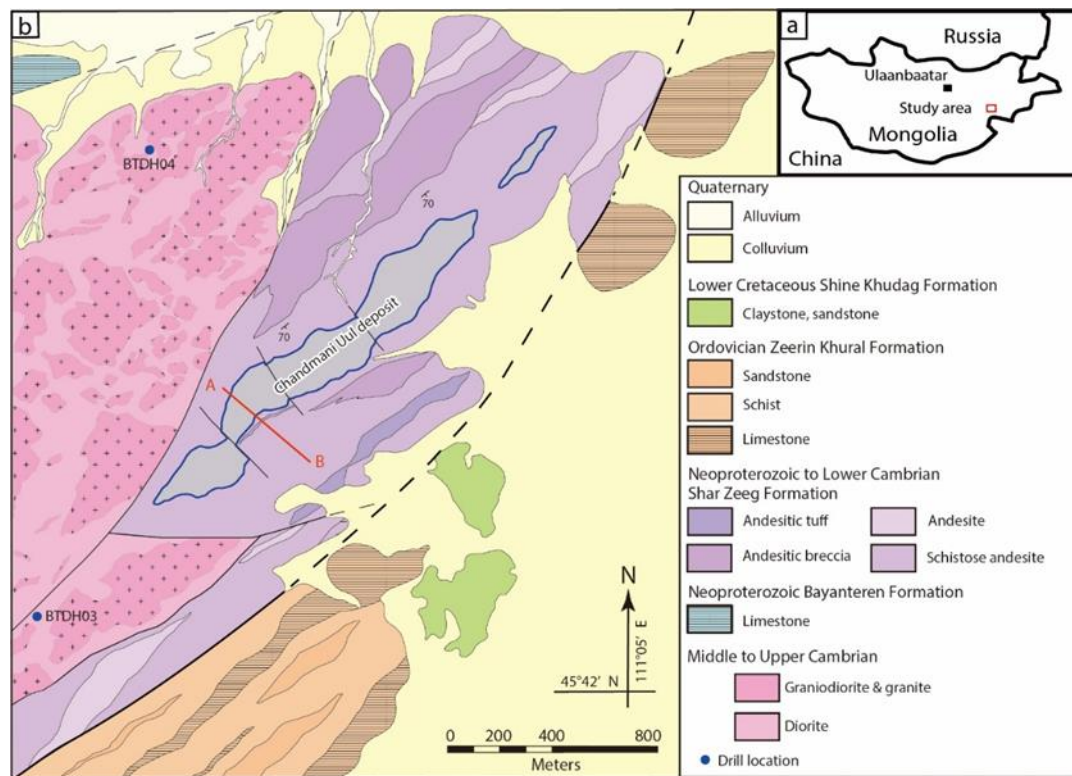


**Fig.2. 3** Geological map of the Chandmani Uul deposit. (a) Location of the study area. (b) Geology of the area surrounding the Chandmani Uul deposit. Line A–B corresponds to the cross-section shown in Fig. 2.4.

## 2.2. Alteration and mineralization

### 2.2.1 Wall rock alteration

The Chandmani Uul deposit consists of several lenticular iron oxide bodies with lengths of 100–200 m and thicknesses of 10–30 m (Fig. 2.4). It has a general strike of N40°E with dip of ~70°SE.

Closer to the ore zones, the hydrothermal alteration is characterized

sequentially from the surface to the deeper levels as sericite, sericite–chlorite, epidote, and potassic alteration zones, as shown in the cross section (Fig. 2.4).

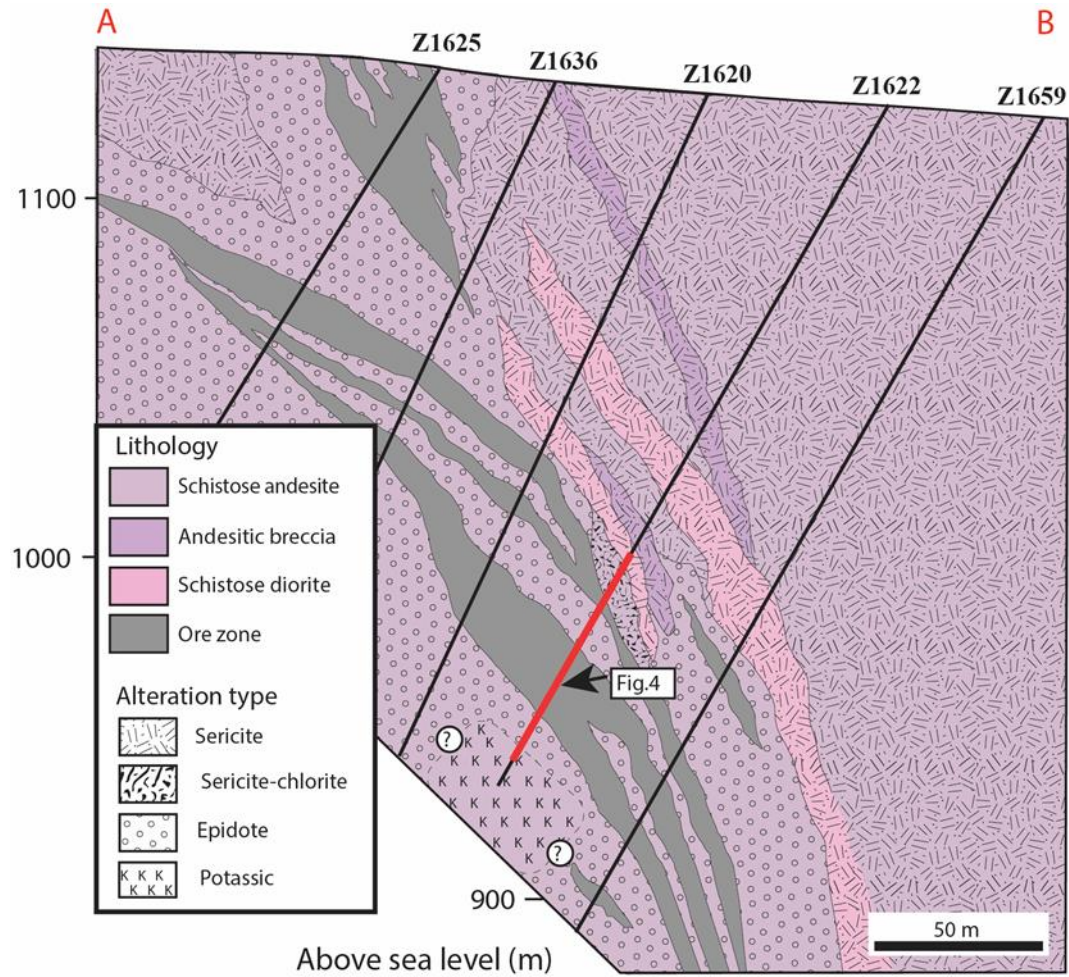


**Fig.2. 4** Map illustrating the cross-sectional distributions of the host rocks and ore bodies. The distribution of hydrothermal alteration zones is superimposed on the lithology map. The positions of five drill holes (Z1625, Z1636, Z1620, Z1622, and Z1659) are shown.

Alteration zones are also typically observed around the iron oxide ores in drillcore Z1622 (Fig. 2.5), whose position is shown in Fig. 2.4. Schistose diorite with sericite alteration has a greenish-gray appearance with brown dots of fine hematite aggregate (Fig. 2.5, CHU-127). Schistose andesite with sericite–chlorite alteration is dark greenish in color, and is commonly cut by veinlets of magnetite–

chalcopyrite (Fig. 2.5, CHU-128). Andesitic schist suffering from epidote alteration has an olive-green appearance, and is often replaced by quartz–calcite and/or chlorite veinlets (Fig. 2.5, CHU-131, CHU-138). The potassic alteration zone is characterized by conspicuous orange-colored K-feldspar (Fig. 2.5, CHU-140). In the contact area between the epidote alteration and potassic alteration zones, epidotized andesite is replaced by K-feldspar veinlets.

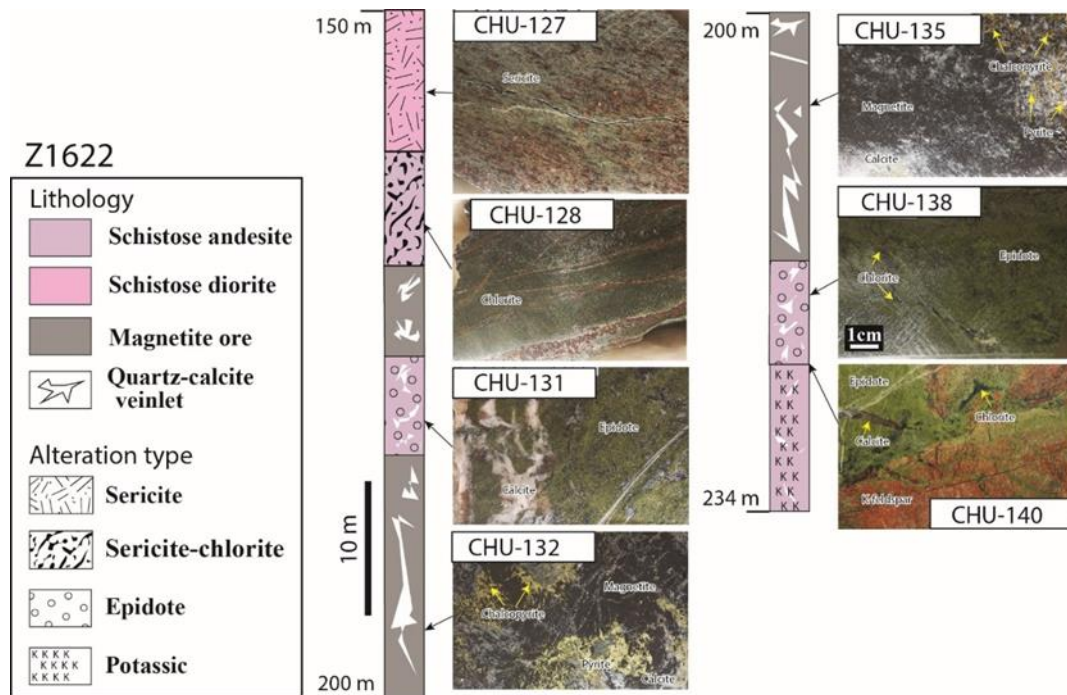


**Fig.2. 5** Occurrences of hydrothermal alteration zones and magnetite–sulfide ore in andesitic and dioritic host rocks in the 150–234 m interval of drill hole core Z1622, Chandmani Uul deposit.

Hornblende is the most dominant phenocryst of andesite with accessory amounts of plagioclase and quartz. The groundmass consists of plagioclase and volcanic glass. The hornblende phenocryst in andesite are partially altered to sericite (Fig. 2.6a, c) in the sericite and sericite–chlorite alteration zones, while epidote is the dominant alteration mineral after hornblende in the epidote alteration zone (Fig. 2.6d, f). Disseminated magnetite grains accompanying chalcopyrite are



ubiquitous in the sericite–chlorite alteration zone (Fig. 2.6b).

The dominant minerals in granodiorite are plagioclase (~50 vol.%), quartz (~25 vol.%), K-feldspar (~15 vol.%), and biotite (~10 vol.%), with sizes of 0.2–1.7 mm. Accessory minerals, such as titanite, monazite, and apatite, are also present. Dacite dykes that cut granitic rocks were observed in the drilling cores. The dacite contains 10–15 vol.% of phenocryst and 85–90 vol.% of groundmass. A large amount of sericite replacing plagioclase is common (Fig. 2.6g, h). Tabular and/or anhedral K-feldspar also replaces plagioclase (Fig. 2.6g), and K-feldspar shows a perthite texture. Biotite is partially changed to chlorite as a result of hydrothermal alteration (Fig. 2.6g). Pseudomorph of pyrite (goethite) is also present in the altered rocks.

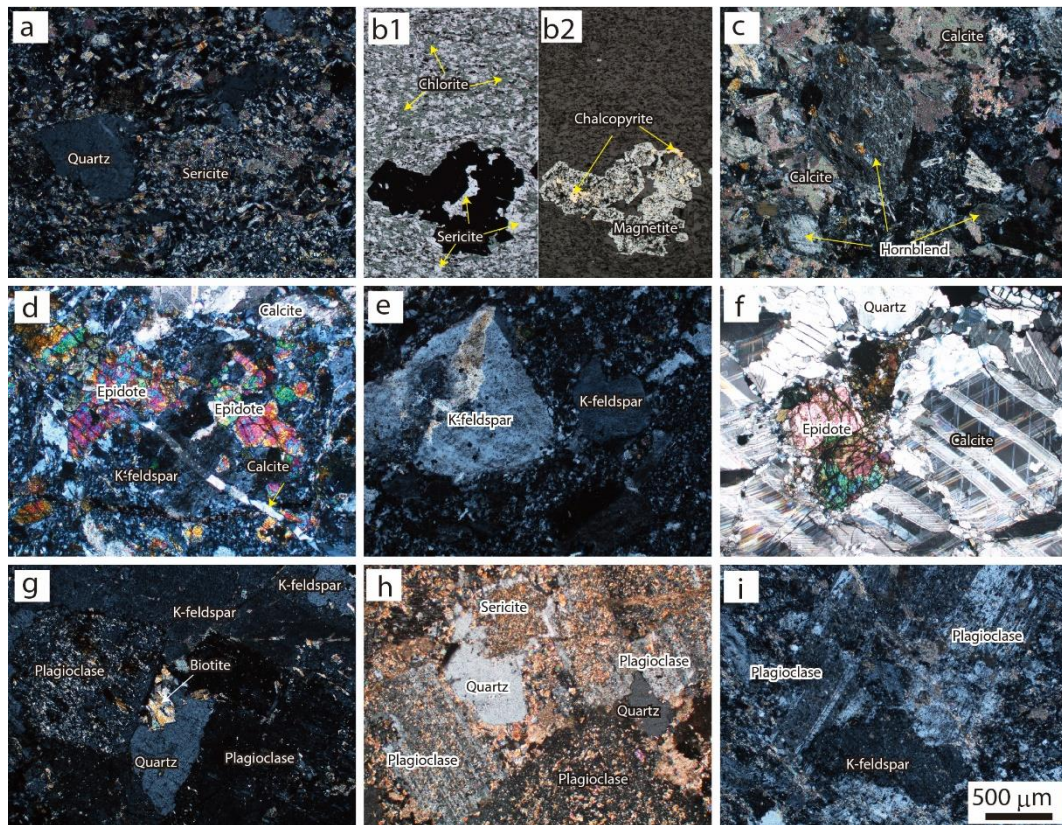


**Fig. 2. 6** Photomicrographs of common distal and proximal alteration assemblages in the Chandmani Uul deposit. (a) Schistose andesite in the sericite alteration zone. (b1) Andesite in the sericite–

chlorite alteration zone and (b2) disseminated magnetite grains accompanying chalcopyrite in the same area as that shown in b1. (c) Andesite in the sericite alteration zone, showing nearly complete replacement of hornblende phenocryst by sericite. (d) Schistose andesite in the contact area between epidote and potassic alteration zones. Later-stage calcite veinlet cuts altered andesite. (e) Schistose andesite in the potassic alteration zone. (f) Calcite vein in the epidote alteration zone. (g) Altered granite showing replacement of plagioclase by sericite. (h) Altered diorite showing complete replacement of plagioclase by sericite. (i) Altered dacite including plagioclase with a curved polysynthetic twin. All photographs were obtained under transmitted light with crossed nicols, except that in (b2), which was acquired under reflected light.

### **2.2.2 Mineralization**

The iron oxide ores have varied occurrences, and can be grouped into the following four types.

Type 1 ore: Massive magnetite ore accompanying fine grained hematite. It is usually cut by hematite–calcite–malachite veinlets (Fig. 2.7a).

Type 2 ore: Aggregate of acicular magnetite (mushketovite). Some of the magnetite is altered to brown hematite. Hematite–calcite veinlets accompanying malachite often cut this ore type (Fig. 2.7b).

Type 3 ore: Aggregate of prismatic magnetite (mushketovite), whose space is filled with chalcopyrite, pyrite, and calcite. This ore type is the most abundant in the deposit (CHU-132 and CHU-135 in Fig. 2.5, 2.7c).

Type 4 ore: Granular magnetite associated with green-colored garnet, calcite, and pyrite (Fig. 2.7d).

Type 1 ore occurs in the shallow level of the deposit, and type 4 ore is scarcely observable in the deepest level. The middle level of the deposit is dominated by types 2 and 3 ores, which represent most of the deposit. Sulfide mineralization

formed after the oxide stage replacing iron oxide minerals and as veinlets at late-stages of hydrothermal activity (Fig. 2.7c, 2.7d).

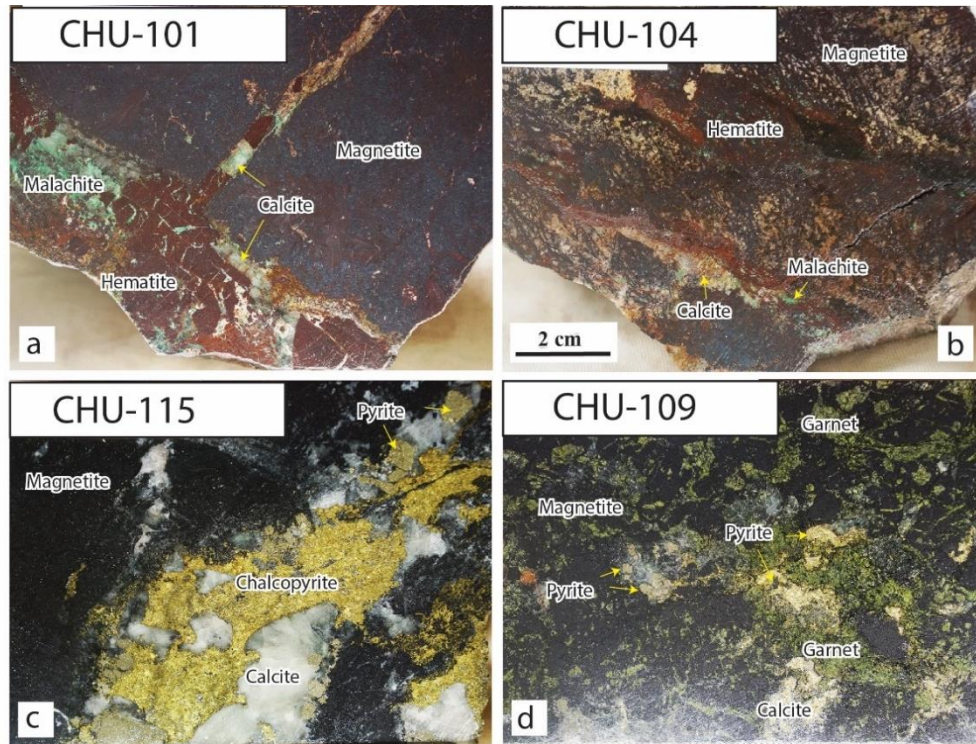


**Fig.2. 7** Typical ore samples from the Chandmani Uul deposit. (a) Type 1 massive magnetite ore from CHU-101 accompanying fine grained hematite, which is cut by a hematite–calcite–malachite veinlet. (b) Type 2 iron oxide ore from CHU-104 composed of an aggregate of acicular magnetite (mushketovite). Hematite–calcite veinlets accompanying malachite often cut this ore type. (c) Type 3 iron oxide–sulfide ore from CHU-115 composed of an aggregate of prismatic magnetite (mushketovite), where the spaces are filled with calcite. (d) Type 4 iron oxide–sulfide ore of CHU-109 composed of granular magnetite associated with green garnet, calcite, and pyrite.

There are three types of magnetite, 1) mushketovite, a pseudomorph of magnetite after prismatic hematite; 2) euhedral magnetite; and 3) cauliflower magnetite, an aggregate of fine-grained magnetite. The occurrences of these types of magnetite are summarized as follows.

Mushketovite originally precipitated as hematite is the most dominant iron oxide and shows prismatic and/or radial aggregation of prismatic crystals with grain sizes of 0.2–3 mm. Both type 2 and 3 ores are dominated by mushketovite. Prismatic mushketovite (Fig. 2.8a, d, e, g) is often associated with coarse-grained calcite with rhombohedral cleavages. In the case of sulfide-rich mushketovite ore, the radial of prismatic crystals of mushketovite is replaced by pyrite and chalcopryrite (Fig. 2.8b).

Euhedral magnetite is the dominant iron oxide mineral in type 1 ore. It shows chemical zoning, and can be divided into two subgroups, concentrically-zoned magnetite and oscillatory zoned magnetite, according to its zoning features. Concentrically-zoned magnetite exhibits a dark core and light rim based on back-scattered electron (BSE) imaging, which is associated with prismatic mushketovite (Fig. 2.8e, j). The oscillatory zoned magnetite precipitated almost simultaneously with mushketovite, and was followed by concentric zoned magnetite (Fig. 2.8k). Although microscopic observations often show oscillatory zoned magnetite as an aggregate of broken crystals, the BSE imaging confirmed that it was precipitated as single crystal (Fig. 2.8k).

Cauliflower magnetite is the typical constituent of type 4 ore. It appears as an aggregate of very fine-grained magnetite crystals associated with green-colored garnet, chalcopryrite, and calcite (Fig. 2.8c, f, h, l). In the deep level of drilling core Z1659, ~2-m-thick garnet-rich ore appears. Euhedral and partly broken garnet crystals ~0.5 mm in size are associated with cauliflower magnetite, calcite, and pyrite (Fig. 2.8h).



Pyrite and chalcopyrite are closely associated with iron oxide minerals, filling the cavities in iron oxides. The replacement texture of pyrite by chalcopyrite is commonly observed (Fig. 2.8b, c).

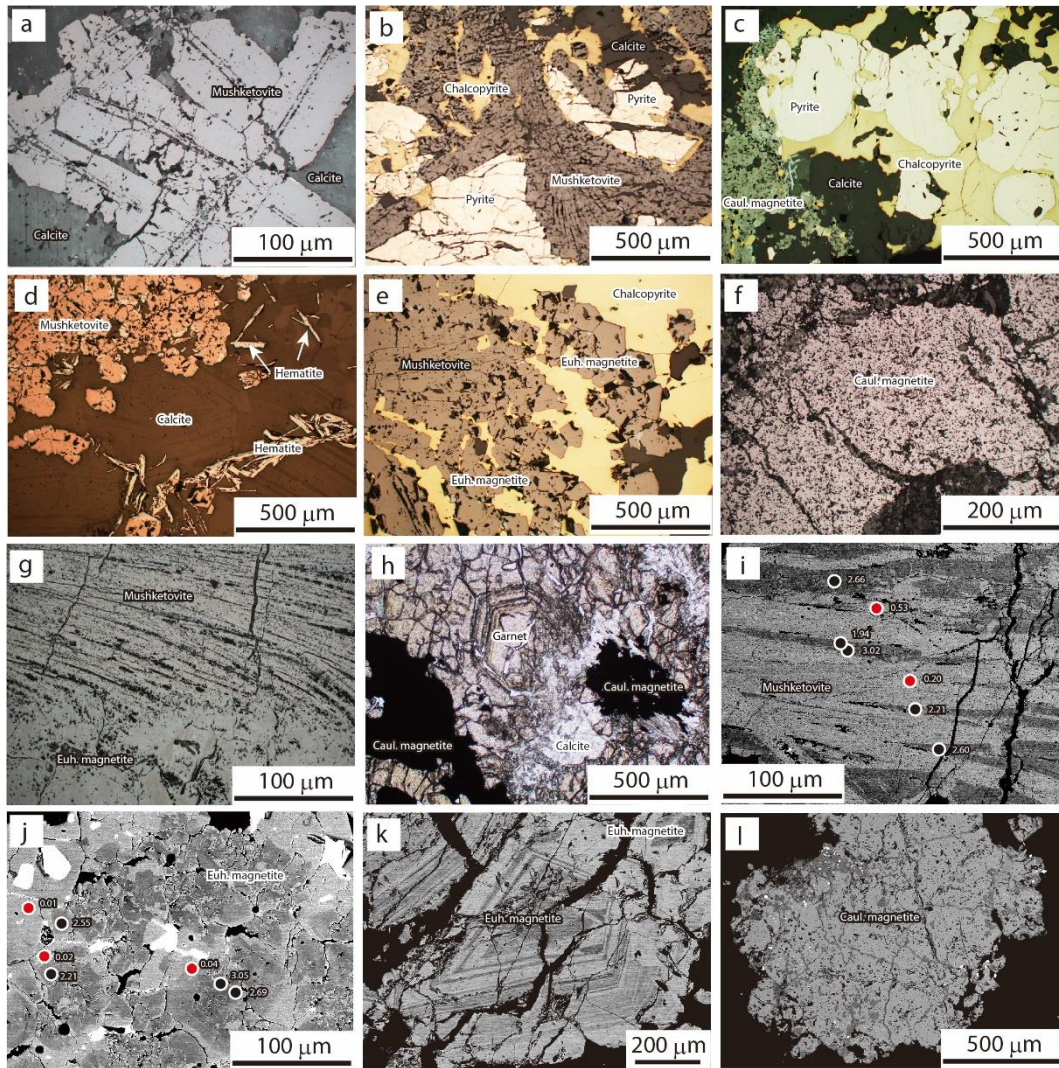


**Fig.2.8** Photomicrographs showing the characteristic features of the ore assemblages in the Chandmani Uul deposit. (a) Mushketovite crystals filled with calcite. (b) Radial aggregate of mushketovite crystals filled with chalcopyrite, pyrite, and calcite. (c) Cauliflower magnetite associated with chalcopyrite and early pyrite. (d) Mushketovite associated with calcite and acicular hematite. Some of the mushketovite was altered to hematite. (e) Mushketovite associated with euhedral magnetite, which is filled in with chalcopyrite and calcite. (f) Cauliflower magnetite. (g)

Mushketovite associated with euhedral magnetite. (h) Euhedral garnet crystals replaced by cauliflower magnetite and calcite. (i) Mushketovite showing alternate bands of a Si-rich dark zone and Si-poor light zone. (j) Euhedral magnetite composed of Si-rich core (dark zone) and Si-poor rim (light zone). (k) Association of euhedral magnetite with oscillatory and concentric zonings. (l) Aggregate of cauliflower magnetite. The photographs in (a–g) were obtained under reflected light, that in (h) was obtained under transmitted light, and those in (i–l) are BSE images. The SiO<sub>2</sub> content (wt%) of magnetite obtained using the EPMA is shown in photographs (i, j) using red (Si-poor) and black (Si-rich) points.

A paragenetic sequence of ore and alteration minerals was established, as shown in Fig. 2.9. The early-stage mineralization is characterized by iron oxide precipitation. This stage began with the precipitation of garnet, followed by the precipitation of magnetite and hematite. The early garnet was replaced by magnetite. Quartz precipitated with iron oxides to fill the spaces. The precipitation of alteration minerals such as epidote and K-feldspar was accompanied by iron oxides, while sericite precipitated after the iron oxides. Two different occurrences of sulfide minerals were observed: early sulfide dominated by pyrite and chalcopyrite precipitated to fill the spaces between the iron oxide minerals or replace them. Calcite was accompanied by pyrite and chalcopyrite. On the other hand, sulfide minerals appeared as veinlets to cut the iron oxide ores, as well as early sulfides. In such veinlets, pyrite, sphalerite, and galena precipitated with epidote, and bornite and covellite were also present in the later stage.

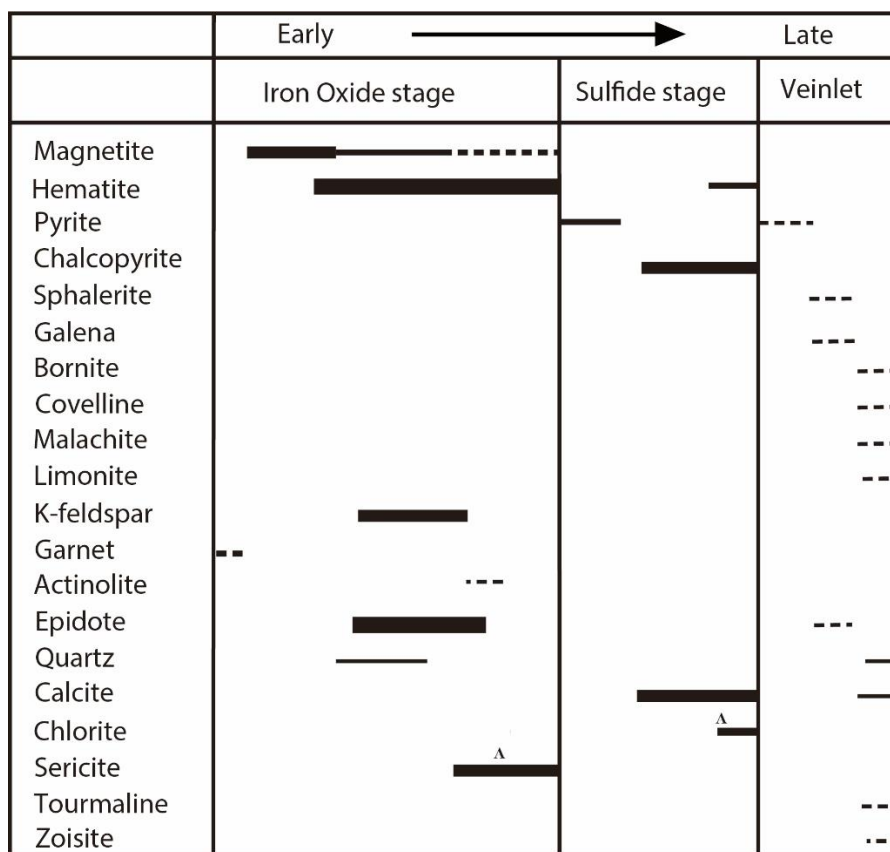


**Fig.2.9** Paragenetic sequence during hydrothermal alteration and mineralization at the Chandmani Uul deposit. Mushketovite is indicated as hematite in the paragenetic diagram. The inserted character “A” denotes a mineral associated with hydrothermally alteration of the wall rock.

### 3. Samples and analytical methods

Most of the host rocks and ore samples used in this study were collected from five drilling holes (Z1625, Z1636, Z1620, Z1622, and Z1659) (Fig. 2.4), and some samples were also taken from the surface outcrops of an open pit. Granitic rocks were collected from the outcrops of the open pit and two drilling holes (BTDH03 and BTDH04) of mineral prospect ~1 km west and south of the Chandmani Uul deposit (Fig. 2.3).

### **3.1. Geochemistry of granitic rocks**

In total, 15 samples of granitoids were selected for the geochemical study, as they are highly likely to have genetic relationship with mineralization. The whole-rock samples were crushed using an agate mortar to ~200 mesh, and whole-rock geochemical analyses were subsequently performed at Activation Laboratories Ltd., Canada. The major elements and 53 trace elements including rare-earth elements (REEs) were analyzed using a lithium metaborate/tetraborate fusion technique. The resulting molten beads were digested in a nitric acid, and the sample solutions were analyzed by ICP-OES and ICP-MS.

### **3.2. Zircon U-Pb analyses**

Granitic rock samples were cleaned and washed in an ultrasonic bath. The zircon crystals were handpicked from heavy fractions under a binocular microscope which were separated from the granitic rock samples by standard crushing and heavy-liquid techniques at the National Museum of Nature and Science, Tsukuba. Zircon crystals from the samples, the zircon standards FC1 and OD-3, and the glass standard NIST SRM610 were mounted in an epoxy resin and polished until the surface was flattened with the center of the embedded grains exposed (Tsutsumi et al., 2016). Backscattered electron and cathodoluminescence images of zircon grains were obtained using scanning electron microscope-cathodoluminescence (SEM-CL) equipment, JSM-6610 and a CL detector installed at the National Museum of Nature and Science, Tsukuba to examine the internal structures and identify and select distinct domains within zircons for laser ablation.

U-Pb analyses of nine samples (CHU179, CHU180, BT004, BT006, BT011, BT012, BT015, BT016, BT021) were investigated using an ablation inductively coupled plasma mass spectrometry (LA-ICP-MS). The experimental conditions and the analytical procedures followed for the measurements were after Tsutsumi et al. (2012, 2016). The spot size of the laser was 25  $\mu\text{m}$ .

### **3.3. Electron Probe Micro Analyses**

Typical samples of three types of magnetite: mushketovite, euhedral magnetite, and cauliflower magnetite, were selected for chemical analysis using a JXA-8350F electron probe microanalyzer (EPMA) (JEOL, Akishima) at the University of Tsukuba. Quantitative point analyses were conducted using an accelerating voltage of 15 kV, a beam current of 20 nA, and a focused beam diameter of 5  $\mu\text{m}$ , following the method described by Suzuki & Hayashi (2019). The acquisition periods for the X-ray intensity of each element were 10 s for the peak position and 10 s in total for the background positions. Quartz (Si), rutile (Ti), corundum (Al), periclase (Mg), wollastonite (for Ca), manganese ferrite (for Mn), Cr<sub>2</sub>O<sub>3</sub> (Cr), FeO (Fe), NiO (Ni), Cu metal (Cu), Zn metal (Zn), and V metal (V) were used as standards. After background processing, the X-ray intensities were corrected using the ZAF method. A mean detection limit of 0.1 wt% was achieved.

### **4.4. Oxygen isotope analyses of minerals**

Mineral grains were hand-picked from slabs of ore under a binocular microscope for the oxygen isotope analysis. The grains in most of the samples were

large ( $>0.1$  mm), and the mineral separates were more than 95% pure. Some quartz–magnetite pairs were prepared through chemical treatment of powdered iron oxide ores: magnetite was separated using a magnet, and the residual powder was subsequently reacted with HCl and aqua regia to remove impurity magnetite and/or hematite, calcite, and sulfides. Finally, pure quartz was obtained.

Oxygen was extracted from the magnetite, quartz and epidote using a 17 Watt JLC-200 CO<sub>2</sub>-laser ( $\lambda=10.6$   $\mu\text{m}$ ) (Japan Laser Co., Shinjuku) and BrF<sub>5</sub> using a fluorination method similar to that described by Hayashi et al. (2001). Approximately 2 mg of each mineral in grain or powder form was placed in a hole drilled in a Ni rod placed in a reaction cell under a BrF<sub>5</sub> atmosphere with a pressure of  $\sim 110$  mm Hg. The CO<sub>2</sub>-laser beam was focused to a diameter of  $\sim 25$   $\mu\text{m}$  and then irradiated through a BaF<sub>2</sub> window. Completion of the reaction between the mineral and BrF<sub>5</sub> was confirmed by observing the reaction under a microscope positioned co-axially with the CO<sub>2</sub>-laser. The oxygen extracted from the minerals was converted into CO<sub>2</sub> quantitatively in a reaction with heated diamond. Completion of the reaction to extract oxygen from the minerals was evaluated by measuring the amount of CO<sub>2</sub> released from the minerals. The isotopic compositions of the CO<sub>2</sub> was measured using a MAT-253 mass spectrometer (Thermo-Finnigan LLC, San Jose) at the National Museum of Nature and Science, Tsukuba and the Center for Advanced Marine Core Research, Kochi University. The  $^{18}\text{O}/^{16}\text{O}$  ratios were expressed using the conventional  $\delta^{18}\text{O}$  notation relative to the Vienna Standard Mean Ocean Water. The accuracy of the CO<sub>2</sub>-laser fluorination oxygen isotope analyses was evaluated by repeated analysis of working standards. The  $\delta^{18}\text{O}$  value of the reference quartz (NBS 28,  $\delta^{18}\text{O} = 9.6\text{‰}$ ) was measured using

each sample, and a reproducibility of better than 0.2‰ was achieved (Hayashi et al., 2001).

## **4. Analytical results**

### **4.1 Major elements and trace elements of granitic rocks**

The major element data of the granitoids are given in the Table 2.1, which shows that SiO<sub>2</sub> ranges from 58.36 to 64.99 wt% (average 62.16 wt%), Al<sub>2</sub>O<sub>3</sub> varies from 13.91 to 16.64 wt% (average 15.6 wt%), CaO contributes 2.21 to 5.12 wt% (average 3.41 wt%), Na<sub>2</sub>O constitutes 2.26 to 5.28 wt% (average 3.95 wt%), and K<sub>2</sub>O ranges from 1.96 to 4.7 wt% (average 3.34 wt%). Those rocks have extremely high total alkali contents (Na<sub>2</sub>O+ K<sub>2</sub>O ranges from 6.01 wt% to 8.37 wt%) with an average of 7.29 wt%, and the ratio of Na<sub>2</sub>O/K<sub>2</sub>O varies from 0.37 to 1.66.

The granitoids are sub-alkaline and are plotted in the region of mixed monzonite, quartz monzonite, diorite, granodiorite, and granite fields in the K<sub>2</sub>O+Na<sub>2</sub>O versus SiO<sub>2</sub> diagram (Fig. 2.10a). As mentioned previously, these granitoids can be classified as quartz diorite, biotite diorite, granodiorite, and biotite granite based on the modal abundances of the minerals under microscopic observation. Discrepancies between the rock types obtained using chemical data and petrography are caused by strong sericitic alteration: alkaline elements, especially K, were added to the granitoids during hydrothermal alteration. Replacement of plagioclase and K-feldspar by sericite is common according to the microscopic observation (Fig. 2.7g–i). The granitic suites plot of Maniar & Priccoli (1989) indicates that most granitoids are I-type, with two exceptions that are S-type

(Fig. 2.10b). The Al saturation index [ $\text{Al}_2\text{O}_3/(\text{CaO} + \text{Na}_2\text{O} + \text{K}_2\text{O})$ ] of these granitic rocks ranges from 0.81 to 1.24, and their molar  $\text{Al}_2\text{O}_3/(\text{Na}_2\text{O} + \text{K}_2\text{O})$  ratios are greater than 1 (Table 2.1).

The granitoids have  $\Sigma\text{REE}$  varying from 69.47 to 119.92 ppm (average of 97.74 ppm) and LREE/REE ratios of 6.83–9.57 (average 7.79). The  $\delta\text{Eu}$  values range from 0.57 to 0.92 (average 0.80) (Table 2.2). The primitive mantle-normalized trace element spidergram shows LILEs enrichment and HFSE depletion (Fig. 2.10e). In the geotectonic discrimination diagram, these granitoids are plotted in the volcanic arc granite field (Fig. 2.10c, d).  $(\text{La}/\text{Sm})\text{N}$  and  $(\text{La}/\text{Yb})\text{N}$  of granitoids range from 2.55 to 4.11, and from 1.65 to 2.77, respectively.



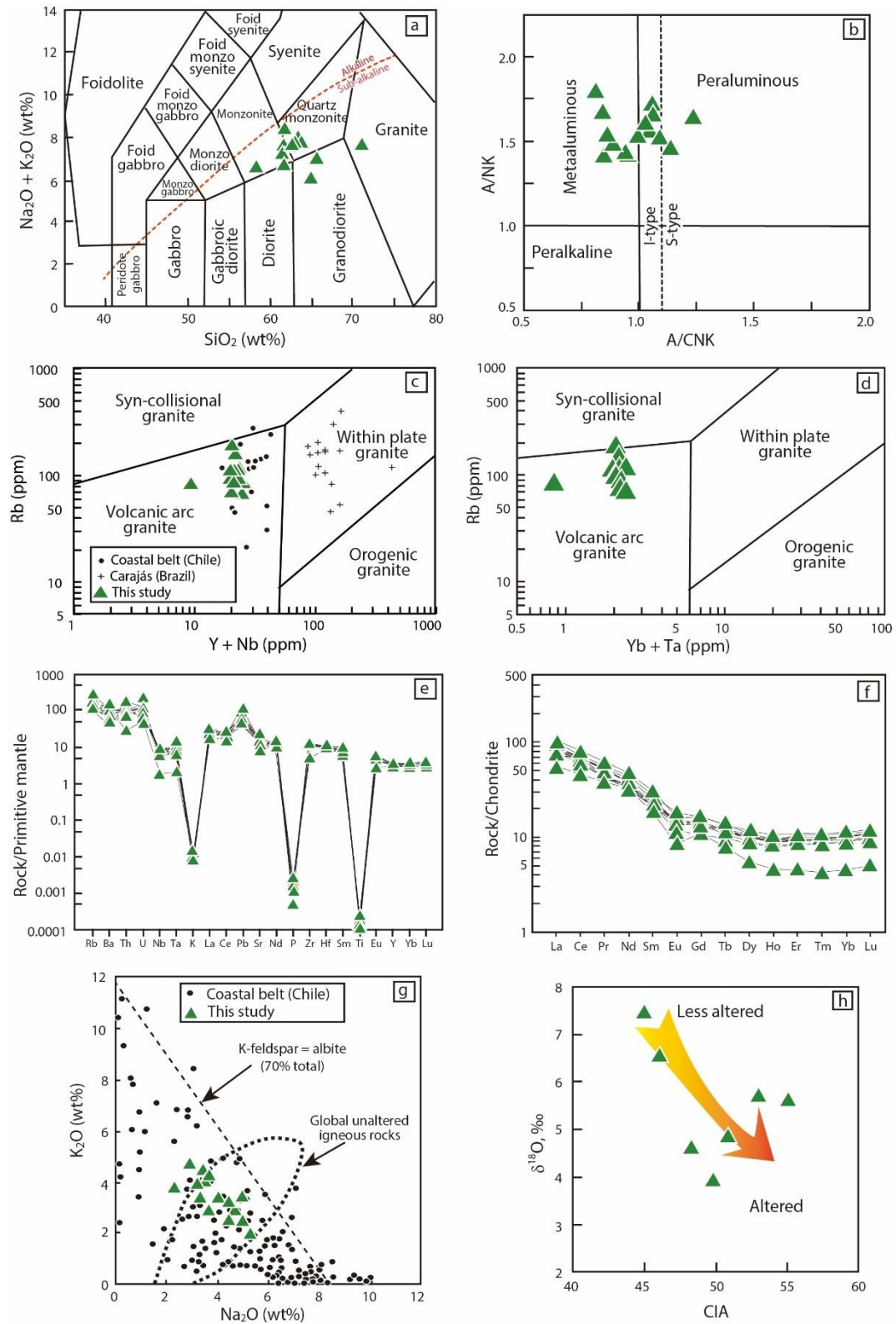


**Fig.2. 10** Geochemical discrimination diagrams and petrochemical data for granitoids from the Chandmani Uul deposit. (a)  $\text{K}_2\text{O} + \text{Na}_2\text{O}$  versus  $\text{SiO}_2$  diagram (after Middlemost, 1994). The fields for the alkaline and sub-alkaline compositions are from Irvine and Barragar (1971). (b)  $\text{A/CNK}$

(molar ratio  $\text{Al}_2\text{O}_3/(\text{CaO}+\text{Na}_2\text{O}+\text{K}_2\text{O})$ ) versus A/NK (molar ratio  $\text{Al}_2\text{O}_3/(\text{Na}_2\text{O}+\text{K}_2\text{O})$ ) diagram after Maniar & Piccoli, (1989). The I- and S-type boundary is after Chappell (1999). (c) Rb versus Y+Nb plot after Pearce et al. (1984). The data for the granitic rocks from the IOCG provinces in the Chilean coastal belt and Brazilian Carajás district are from Marschik et al. (2003) and Pollard (2006), respectively. (d) Rb versus Yb+Ta plot after Pearce et al. (1984). (e) and (f) Primitive mantle-normalized spider diagram and chondrite-normalized REE patterns (the normalization values are from Sun & McDonough, 1989). (g)  $\text{K}_2\text{O}$  versus  $\text{Na}_2\text{O}$  plot for the granitoids in this study and those from the IOCG provinces of the Chilean coastal belt (the data are from Barton, 2014). (h) CIA (Nesbitt & Young, 1982) versus  $\delta^{18}\text{O}$  plot. The arrow indicates the oxygen isotope trend during hydrothermal alteration.

#### 4.2. Zircon U-Pb ages

Zircon LA-ICP-MS U-Pb ages for the granitic rocks illustrated, and the representative locations of the LA-ICP-MS U-Pb isotope analytical points are spotted by red circles Fig.2.11. The results of the zircon U-Pb isotopic are listed in Table 2.3. U–Pb concordia diagrams and age distribution plot of result of LA-ICP-MS measurements of age-known zircon samples from granitoids are illustrated in Fig.2.12. All zircons in the study area samples show rhythmic oscillatory and/or sector zoning on cathodoluminescence images, that is commonly observed in igneous zircons (Corfu et al., 2003, Tsutsumi et al., 2015).

Sample CHU179, a fine to medium grained granodiorite, was collected from the drilling core Z1671 (171.5m). Zircon grains in the sample show columnar habit and are translucent in CL images. Results of zircon U-Pb isotopic analysis shows Th and U contents in the range of 33-316 and 80-356 ppm, with Th/U ratios (0.42-0.76) exceeding 0.1, indicating a magmatic origin. The  $^{238}\text{U}/^{206}\text{Pb}$  ages on 25 spots

range from  $461 \pm 8.3$  to  $544 \pm 9.4$  Ma, yielding a weighted mean age of  $475.6 \pm 4.3$  Ma (MSWD=2.0; rejected 0 of 19).

Sample CHU180, a fine to medium grained granodiorite, was collected from the drilling core Z1671 (198.8). In CL images, Zircon grains in the sample show columnar habit, and are translucent in CL images. Th and U contents and Th/U ratio of the spots are 47-254ppm, 61-295ppm, and 0.44-0.93ppm, respectively. The  $^{238}\text{U}/^{206}\text{Pb}$  ages on 24 spots range from  $426 \pm 5.3$  to  $510 \pm 6.8$  Ma, yielding a weighted mean age of  $484 \pm 3.0$  Ma (MSWD=0.99; rejected 1 of 20).

Sample BT004, a fine to medium grained biotite- quartz diorite, was sampled from the drilling core BTDH03 (23.9m). Zircon grains in the sample show euhedral habit, and are translucent in CL images. Their Th and U contents and Th/U ratio display ranges of 38-225ppm, 83-357 ppm, and 0.40-0.84, respectively. The  $^{238}\text{U}/^{206}\text{Pb}$  ages on 27 spots range from  $471 \pm 6.0$  to  $521 \pm 6.3$  Ma, yielding a weighted mean age of  $486 \pm 2.6$  Ma (MSWD=1.4; rejected 1 of 23).

Sample BT006, a fine to medium grained quartz diorite, was sampled from the drilling core BTDH03 (180m). Zircon grains in the sample show euhedral and columnar habit, and are translucent in CL images. Th and U contents and Th/U ratio of these spots are 31-250 ppm, 76-300 ppm, and 0.41-0.86, respectively. The  $^{238}\text{U}/^{206}\text{Pb}$  ages on 25 spots range from  $466 \pm 4.6$  to  $508 \pm 5.3$  Ma, yielding a weighted mean age of  $486 \pm 2.9$  Ma (MSWD=1.00; rejected 1 of 21).

Sample BT011, a fine to medium grained biotite- quartz diorite, was sampled from the drilling core BTDH03 (271.6m). Zircon grains in the sample show euhedral and columnar habit, and are in CL images. Th and U contents and Th/U ratio of the spots are 44-212 ppm, 93-260 ppm, and 0.44-0.84, respectively. The

$^{238}\text{U}/^{206}\text{Pb}$  ages on 14 spots range from  $459\pm 4.6$  to  $507.1\pm 7.6$  Ma, yielding a weighted mean age of  $481\pm 5.0$  Ma (MSWD=1.6; rejected 0 of 11).

Sample BT012, a fine to medium grained biotite- quartz diorite, was collected from the drilling core BTDH04 (16.9m). Zircon grains in the sample show euhedral and columnar habit, and are translucent in CL images. Their Th and U contents and Th/U ratio of the ratios are 35-561 ppm, 77-507 ppm, and 0.43-1.14, respectively. The  $^{238}\text{U}/^{206}\text{Pb}$  ages on 27 spots range from  $465\pm 4.3$  to  $496.2\pm 5.8$  Ma, yielding a weighted mean age of  $479\pm 2.9$  Ma (MSWD=1.6; rejected 0 of 11).

Sample BT015, a fine to medium grained biotite- quartz diorite, was collected from the drilling core BTDH04 (115.1m). Zircon grains from sample BT015 show euhedral and columnar features, and are translucent in CL images. Th and U contents and Th/U ratio of the ratios are 34-225 ppm, 78-310 ppm, and 0.44-0.75, respectively. The  $^{238}\text{U}/^{206}\text{Pb}$  ages on 23 spots range from  $465\pm 4.3$  to  $512.3\pm 5.9$  Ma, yielding a weighted mean age of  $486.1\pm 3.2$  Ma (MSWD=1.5; rejected 0 of 21).

Sample BT016, a fine to medium grained biotite- quartz diorite, was collected from the drilling core BTDH04 (115.1m). Zircon grains from sample BT016 show euhedral and columnar features, and are translucent in CL images. Th and U contents and Th/U ratio of the ratios are 28-192 ppm, 81-264 ppm, and 0.34-0.87, respectively. The  $^{238}\text{U}/^{206}\text{Pb}$  ages on 33 spots range from  $452\pm 7.8$  to  $503\pm 7.0$  Ma, yielding a weighted mean age of  $483.1\pm 2.6$  Ma (MSWD=0.97; rejected 1 of 22).

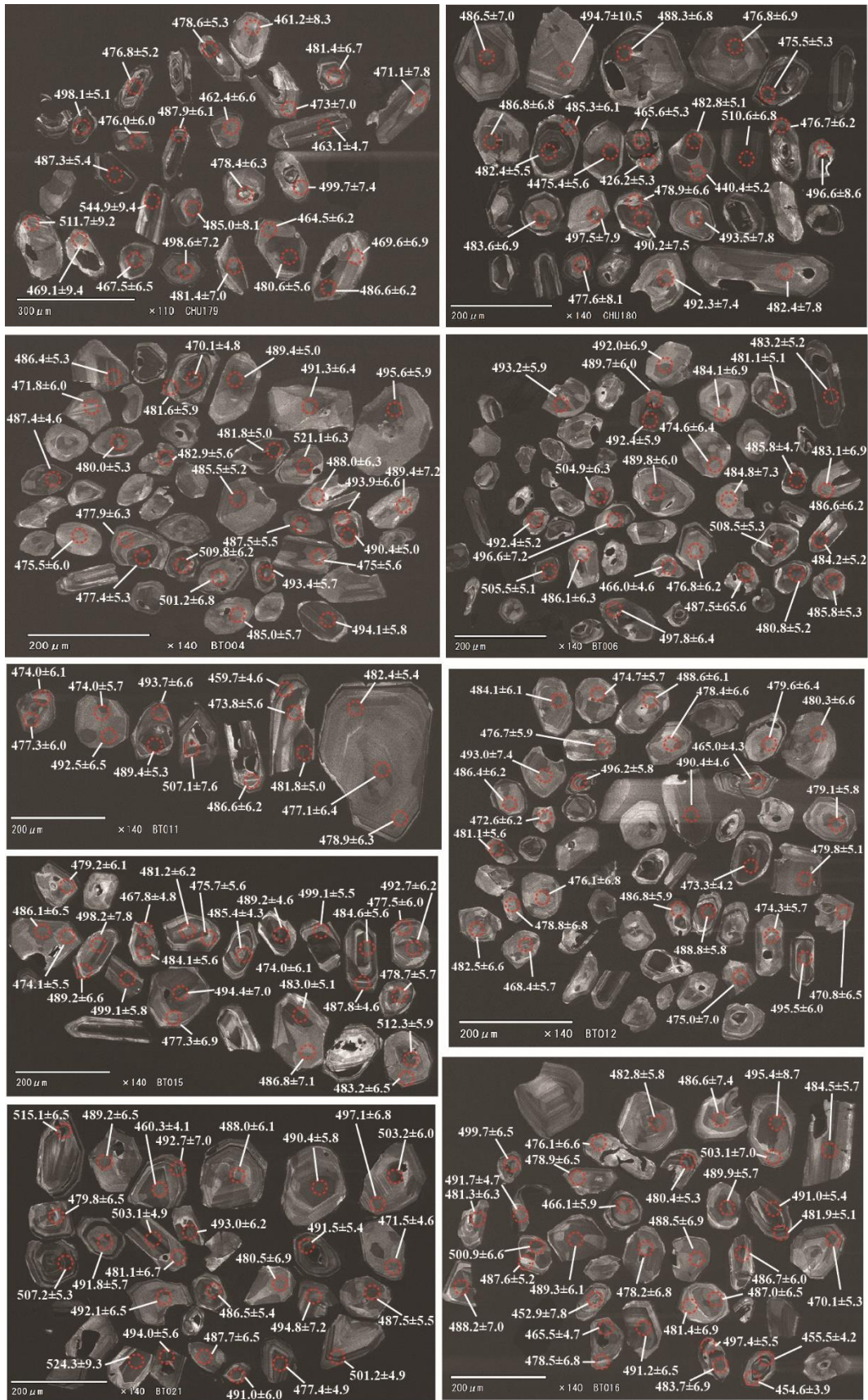


**Fig.2. 11** CL image of representative zircons from the samples.



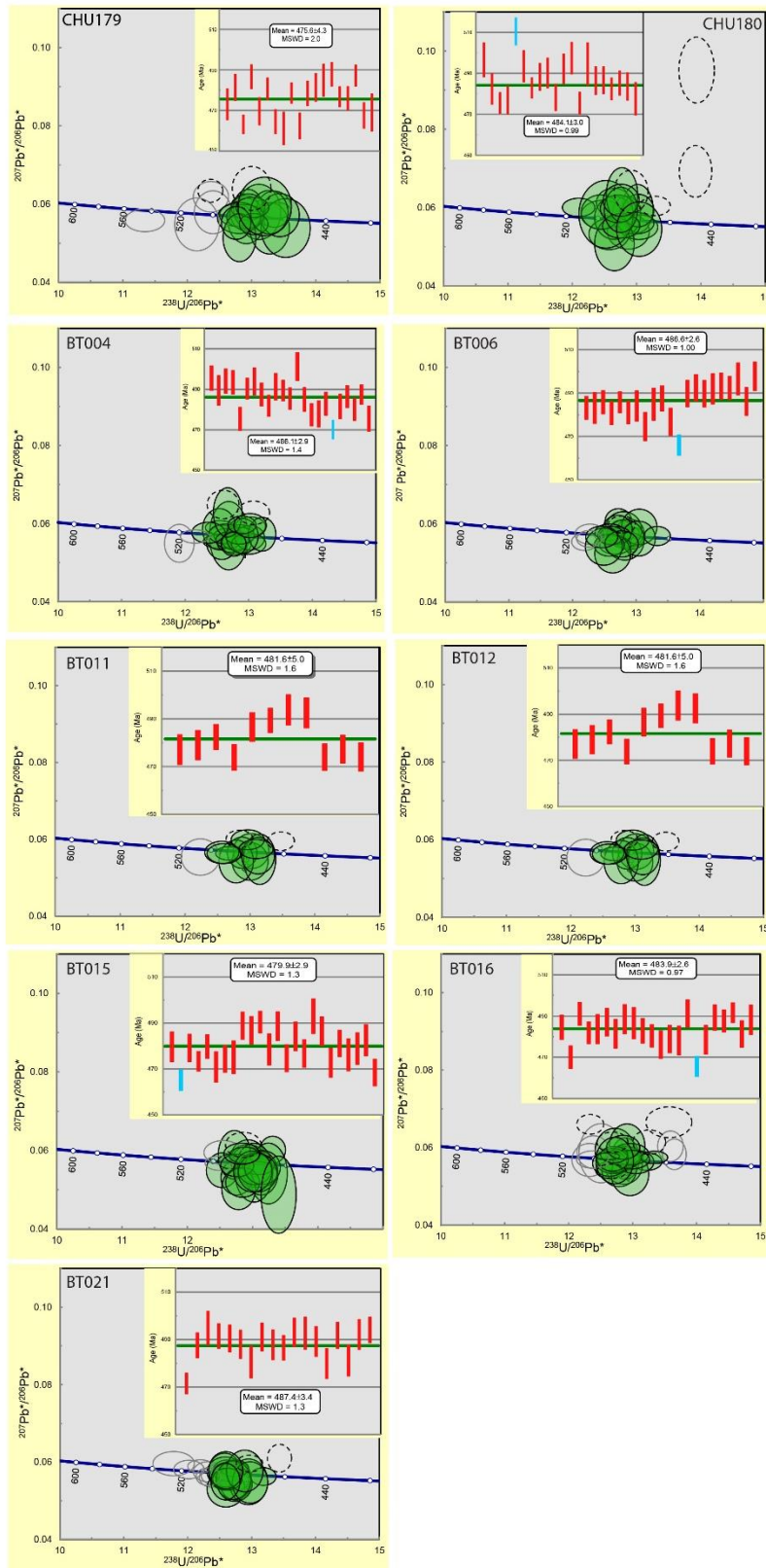


**Fig.2. 12** U–Pb concordia diagrams and age distribution plot of result of LA-ICP-MS measurements of age-known zircon samples from granitoids

Sample BT021, a fine to medium grained biotite- quartz diorite, was collected from the drilling core BTDH04 (357.5m). Zircon grains in the sample show euhedral and columnar features, and are translucent, in CL images. Their Th and U contents and Th/U ratio of the ratios are 41-179 ppm, 80-216 ppm, and 0.42-0.75, respectively. The  $^{238}\text{U}/^{206}\text{Pb}$  ages on 27 spots range from  $471 \pm 4.6$  to  $524 \pm 9.3$  Ma, yielding a weighted mean age of  $487.4 \pm 3.4$  Ma (MSWD=1.3; rejected 0 of 18).

The Chandmani Uul biotite-diorite, granodiorite, granite intruded in the southwestern part of the Shar Zeeg formation in the study area, and the zircon U-Pb LA-ICP-MAS data from this intrusion yield age of  $426 \pm 5.3$  to  $544 \pm 9.3$  Ma which is consistent with ore-formation age. The magmatism is deduced to have provided the heat and fluid input.

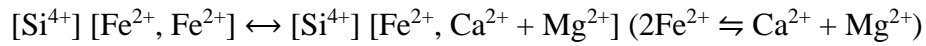
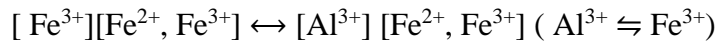
#### **4.3. Magnetite chemistry**

The following elements were appreciably detected and thus were measured: Fe, Si, Al, Ti, Mn, Mg, Ca, Zn and Cu. In total, 94 quantitative point analyses were conducted, and representative results are listed in Table 2.4. Because the Fe-calculations were performed using FeO (II), the total weight of all the oxide components was usually ~93%, which led to reasonable recalculated values. Si is the main impurity element in magnetite, and magnetite analysis revealed up to 3.1 wt% SiO<sub>2</sub> in euhedral magnetite and to 3.0 wt% SiO<sub>2</sub> in mushketovite.

The BSE images of magnetite suggest variable chemical compositions. The BSE image of mushketovite (Fig. 2.8i) shows minor elements-rich (dark color in BSE) and minor elements-poor (light color in BSE) zones parallel to its elongation.

Euhedral magnetite (Fig. 2.8j) exhibits a minor elements-rich core and minor elements-poor rim. Some analytical data related to the SiO<sub>2</sub> contents are shown in the BSE images (Fig. 2.8i, j). Cauliflower magnetite with a thin hematite rim has a relatively homogeneous composition (Fig. 2.8l). The TiO<sub>2</sub> content is low (<0.1 wt%) for all types of magnetite.

Figure 2.13 shows the correlations of the minor elements in the magnetite. The numbers of atoms per formula unit plotted in Fig. 2.13 were calculated based on the 32 oxygen atoms in the crystal structure of magnetite. Several correlations between the measured components are observable. Ferric oxide shows a negative correlations with Si (Fig. 2.13a) and Al (Fig. 2.13b), and Fe (II) exhibits correlations with Si (Fig. 2.13c) and (Ca+Mg) (Fig. 2.13d). Figures 2.13b and 2.13d suggest that the following substitutions additionally occur in minor ranges.





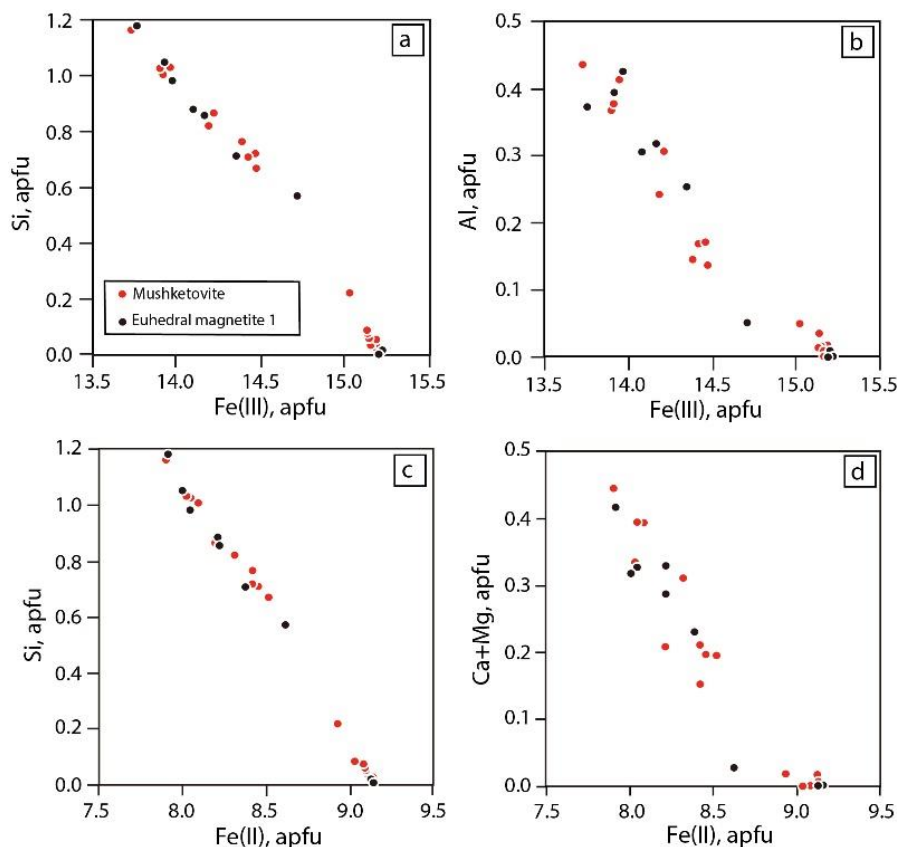


**Fig.2. 13** Correlations of elements in magnetite from the Chandmani Uul deposit. (a) Ferric iron versus Si plot. (b) Ferric iron versus Al plot. (c) Ferrous iron versus Si plot. (d) Ferrous iron versus Ca+Mg plot.

#### 4.4. Oxygen Isotope

The oxygen isotope values were obtained for mushketovite, euhedral magnetite, cauliflower magnetite, quartz, epidote in the alteration zone, and epidote in the late vein and are presented in Table 2.5 and Fig. 2.14. The oxygen isotope values were also measured for bulk powder samples of the granitic rocks that were used for the chemical analysis, and are summarized in Table 2.1. The  $\delta^{18}\text{O}$  values of the minerals were found to be  $-5.9 - 2.8\text{‰}$  ( $n = 47$ ) for mushketovite,  $-3.8 - 2.9\text{‰}$  ( $n = 6$ ) for euhedral magnetite, and  $-1.3 - 2.6\text{‰}$  ( $n = 5$ ) for cauliflower

magnetite. While the values for mushketovite are spread across a wide range, those of euhedral magnetite fall within a narrow range. Meanwhile, the  $\delta^{18}\text{O}$  values for the silicate minerals are 10.4 – 14.9‰ (n = 11) for quartz and 3.6 – 6.6‰ (n = 16) for epidote. Epidotes appear in an alteration zone of the host rock, and have similar  $\delta^{18}\text{O}$  values to those in late-stage veinlet.

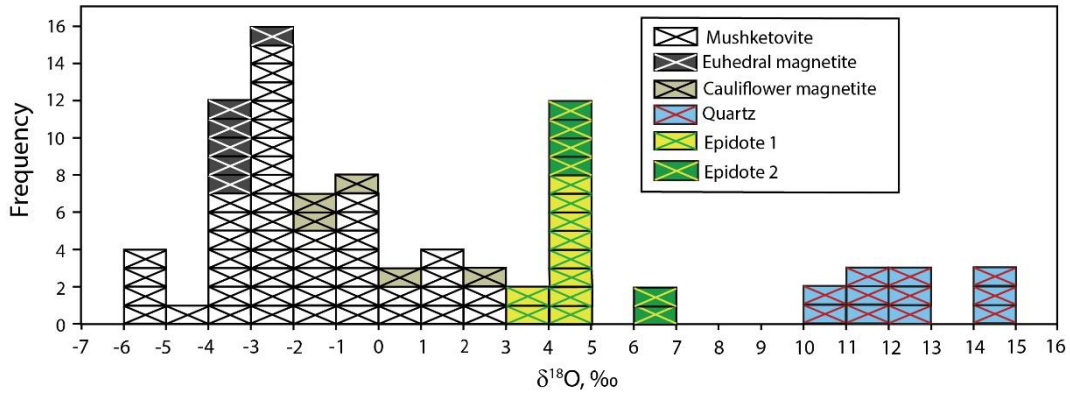


**Fig.2. 14**  $\delta^{18}\text{O}$  values of minerals from the Chandmani Uul deposit. Epidote-1 and -2 occur in the wall rock alteration zone and late-stage vein, respectively.

## 5. Discussion

### 5.1. Oxygen isotope geothermometry of iron oxide ore

To estimate the ore formation temperature, the oxygen isotope values of several mineral pairs were examined. Among the mineral pairs, magnetite–quartz was the most likely in this study since magnetite (mushketovite) and quartz are intimately associated with each other in iron oxide ores. These minerals were separated through the chemical treatment described earlier. Magnetite and quartz constitute one of the most sensitive mineral pairs for the large differences in oxygen isotope fractionation (Chacko et al., 2001).

The equilibrium fractionation factors ( $1000\ln\alpha$ ) for the oxygen isotopes used in this study were as follows:

Magnetite–water:  $1.47 \times 10^6/T^2 - 3.70$  (Bottinga & Javoy, 1973)

Quartz–water:  $3.34 \times 10^6/T^2 - 3.31$  (Matsuhisa et al., 1979)

Epidote–water:  $-(1.56 + 1.92\beta_{ps}) \times 10^6/T^2$  (Matthews & Schliestedt., 1984),

where T is the absolute temperature (K) and  $\beta_{ps}$  is the mole fraction of the pistacite component. The  $\beta_{ps}$  value of epidote was assumed to be 0.28 in this study, based on the average value obtained in the microprobe analyses.

Five quartz–magnetite pairs were available for the temperature calculations, whose results are shown in Table 2.5. Although mushketovite originally precipitated as hematite, the oxygen isotope fractionation factor of magnetite was applied to mushketovite for lack of applicable fractionation factor of hematite. Selected quartz–magnetite pairs suggest that the precipitation temperatures of euhedral magnetite (CHU-158 and CHU-170) and mushketovite (CHU-137, -161, and -218) are 299 – 309°C and 218 – 311°C, respectively. Sample CHU-161 contained both mushketovite and cauliflower magnetite, which have different  $\delta^{18}\text{O}$  values: -3.5‰ for mushketovite and -0.5‰ for cauliflower magnetite (Table 2.5). Since the quartz in this sample is associated with mushketovite rather than cauliflower magnetite, the temperature obtained from the quartz–mushketovite pair is reliable. The calculated temperatures have a broad range of 218 – 311°C. However, if the lowest temperature of 218°C is excluded, the values fall within a convergent range of 299 – 311°C (average 304.2°C). This temperature range is the most probable for iron oxide precipitation.

## 5.2. Source of ore-forming fluid

The oxygen isotope values of the fluids responsible for the minerals were calculated at 300°C, assuming fluid-dominant conditions. The calculated  $\delta^{18}\text{O}$  values of water are shown in Table 2.5 and plotted in Fig. 2.15. The  $\delta^{18}\text{O}$  values of the water related to the minerals are 4.4 – 5.3‰ for euhedral magnetite, 2.3 – 10.9‰ for mushketovite, 6.9 – 10.7‰ for cauliflower magnetite, 3.7 – 8.0‰ for quartz, 3.1 – 4.5‰ for epidote in the epidote alteration zone of the wall rock, and 3.8 – 6.2‰ for the epidote in the late-stage vein.

Figure 2.15 indicates that the water equilibrated with cauliflower magnetite has  $\delta^{18}\text{O}$  values corresponding to the range for magmatic water, whereas the  $\delta^{18}\text{O}$  values of the water responsible for mushketovite are spread across a wide range; about half of them correspond to the  $\delta^{18}\text{O}$  values of magmatic water, and the other half are lighter  $\delta^{18}\text{O}$ . The water responsible for euhedral magnetite has slightly lighter  $\delta^{18}\text{O}$  values outside of the range of magmatic water. In the case of the silicate minerals, half of the quartz specimens suggest mineralizing fluid with the  $\delta^{18}\text{O}$  range of primary magmatic water ( $\delta^{18}\text{O} = 5.5 - 10.0\text{‰}$ ). The mineralizing fluid half of the quartz and most of the epidote precipitated from water with  $\delta^{18}\text{O}$  values significantly lighter than that of magmatic water.

The  $\delta^{18}\text{O}$  values of magmatic water were estimated, based on the  $\delta^{18}\text{O}$  values of granitic rocks and the oxygen isotope fractionation factor between plagioclase and  $\text{H}_2\text{O}$  at magmatic temperatures (Sheppard, 1986; Ohmoto, 1986; Taylor, 1997). Because the oxygen isotope fractionation between a mineral and water is small at magmatic temperatures ( $>800^\circ\text{C}$ ), the  $\delta^{18}\text{O}$  values calculated for magmatic water

agree with those of the coexisting magma or are slightly lighter ( $<1.0\text{‰}$ ) (Matsuhisa et al., 1979). The  $\delta^{18}\text{O}$  values of the granitic rocks near the Chandmani Uul deposit obtained in this study range from 3.9 to 7.5‰ ( $n = 7$ ), as shown in Table 2.1 and Fig. 2.15. When the  $\delta^{18}\text{O}$  values of the magmatic water was controlled by that of granitic magma, the magmatic fluid responsible for the Chandmani Uul deposit exhibits  $\delta^{18}\text{O}$  values similar to those of granitic rocks. Some of the values fall within the range for normal magmatic water ( $\delta^{18}\text{O} = 5.5 - 10.0\text{‰}$ ), and the rest are slightly lighter (Fig. 2.15). The granitic rocks in the study area were hydrothermally altered and particularly suffered from strong sericite and/or potassic alterations (Fig. 2.7g–i). Although the oxygen isotope behavior during the hydrothermal alteration of granitic rock is variable, the  $\delta^{18}\text{O}$  values of the altered granitic rocks commonly shift to lighter values (Taylor, 1974, 1997; Barker et al., 2013).

The chemical index of alteration (CIA) (Nesbitt & Young, 1982) for the granitic rocks in this study was calculated as follows:

$$\text{CIA} = \text{Al}_2\text{O}_3 / (\text{Al}_2\text{O}_3 + \text{CaO}^* + \text{Na}_2\text{O} + \text{K}_2\text{O}) \times 100 \text{ (in molecular proportions),}$$

where  $\text{CaO}^*$  is the amount of  $\text{CaO}$  incorporated in the silicate fraction. Figure 2.10h shows the relationship between the CIA and  $\delta^{18}\text{O}$  values of the granitic rocks, where a weak negative correlation is recognizable and the less altered rocks are isotopically heavier. The CIA of granitic rocks suggests that less altered granitic rock has  $\delta^{18}\text{O}$  values similar to those of the magmatic fluid associated with normal granitoids. Therefore, it can be inferred that the magmatic water associated with the formation of the Chandmani Uul deposit had  $\delta^{18}\text{O}$  values similar to those of normal magmatic water ( $\delta^{18}\text{O} = 5.5 - 10.0\text{‰}$ ).

Several types of water have lighter  $\delta^{18}\text{O}$  values outside of the range for

magmatic water, such as seawater, meteoric water, and metamorphic water. The oxygen isotope compositions of ancient seawater have been determined previously using indirect methods such as calculating the effects of ice cap melting or analyzing minerals that were formerly in equilibrium with seawater (Sheppard, 1986). In addition, analyses of carbonates, cherts, phosphorites, and glauconites from marine sediments of different ages have revealed  $\delta^{18}\text{O}$  trends over time (Knauth & Lowe, 1978; Shemesh et al., 1983; Knauth & Roberts, 1991; Jaffrés et al., 2007; Armendáriz et al., 2013). Specifically, the  $\delta^{18}\text{O}$  values of seawater was found to increase progressively from the Archean ( $\delta^{18}\text{O} = -8 - -12\text{‰}$ ) to the present ( $0\text{‰}$ ). The oxygen isotope composition of meteoric precipitation is controlled by complex mechanisms involving geographic and climatic parameters e.g., latitude, elevation, distance from coast, humidity including surface air temperature (Dutton et al., 2005). Since these mechanisms have not changed significantly over geological time, the  $\delta^{18}\text{O}$  value of local meteoric water should increase from the Archean in a manner similar to that of seawater.

The  $\delta^{18}\text{O}$  values of modern meteoric water in southern Mongolia are light values ranging from  $-5$  to  $-20\text{‰}$  (Sturm et al., 2017). These values are not directly applicable to Cambrian ore-forming environments. However, it is unique for meteoric water to have a light  $\delta^{18}\text{O}$  value, so the participation of meteoric water during the precipitation of ore minerals is likely. The involvement of meteoric water is a well-established idea especially for magmatic–hydrothermal deposits formed in levels near the surface, such as epithermal and porphyry Cu–(Au) deposits (e.g., Robb, 2005). Meteoric components also play important roles for hydrothermal deposits formed near granitic intrusions, especially for the middle to late

mineralization stages of porphyry Mo–W deposits (Shu & Lai, 2017; Li et al., 2019) and skarn deposits (Öztürk et al., 2008; Oyunjargal et al., 2019).

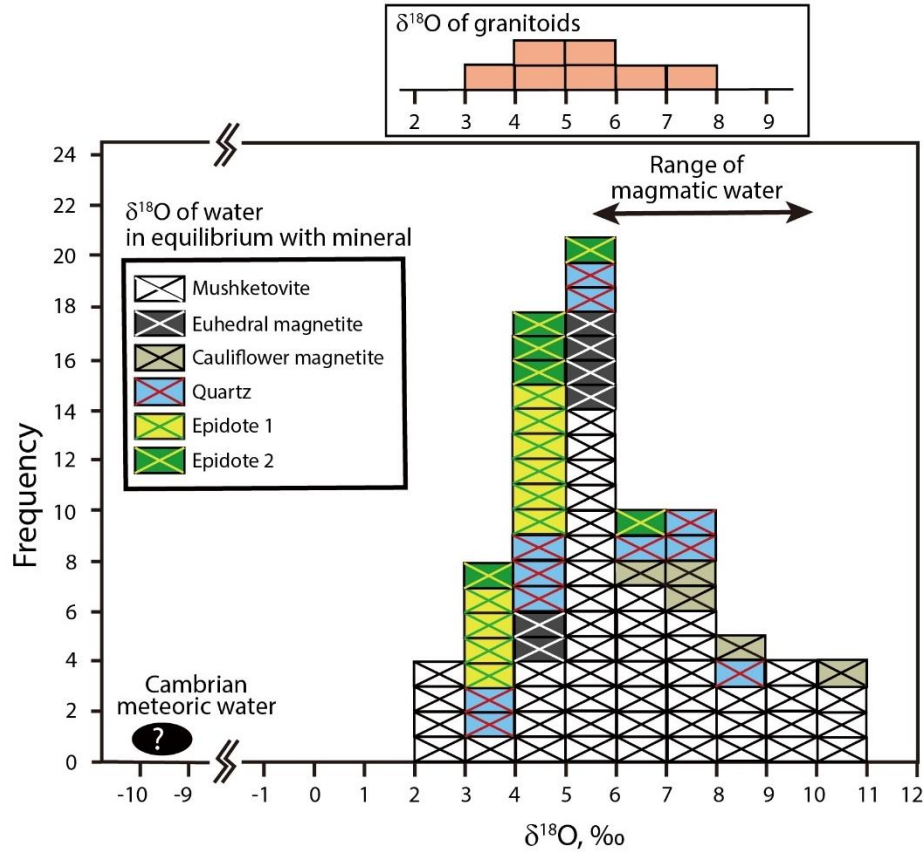


**Fig.2. 15**  $\delta^{18}\text{O}$  values of water estimated from those of the constituent minerals and fractionation factor of oxygen isotope between minerals and water at 300°C. The range for magmatic water is from Taylor (1997). The oxygen isotope values of the granitic rocks in the study area are shown. The abbreviations are same as those in Fig. 2.14.

### 5.3. Comparison with other IOCG deposits

Since the first formal proposal of IOCG deposits by Hitzman et al. (1992), numerous geological, mineralogical, and geochemical data have been collected from IOCG deposits worldwide. Although several classification methods have been proposed (Sillitoe, 2003; Williams et al., 2005; Groves et al., 2010; Chen, 2013),

the common features of IOCG deposits can be summarized as follows: 1) the presence of Cu with or without Au as an economic metal, 2) the existence of hydrothermal veins, breccia, and/or replacement ore styles accompanied by structural control, 3) regional Na–Ca alteration and subsequent potassic alteration, 4) abundant magnetite and/or hematite, 5) iron oxides with Ti contents lower than those in most igneous rocks, and 6) the absence of any clear spatial association with igneous intrusions. The mineralization style of the Chandmani Uul deposit exhibits these features, and several of them are compared with typical IOCG provinces in South America as summarized in Table 2.6

#### **5.3.1. Tectonic setting and related igneous rocks**

In northern Chile, several IOCG deposits are distributed within a belt of ~5 km wide and >20 km long along the Atacama fault system, which stretches over 1,000 km along the Chilean coast. The Atacama fault zone is a subduction-linked arc-parallel strike-slip fault system that has been active at least since the Jurassic (Scheuber & Andriessen, 1990; Scheuber et al., 1995; Cembrano et al., 2005; Arévalo, et al., 2006). This fault system controlled the mineralization of many of the iron deposits in the Chilean iron belt (Bookstrom, 1977; Ménard, 1995; Oyurzún et al., 2003; Rieger et al., 2010). The south-central Peruvian IOCG province in the Cañete basin hosts several deposits, and the distribution of these deposits is controlled by four principal fault systems (Atherton & Aguirre, 1992; Chen et al., 2010). The Carajás Mineral Province (CMP) in Brazil, in the southeastern portion of the Amazonian Craton, is known to host a series of large IOCG deposits. These deposits are located in the same NW–SE striking shear zone in the Itacaúnas Shear



Belt in the southern sector of the CMP (Torresi et al., 2012). These examples suggest that the distribution of IOCG deposits is controlled by the regional tectonic stress field. Although, the Chandmani Uul deposit is located in the stress field of the MML, the active movement of this fault zone occurred during the Phanerozoic. There is no direct evidence relating the MML to mineralization. Since the area investigated in this study is located in the geologically active domain of the eastern CAOB, the intrusion of Cambrian granitic rocks must have been influenced by this stress field.

The IOCG deposits in northern Chile are located tectonically in a continental margin arc setting, and those in Carajás in Brazil may be located in the same setting, although the ages of the granitic rocks associated with mineralization are Mesozoic for northern Chile and Archean for Carajás (Pollard, 2006). These granitic rocks are plotted in different regions as shown in the discrimination diagram of Pearce et al. (1984). The paleozoic granitic rocks in this study belong to a field of volcanic arc granitoid, similarly to the rocks from northern Chile (see Fig. 2.10).

### **5.3.2. Wall rock alteration**

The hydrothermal alteration found in IOCG-style mineralization is characterized by regional Na–Ca alteration, which usually accompanies the formation of albite (and scapolite). The regional Na–Ca alteration extends around the Salobo and Sossego deposits in the CMP (Monteiro et al., 2008) and the Candelaria–Punta del Cobre deposits in northern Chile (Marschik and Fontboté, 2001; Williams et al., 2005). Albite–scapolite alteration has been confirmed in the Marcoa deposit, while this alteration type is indistinct in the neighboring Mina Justa

deposit in the Cañete basin, Peru (Chen et al., 2010). The Na–Ca alteration has not been confirmed in the Chandmani Uul deposit, except for the epidote alteration enveloping the adjacent ore body. The lack of Na alteration can be inferred from the chemical composition of the granitic rocks. The Na<sub>2</sub>O versus K<sub>2</sub>O plot (Fig. 2.10g) demonstrates that the granitic rocks in the study area are not enriched with Na<sub>2</sub>O, while most of the igneous rocks related to IOCG deposits in the Chilean coastal belt show Na<sub>2</sub>O enrichment during hydrothermal alteration. The granitic rocks of the Chandmani Uul area underwent slight K<sub>2</sub>O enrichment.

A potassic alteration zone is developed in the deep level, and the shallow zones are characterized by the development of sericite and sericite–chlorite alteration zones in the Chandmani Uul deposit. These alteration zones are similar to those in the middle stages of the Marcona deposit in Peru (Chen et al., 2010, 2011), the Mantoverde deposit in Chile (Benavides et al., 2007), and the Alvo 118 deposit in the CMP (Torresi et al., 2012). In the summary of the genetic model of IOCG deposits worldwide by Chen (2013), the expanse of hydrothermal alteration around a deposit was described as follows. Regional Na–Ca alteration commonly precedes mineralization, and potassic and sericite–chlorite alterations subsequently occur, simultaneously with metallic mineralization. A potassic alteration zone develops at intermediate depth, and the shallow zone is dominated by a sericite–chlorite alteration zone. The alteration zones around the Chandmani Uul deposit are relatively shallow examples of IOCG deposits.

### **5.3.3. Ore mineralogy**

The dominant ore mineral in IOCG deposits may be iron oxide, magnetite,

and/or hematite. The Marcona and Mina Justa deposits are located near the Cañete basin, south-central Peru. Although the mineralization ages of these deposits are different (~160 Ma for Marcona and ~100 Ma for Mina Justa), major hematite mineralization took place only at the Mina Justa where mineralization occurred at a shallow level (Chen et al., 2010, 2011). High oxygen fugacity ( $fO_2$ ) environments accompanying hematite (mushketovite) are common in deposits formed at shallow levels, such as the Mantoverde (Benavides et al., 2007) and Alvo 118 (Torresi et al., 2012) deposits. The iron oxide ores dominated by mushketovite in the Chandmani Uul deposit have similarities to those in the aforementioned deposits.

Magnetite is known to host several impurity elements such as Si, Al, Cr, Ti, V, Mn, Mg, Ca, Zn, Cu, Ni and Co. The chemical compositions of the magnetite in this study are shown in Table 2.4, where the maximum contents of impurity elements are as follows:  $SiO_2$  (3.1 wt%),  $Al_2O_3$  (0.9 wt%),  $TiO_2$  (0.1 wt%), MnO (0.1 wt%), MgO (0.2 wt%), CaO (0.7 wt%), ZnO (0.1 wt%) and CuO (0.1 wt%). Elements such as Cr, V, Ni, and Co were under the detection limit of EPMA. The trace elements contents in magnetite differ based on the type of mineral deposit (Dupuis & Beaudoin, 2011; Dare et al., 2014; Nadoll et al., 2014; Knipping et al., 2015; Heidarian et al., 2016; Huang et al., 2019). Recently, silician magnetite containing up to 7.5 wt% of  $SiO_2$  was reported from the Copiapó Nordeste IOCG prospect, northern Chile (González et al., 2018). González et al. (2018) stated that the  $SiO_2$  content in magnetite is influenced by the fluid temperature and salinity, because the solubility of silica is also controlled by the temperature and salinity (Monecke et al., 2018). The intermediate Si content of the magnetite in this study is consistent with an intermediate magnetite precipitation temperature near ~300°C.

According to the discrimination diagram proposed by Nadoll et al. (2014), the magnetite from this study overlaps the fields of IOCG and skarn deposits. Since a similar compositional range of magnetite was found in the Copiapó Nordeste IOCG prospect (González et al., 2018), the composition of magnetite from IOCG deposits can vary widely, as demonstrated by Nadoll et al. (2014).

#### **5.3.4. Source of ore-forming fluid**

The source of the ore-forming fluid of IOCG deposits has been discussed based on the stable isotopes (chlorine, oxygen, and sulfur) and salinity of fluid inclusion (Barton & Johnson, 1996; Barton, 2014). Most deposits have multiple fluid sources (Table 2.6). Although magmatic fluid is dominant in the mineralization of iron oxide in most deposits (Rieger, et al., 2012), the very high salinity of fluid inclusion and heavy  $\delta^{34}\text{S}$  values of sulfide minerals suggest the infiltration of modified seawater, possibly via evaporite sediments or basinal water, in numerous deposits. The involvement of nonmagmatic fluids is important for the middle- to late-stage fluid responsible for Cu and Au mineralization in South American deposits (Marschik & Fontboté, 2001; Chiaradia et al., 2006; Benavides et al., 2007; Torresi et al., 2012). Meteoric water is also responsible for late-stage mineralization (Chen et al., 2011). Relatively light  $\delta^{18}\text{O}$  values of water are evident for some mushketovite and late-stage epidote, which suggests the infiltration of nonmagmatic fluid into the Chandmani Uul deposit. As certain data suggestive of the infiltration of modified seawater have not been obtained, meteoric water is the most probable candidate.

Genetical connection between iron oxide–apatite (IOA) mineralization and

IOCGs has been revealed by recent studies. This new model is based on evidences that come from trace elements chemistries of magnetite (Knipping et al., 2015; Simon et al., 2018; Rojas et al., 2018) and apatite (La Cruz et al., 2019), and iron isotopic values (Knipping et al., 2019). Since the dominant iron oxide mineral of this study is mushketovite, originally precipitated as hematite rather than magnetite, the data obtained in this study is not linked to aforementioned model. The  $\delta^{18}\text{O}$  values obtained both from mushketovite and magnetite in this study cover wide range of  $-5.9 - 2.8\text{‰}$  (Table 2.5). Distribution nature of the  $\delta^{18}\text{O}$  values of this study is obviously different from the  $\delta^{18}\text{O}$  values of magnetite from most IOA deposits (Tornos et al., 2016; Troll et al., 2019).

## **6. Conclusions**

The geological, mineralogical, and geochemical characteristics of the Chandmani Uul deposit, which is the first documented occurrence of IOCG-style mineralization in Mongolia, can be summarized as follows.

1. The Chandmani Uul biotite-diorite, granodiorite, granite intruded in the southwestern part of the Shar Zeeg formation in the study area, and the zircon U-Pb LA-ICP-MAS data from this intrusion yield age of  $426 \pm 5.3$  to  $544 \pm 9.3$  Ma which is consistent with ore-formation age.
2. Iron oxide ores are hosted in the andesitic rocks of the Shar Zeeg Formation from Neoproterozoic to Lower-Cambrian in age. Middle- to Upper-Cambrian bodies of granitic rocks have intruded into the andesitic rocks. The wall rocks around the iron oxide ore body were hydrothermally altered to form potassic, epidote, and sericite–chlorite alteration zones, and calcite and quartz veinlets were

ubiquitous in the late-stage. Granitic rocks also underwent potassic alteration, which suggests that the ore deposit was formed in relation with the activity of granitic rocks.

3. The ore mineral assemblage is dominated by mushketovite, euhedral magnetite with concentric and oscillatory zoning textures, and cauliflower magnetite with minor chalcopyrite and pyrite. Mushketovite is the most dominant iron phase as prismatic aggregation with grain sizes of 0.2 – 3 mm, and is distributed throughout the deposit. Euhedral magnetite appears in limited amounts at relatively shallow levels in the deposit. Cauliflower magnetite appears locally in the deeper parts of the deposit in association with green-colored garnet and calcite. Sulfide minerals are ubiquitously associated with iron oxides.

4. The  $\delta^{18}\text{O}$  values were obtained for all types of magnetite, quartz, and epidote and were found to be -5.9 – 2.8 ‰, 10.5 – 14.9 ‰, and 3.6 – 6.6 ‰, respectively. The oxygen isotope values of the quartz–magnetite pairs give equilibrium isotopic temperature of near 300°C. The  $\delta^{18}\text{O}$  values for the water responsible for all types of magnetite were calculated at 300°C and ranged from 2 to 10 ‰.

5. The geological, mineralogical, and geochemical data obtained in this study suggest that the iron oxide deposit in the Chandmani Uul is a typical IOCG deposit. This deposit was formed at an intermediate depth with potassic and sericite–chlorite alteration zones under the oxidized conditions of hematite-stable environment. The ore-forming fluid was supplied by granodioritic magma with a significant contribution of meteoric water.

## **Chapter 3: Oxygen Isotopic Study on the Date-Nagai Skarn-Type Tungsten Deposit, Northeastern Japan**

### **1.Introduction**

Skarn deposits are typically formed as a result of three sequential processes (Einaudi et al., 1981; Meinert, 2005); isothermal contact metamorphism during the early stages of plutonic magma emplacement and solidification, followed by open system metasomatism. Open system metasomatism is generally characterized by two distinctly different styles. The early prograde stage is characterized by the precipitation of anhydrous minerals such as wollastonite, garnet and pyroxene, which forms in the presence of relatively high-temperature fluid. Si, Al and Fe, as well as other components, are introduced into the calcareous sediments by high temperature aqueous fluid, while Ca, Mg and CO<sub>2</sub> are locally derived and also introduced into the metasomatic system. The later retrograde stage is characterized by the precipitation of hydrous minerals, such as epidote, amphibole and chlorite plus sulfides, which forms in the presence of lower-temperature fluid. These two stages have been commonly thought to reflect the dominance of magmatic and meteoric water, respectively (Bowman et al., 1985a, b; D'Errico et al., 2012; Nokleberg, 1981; Taylor & O'Neil, 1977). Among ore minerals commonly accompanied in skarn deposits, magnetite and scheelite precipitate in the prograde stage of metasomatism (Brown & Essene, 1985; Collins, 1977; Newberry & Swanson, 1986; Robb, 2005). However, there are examples that scheelite and sulfide ore minerals occur as disseminations or veins that cut prograde assemblages (Mathieson & Clark, 1984).

The Date-Nagai deposit is a small-scale skarn deposit producing scheelite ore. The skarn of this deposit develops along the contact between marble and pelitic hornfels, which merely constitutes the remaining hornfels body as a roof pendant on the granodiorite batholith (Fig. 3.1b). Granodiorite is extensively distributed at least 5 km in circumference from the deposit, except nonconformably overlain by younger volcanic rocks. The granodiorite is the most probable source of skarn- and ore-forming fluids at this deposit. The granodiorite belongs to the ilmenite series, and pegmatite and aplite veins are accompanied; therefore, its emplacement depth is likely to be deep in general sense. The geological environment of the Date-Nagai deposit is one of the best examples to examine the characteristics of prograde stage metasomatism. In this short communication, we examine the occurrence, composition and oxygen isotope of skarn minerals, and discuss the origin of skarn-forming fluid.

## **2.Geology**

The Date-Nagai deposit is located in the northern part of the Abukuma mountains, approximately 20 km east from Fukushima city (Fig. 3.1a), and is halfway along the road connecting the cities of Fukushima and Soma. The Ishida river runs approximately in the EW direction of the study area, and both banks of the river are occupied with gentle mountains with an altitude of 300-500 m. The highest peak of the area is Mt. Ryozen (825 m) (Fig. 3.1b), a Miocene volcano, which is located ca. 6 km northeast of the deposit.

Most of the study area is covered with Cretaceous granodiorite, which is distributed widely in the Abukuma mountains. Paleozoic sedimentary rocks remain



locally on granodiorite as a roof pendant (Fig. 3.1b) and have changed to hornfels and marble as a result of thermal metamorphism. Skarn that accompanies tungsten mineralization develops along the contact between pelitic hornfels and marble.

The granodiorite body, known as the Idateyama body, belongs to the ilmenite-series and has an intrusion age of 102-106 Ma (METI, 1987). The dominant minerals of granodiorite are quartz, plagioclase and biotite, accompanied by lesser amounts of K-feldspar and hornblende. A large amount of biotite of ca. 5 mm in size is characteristic in the Idateyama body. Quartz veins of ca. 30 cm in width and pegmatite veins occasionally cut the granodiorite. A xenolith of fine-grained granite is rarely found in granodiorite.

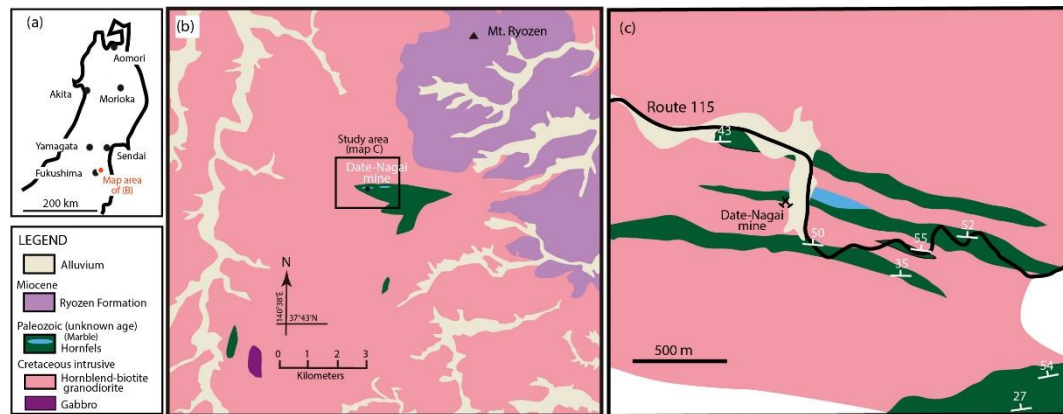


**Fig.3. 1** Geological map of the study area. a) Location of the Date-Nagai deposit in northeastern Japan. b) Regional geological map of the study area (modified after Kubo et al., 2014). c) Detailed geological map around the Date-Nagai deposit.

Hornfels crops out mostly along the Ishida river as EW extended lenticular masses of ca. 70 m in maximum thickness (Fig. 3.1c). The hornfels have remarkable schistosity, and biotite crystals are arranged parallel to the schistosity plane. The dominant minerals of the hornfels are biotite, cordierite and quartz, with trace

amounts of plagioclase. A lenticular marble bed with a maximum thickness of 35 m appears in hornfels in the vicinity of the Date-Nagai deposit. The texture of the marble is massive without cristallinity. The Miocene Ryozen formation nonconformably overlays the granodiorite at the northeastern area (Fig. 3.1b). This formation is composed of Lahal sediments of basaltic tuff breccia. The age of the Ryozen formation is estimated to be 16-15 Ma (Yamamoto, 1996; Yamamoto & Hoang, 2009).

### **3.Ore deposit**

Scheelite-bearing tungsten ore was produced from the deposit for 24 years between 1964 and 1988 with an annual production of ca. 600 t with ca. 1.5% WO<sub>3</sub>. Scheelite is hosted in the skarn zone that is developed along the contact between pelitic hornfels and marble. The highest level of the mine is 250 m above sea level, and an inclined shaft with an oblique angle of ca. 45° continues down to 180 m above sea level. Figure 3.2a shows an underground geological map of the Date-Nagai deposit. Although an irregular distribution of skarn is shown on the geological map, skarn develops as a layer between hornfels and marble, as shown in the cross section along the inclined shaft (Fig. 3b). The thickness of the skarn is varied and has a maximum thickness of 4.0 m. Aplite dyke cuts the wall rock and skarn, as shown in cross section. The thickness of the skarn increases toward the contact with the aplite dyke. The aplite is a pale yellowish-green compact rock mostly composed of quartz with trace amounts of plagioclase. Small amounts of garnet and clinopyroxene are included in aplite in the vicinity of the contact with the skarn.

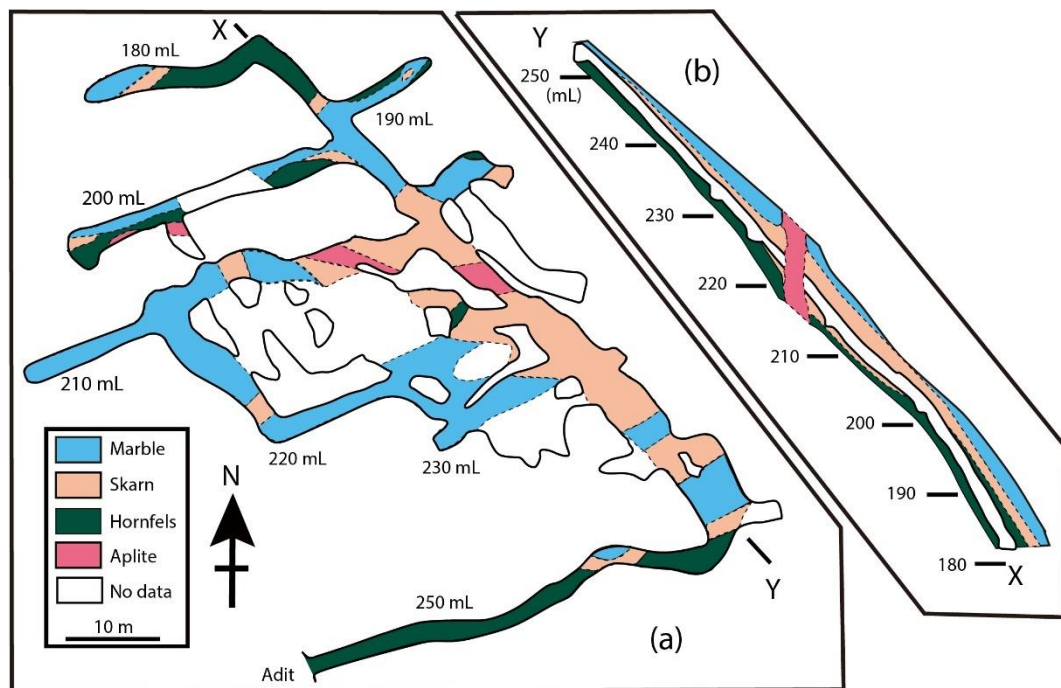


**Fig.3. 2** a) Underground geological map and b) cross section of the Date-Nagai deposit.

### 3.1. Occurrence of skarn

A zonal arrangement of minerals is observed in the skarn (Fig. 3.3a). The zonation consists of 1) wollastonite, 2) garnet, 3) vesuvianite-garnet, and 4) garnet-epidote zones from marble to hornfels. A lack of certain zones and a reversed distribution of zones are occasionally found. The widths of the wollastonite, garnet and vesuvianite-garnet zones are several 10 cm, while that of the garnet-epidote zone is 1-3 m. The characteristics of each skarn zone are as follows.

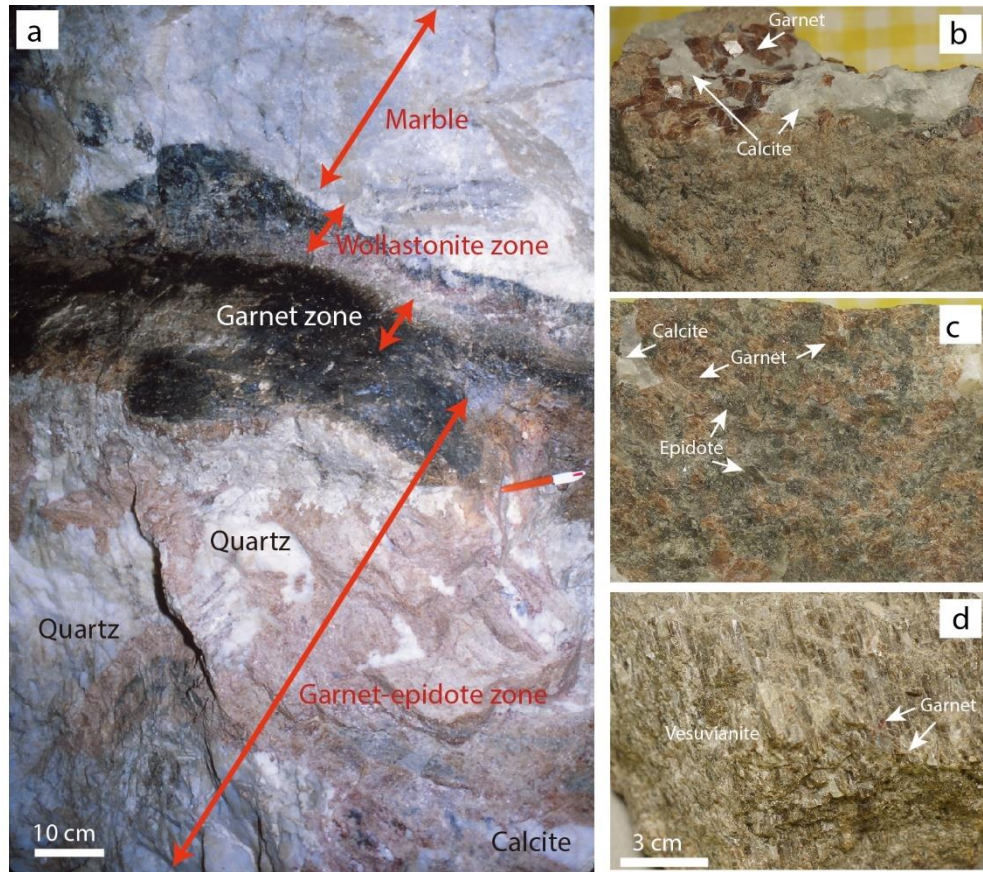


**Fig.3. 3** Occurrence of skarn zones of the Date-Nagai deposit. a) Underground photo of skarn at the contact of marble. b) Hand specimen sample of garnet zone. Euhedral garnet is covered with calcite in druse. c) Hand specimen sample of garnet-epidote zone. d) Hand specimen sample of vesuvianite-garnet zone. Prismatic crystals of vesuvianite associates with garnet.

**Wollastonite zone:** The Wollastonite skarn has a width of 1 to 15 cm and is a light brown to white color. This zone is brittle and clayey when it contains water. The dominant mineral in this zone is wollastonite, accompanied by small amounts of clinopyroxene, calcite and quartz.

**Garnet zone:** The Garnet zone is <15 cm thick and is dominated by reddish brown euhedral to subhedral garnet. Euhedral to subhedral garnet is the main constituent of this zone, and accessory amount of clinopyroxene accompanies. Small amounts of euhedral vesuvianite and fine-grained scheelite, epidote and calcite precipitated

to surround or fulfill fracture within garnet. The garnet zone gradually changes to the following vesuvianite-garnet zone with an increase in the amount of vesuvianite. Vesuvianite-garnet zone: The thickness of this zone is varied from several cm up to 40 cm and its horizontal continuity is poor. This zone appears irregularly in garnet-epidote zone. A large amount of euhedral vesuvianite and lesser amounts of garnet, calcite and quartz are included. Columnar vesuvianite of 1 to 2 cm in length arranges its c-axis vertical to the contact plane between the mineral zones (Fig. 3.3d). Under an optical microscope, granular garnet crystals of ~50  $\mu\text{m}$  in size are included in vesuvianite crystal. Intergranular spaces among vesuvianite is filled by scheelite, epidote, calcite and quartz (Fig. 3.4k, l). Arrangement of scheelite crystals with grain size < 1 mm along the grain boundary of vesuvianite is well observed under ultraviolet light (Fig. 3.4d).

Garnet-epidote zone: This zone is the widest among mineral zones at 1 to 3 m thick. The constituent minerals of this zone are difficult to distinguish in hand specimens because the minerals do not appear in the bulk, except in rarely observed euhedral garnet in a druse (Fig. 3.3b). Under an optical microscope, euhedral to subhedral garnet crystals with <1 cm in size aggregate, which show optical anisotropy (Fig. 3.4a). The replacement of garnet from its perimeter by euhedral scheelite (up to 3 mm in size), epidote, calcite and quartz is commonly observed (Fig. 3.4e). Scheelite is often surrounded by thin film of epidote when it associates with garnet (Fig. 3.4f, h).

Paragenetic sequence of skarn is constructed from the observation of hand specimens and optical microscopic petrography of thin sections as shown in Fig. 3.5.

### **3.2. Occurrence of scheelite**

Scheelite, the only ore mineral of the deposit, appears in the garnet, vesuvianite-garnet (Fig. 3.4c and D) and garnet-epidote zones (Fig. 3.4b and d). Scheelite occurs mostly as fine dispersed crystals among skarn minerals; however, greater amounts of scheelite are included in the garnet-epidote zone. Euhedral to subhedral crystals of scheelite with grain sizes of 2-3 cm are often found in the garnet-epidote zone, while the grain size of scheelite is smaller in the vesuvianite-garnet zone (Fig. 3.4d). In hand specimens, scheelite appears to associate with garnet; however, scheelite crystals are associated intimately with calcite, epidote and vesuvianite from microscopic observation (Fig. 3.4f, h, j and l). Scheelite is rimmed by a thin epidote layer when it is included in garnet crystal. The paragenetic sequence of minerals suggests that scheelite was precipitated during the middle stage of skarn formation (Fig. 3.5).



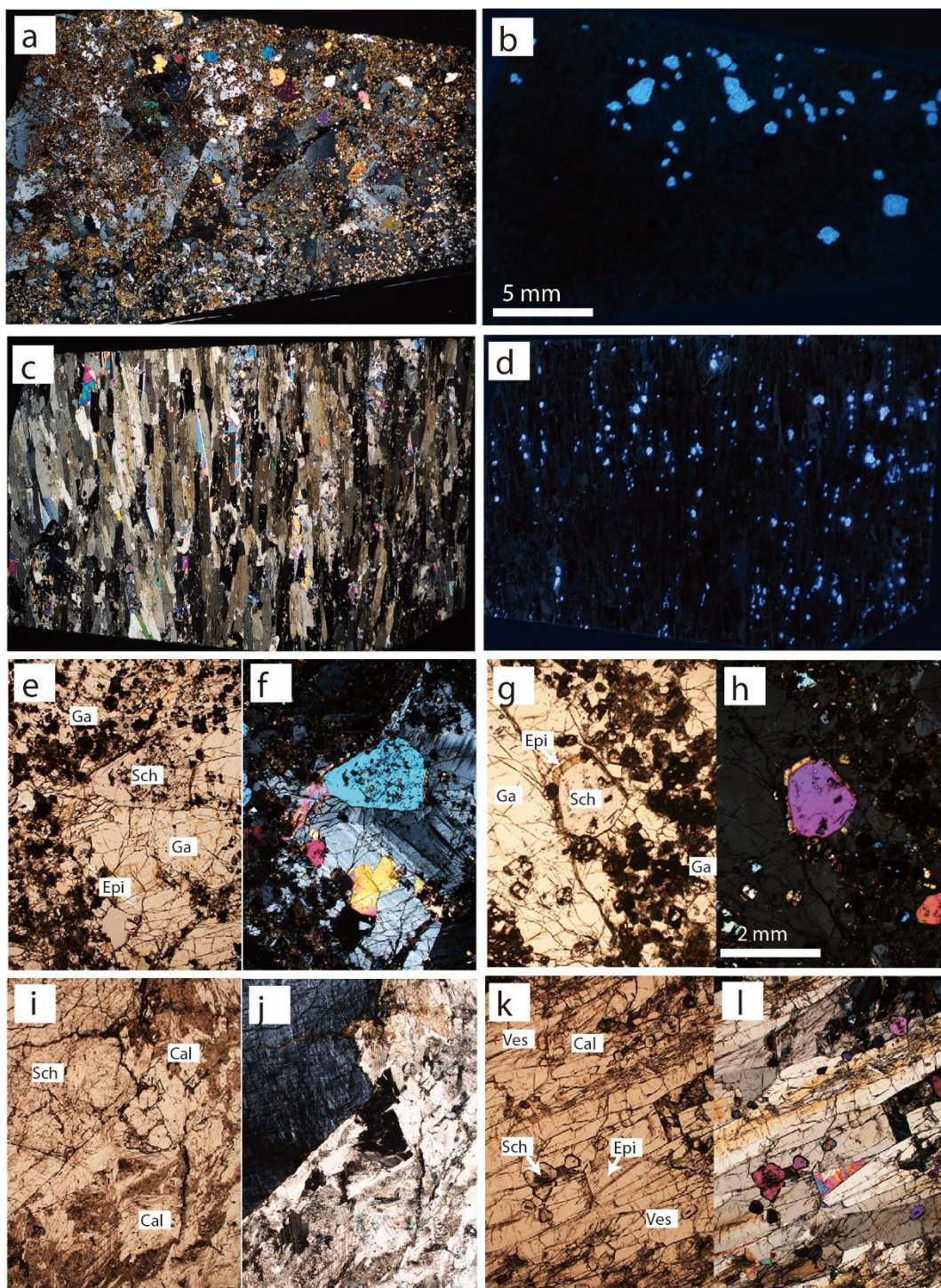


**Fig.3. 4** Macrographs of tungsten ores. a, b) Garnet-epidote zone. c, d) Vesuvianite-garnet zone. Micrographs of e-j) Garnet-epidote zone, k, l) Vesuvianite-garnet zone. a, c) Crossed nicols under polarized light. b, d) Fluorescence color of scheelite under ultraviolet light. e, g, i, k) Open nicols under polarized light, and f, h, j, l) crossed nicols under polarized light. Ga, garnet; Epi, epidote; Ves, vesuvianite; Sch, scheelite.

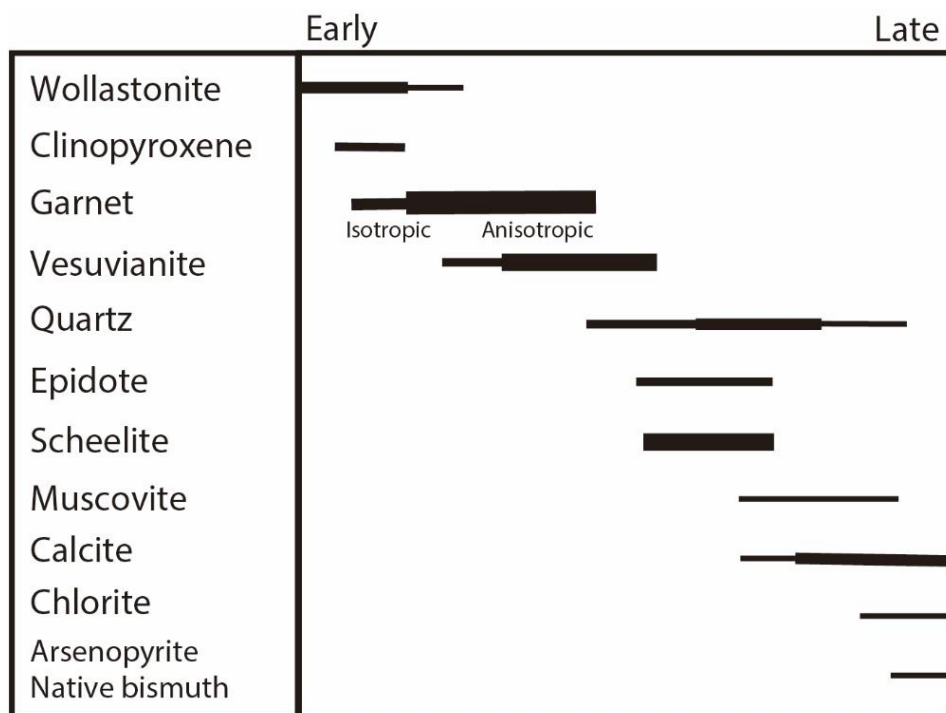


**Fig.3. 5** Paragenetic sequence of minerals. Thickness of bar indicates relative abundance of minerals.

#### 4. Chemical compositions of skarn minerals

Qualitative and quantitative analyses of the chemical compositions of minerals were made using electron probe microanalysis (EPMA; JEOL, JXA-8621) with an acceleration voltage of 15.0 kV and a specimen current of  $1.0 \times 10^{-8}$  A. The diameter of the electron beam was ca. 5.0  $\mu\text{m}$ . After background correction, the chemical compositions of minerals were calculated by the ZAF method. Analytical results for garnet and clinopyroxene are given in Table 3.1 and 3.2, respectively.

**Garnet:** Garnet is the most abundant mineral in the skarn of this study. Optically isotropic and anisotropic garnets were observed (Fig. 3.4a, f, and h); isotropic garnet precipitated in earlier stage (Fig. 3.5). The molal contents of endmembers are calculated on the basis of total oxygen =24 (Table 3.1), and are plotted in a ternary diagram (Fig. 3.6a). As shown in Fig. 3.6a, garnets of this study correspond



to a grossular-pyralspite series; the molal amount of andradite is low (<20%). The molal contents of grossular in each skarn zone are 63-88% in the garnet zone, 25-66% in the vesuvianite-garnet zone, and the 29-60% in garnet-epidote zone. Thus, the molal content of grossular decreases from the contact with marble toward hornfels. The chemical compositions of garnet from world skarn deposits summarized by Meinert et al. (2005) are superimposed in Fig. 3.6a. Garnets from the present study are characterized by a very low andradite content. The optical nature of the garnet correlates with the chemical composition; garnets with a molal pyralispite content of >20% exhibit anisotropy. Among the pyralispite, the content of pyrope is negligible and the almandine/spessartine ratio varies (Table 3.3).

Clinopyroxene: Chemical compositions of clinopyroxene are shown in Table 3.2 and plotted in Fig. 3.6b. These constitute a diopside-hedenbergite series, and the molal content of johannsenite is low (<5.0%).

Scheelite: Scheelite ( $\text{CaWO}_4$ ) is known to form a solid solution with powellite ( $\text{CaMoO}_4$ ). The fluorescence color of the scheelite in this study under ultraviolet light was light blue (Fig. 3.4b and d); therefore, the powellite content is considered to be low. Analytical results for scheelite from vesuvianite-garnet and garnet-epidote zones shows that the molal content of powellite in scheelite is very low (<1.5%, n=24).

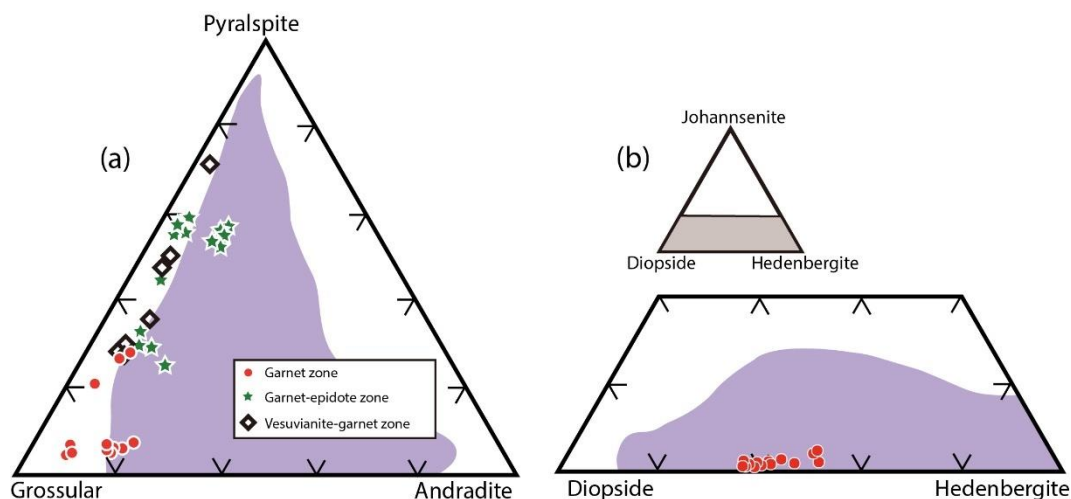


Figure 6

**Fig.3. 6** Chemical compositions of garnet and clinopyroxene. a) Plots of garnet in the grossular-andradite-pyralspite ternary system. b) Plots of clinopyroxene in the diopside-hedenbergite-johannsenite ternary system. Calculation of endmember compositions of garnet and clinopyroxene is after Deer et al. (1992). Compositions of garnet and clinopyroxene from world W-skarn deposits (Meinert et al., 2005) are also shown as purple color domains.

## 5.Oxygen isotope

Mineral grains were hand-picked from slabs of skarn under a binocular microscope. The grain size of most samples used in this study was large (>1 mm), so purities of the mineral separates were better than 95%.

Oxygen was extracted from the skarn minerals using a 17 Watt JLC-200 CO<sub>2</sub> laser ( $\lambda = 10.6 \mu\text{m}$ ) and BrF<sub>5</sub> using a fluorination method similar to that described by Hayashi et al. (2001). Approximately 2 mg grain of skarn mineral was placed in a hole drilled in a Ni rod placed in a reaction cell under a BrF<sub>5</sub> atmosphere of ca. 110 mm Hg pressure. The CO<sub>2</sub> laser beam was focused to ca. 25  $\mu\text{m}$  in diameter and then irradiated through a BaF<sub>2</sub> window. Completion of reaction between the mineral and BrF<sub>5</sub> was confirmed by observation of the reaction under a microscope

positioned co-axially with the CO<sub>2</sub> laser. Oxygen extracted from the minerals was converted to CO<sub>2</sub> quantitatively in a reaction with heated diamond. Completion of the reaction was evaluated by measuring the amount of CO<sub>2</sub> released from the minerals. The isotopic compositions of the CO<sub>2</sub> were measured using a mass spectrometer (Thermo-Finnigan MAT 253). The <sup>18</sup>O/<sup>16</sup>O ratios are expressed in the conventional  $\delta^{18}\text{O}$  notation relative to Vienna standard mean ocean water (VSMOW). The accuracy of CO<sub>2</sub>-laser fluorination oxygen isotope analyses was evaluated by repeated analysis of working standards. The  $\delta^{18}\text{O}$  value of the reference quartz (NBS 28,  $\delta^{18}\text{O}=9.6\text{‰}$ ) was measured with each sample. The reproducibility of the  $\delta^{18}\text{O}$  values was better than 0.2‰ (Hayashi et al., 2001).

Oxygen isotope values of garnet, vesuvianite, scheelite, quartz and muscovite in the garnet, vesuvianite-garnet and garnet-epidote zones were obtained and are given in Table 3.3 and plotted in Fig. 3.7. The  $\delta^{18}\text{O}$  values varied by 4.2-7.7‰ (n=33) for garnet, 5.9-6.9‰ (n=5) for vesuvianite, -0.3-3.4‰ (n=15) for scheelite, 6.0-10.9‰ (n=10) for quartz and 8.2‰ (n=1) for muscovite.

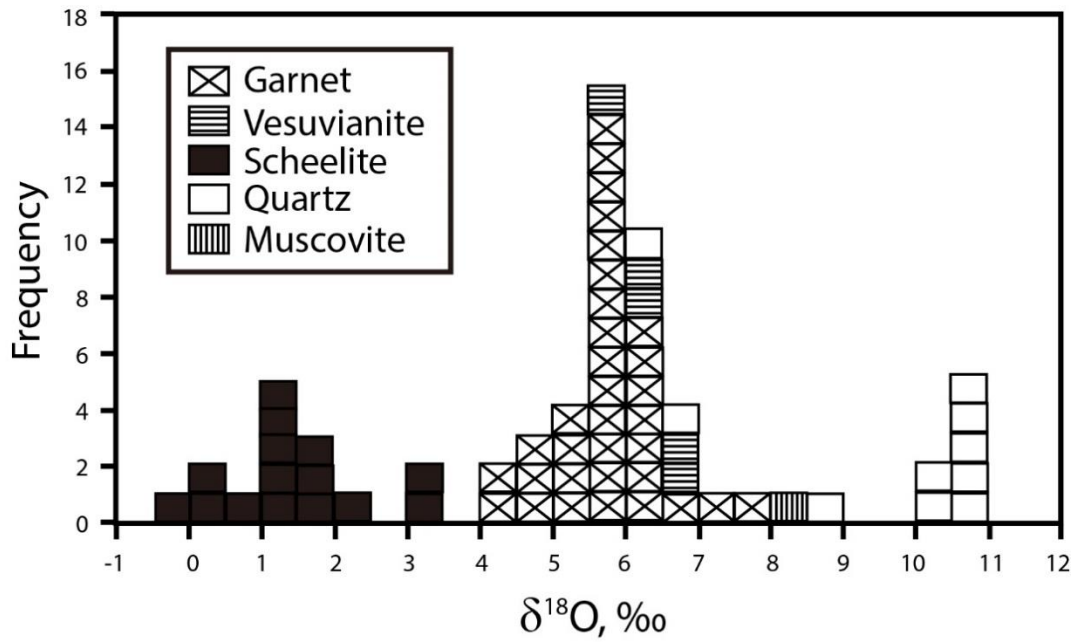


**Fig.3. 7** Oxygen isotope values of garnet, vesuvianite, scheelite, quartz and muscovite.

## 6. Discussion

### 6.1. Oxygen isotope value of skarn-forming fluid

Temperature information is indispensable to calculate  $\delta^{18}\text{O}$  values of fluid responsible for skarn formation. Therefore, we attempted to find fluid inclusion applicable for microthermometric measurement of the filling temperature; however, the samples in this study did not have adequate fluid inclusions. The temperature of skarn-forming fluid was calculated using  $\delta^{18}\text{O}$  for skarn minerals and an equilibrium fractionation factor between minerals (Matthews et al., 1983; Thomas et al., 2001). Several combinations of mineral pairs were possible in this study; however, only quartz-scheelite was an applicable pair.

The equilibrium fractionation factors ( $1000\ln\alpha$ ) for oxygen isotopes used in this study were as follows.

Garnet-quartz:  $-2.88 \times 10^6/T^2$  (Bottinga & Javoy, 1975)

Quartz-water:  $3.34 \times 10^6/T^2 - 3.31$  (Matsuhisa et al., 1979)

Scheelite-water:  $1.39 \times 10^6/T^2 - 5.87$  (Wesolowski & Ohmoto, 1986; Shieh & Zhang, 1991)

Muscovite-water:  $2.38 \times 10^6/T^2 - 3.89$  (O'Neil & Taylor, 1969), where T is the absolute temperature. Although the  $\delta^{18}\text{O}$  values of vesuvianite were obtained, there was no fractionation factor applicable to vesuvianite.

A number of  $\delta^{18}\text{O}$  values for garnet-scheelite pairs were obtained; however, no consistent temperature was obtained from the garnet-scheelite pair. Reasonable temperatures were obtained only from scheelite-quartz pairs, such as 277.1°C, 290.9°C and 294.6°C (average 288°C).

According to the simplified skarn forming model, multiple reaction fronts migrate away from the fluid source towards the marble to form wollastonite zone, clinopyroxene zone and garnet zone in this order from marble side to a source of fluid supply. This zonation reflects the reactive mobility of  $\text{Si} > \text{Mg}$ ,  $\text{Fe}$  and  $\text{Mn} > \text{Al}$  (Meinert et al., 2005; Shanks, 2014). Development of garnet zone indicates that skarn-forming reaction had advanced sufficiently. Skarn of this study consists of several zones, such as wollastonite, garnet, vesuvianite-garnet and garnet-epidote zones. Among them garnet-bearing zones develop largely, >90% of hole skarn body. Such occurrence of skarn suggests large fluid/rock ratio during skarn forming period.

Pegmatite and aplite veins are frequently observed in the vicinity of study area, furthermore an aplite vein appears at the middle of skarn zone (Fig. 3.2). Aplite and pegmatite are formed through rapid cooling of granitic magma under a

catalysis of volatile component (London, 2005). Above geological information suggests fluid dominant condition during formation of skarn of this study.

Oxygen isotope values of fluid responsible for skarn minerals were calculated at 288°C, on the assumption of fluid dominant condition. Calculated  $\delta^{18}\text{O}$  values are shown in Table 3.3 and plotted in Fig. 3.8. The  $\delta^{18}\text{O}$  values of water in equilibrium with garnet, scheelite, quartz and muscovite were 6.1-9.5‰, 1.2-4.8‰, -1.3-3.6‰ and 4.5‰, respectively. The values for vesuvianite could not be calculated because no fractionation factor was available. Figure 3.8 suggests that garnet precipitated from fluids with different  $\delta^{18}\text{O}$  values from scheelite, quartz and muscovite.

## **6.2. Source of ore-forming fluid**

The origin of skarn-forming fluid has been discussed previously, from which magmatic water (e.g., D'Errico et al., 2012) and metamorphic water (Paterson, 1982) are cogent candidates. In addition, the influence of meteoric water is important for late stage fluids (Öztürk et al., 2008; Shimazaki & Kusakabe, 1993). The  $\delta^{18}\text{O}$  values of magmatic water have been discussed by previous researchers (Sheppard, 1986; Taylor, 1997; Ohmoto, 1986); the typical  $\delta^{18}\text{O}$  range of magmatic water is 5.5 to 10.0‰, and this range is shown in Fig. 3.8. The  $\delta^{18}\text{O}$  values of fluid responsible for garnet are consistent with the range of magmatic water; however, those of scheelite, quartz and muscovite are shifted to lighter values outside the range for magmatic water. Under the geological environment for the skarn deposit of this study, mixing of meteoric water is the most probable mechanism to change heavy  $\delta^{18}\text{O}$  values to lighter values. The  $\delta^{18}\text{O}$  value of modern meteoric water in

the study area is ca. -9.0‰ (Yabusaki, 2016), and this is not directly applicable to a Cretaceous ore-forming environment. However, a light  $\delta^{18}\text{O}$  value is unique for meteoric water; therefore, the participation of meteoric water during the precipitation of scheelite is most probable. Mineral paragenesis (Fig. 3.5) suggests that scheelite is intimately associated with epidote, calcite and quartz, rather than early stage minerals of wollastonite and garnet. This mineral association is consistent with the results obtained from oxygen isotope evidence.

Although oxygen isotope values of the granodiorite of the Idateyama body is unknown, granitoid of the Abukuma terrain have relatively heavier  $\delta^{18}\text{O}$  values, 9-11‰ (Ishihara & Matsuhisa, 2004). When granodiorite of the Idateyam body has similar  $\delta^{18}\text{O}$  value, there is a possibility that meteoric water got involved in the precipitation of garnet.

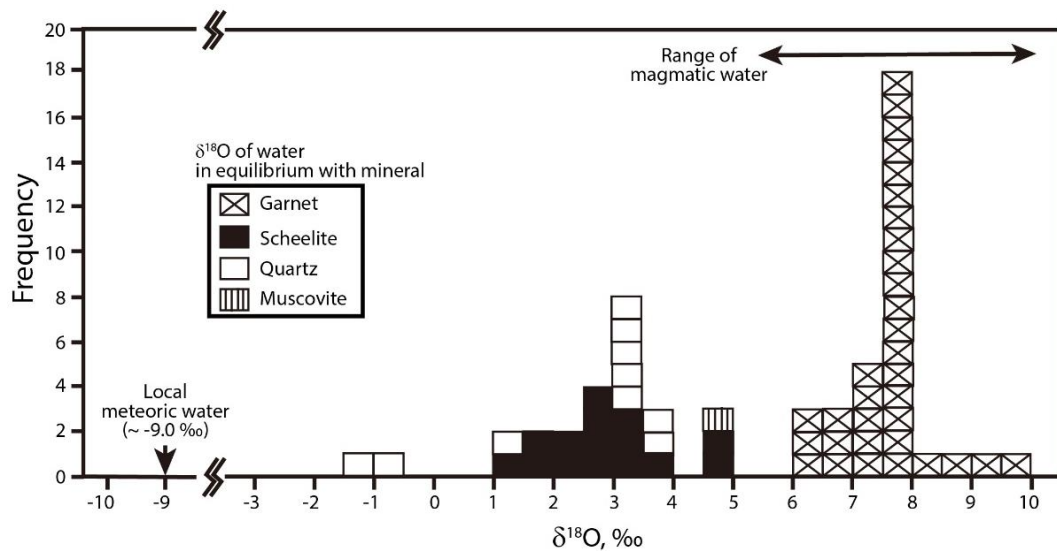


**Fig.3. 8** Oxygen isotope values of water responsible for skarn minerals calculated at 288°C. The range for magmatic water is from Taylor (1997). Value of modern local meteoric water is from Yabusaki (2016).

## **7. Conclusions**

The skarn type tungsten deposit of the Date-Nagai mine is genetically related to the granodiorite batholith of the Idateyama body. Skarn is developed along the contact between pelitic hornfels and marble that remains in small roof pendant body directly above the granodiorite batholith. The granodiorite belongs to the ilmenite series, and accompanies pegmatite and aplite veins; therefore, the emplacement depth of this granodiorite was generally quite deep. Even if under such an environment, the contribution of meteoric water during metasomatic skarn formation was confirmed from oxygen isotope data.



## **Chapter 4: Summary and conclusions**

Oxygen isotope is the powerful tool to study hydrothermal mineral deposits, especially for estimation of origin of mineralized fluids.

In the case of Chandmani Uul IOCG deposit, calculated oxygen isotopic values of ore-forming fluids responsible for minerals suggest that magmatic water participated to precipitate most mushketovite and magnetite ores. A part of mushketovite and epidote precipitated from oxygen isotopically light fluid, which suggests that contribution of meteoric water was the most probable under the geological environment of this deposit.

In the case of Date-Nagai W-skarn deposit, garnet precipitated during relatively early stage of skarn-formation (prograde stage), and magmatic fluid was responsible for garnet. Scheelite precipitated following after garnet from the contribution with meteoric water. Oxygen isotopic equilibrium was not attained between garnet and scheelite.

## **Acknowledgments**

In my thesis, I would like to acknowledge many of the people that I have collaborated with and learned from throughout my PhD. I was very fortunate to have met many outstanding scientists and fellow graduate students and completed my research with the best support from my family and friends.

First and foremost, with regards to my PhD, I would like to acknowledge my supervisors Professor. Emeritus Dr. Ken-ichiro Hayashi, Associate Professor Dr. Teruyuki Maruoka without whom any of my research would have been possible. They have been my constant challenge, critic, and support at the same time, enabling me to grow as a person and a scientist since the day I started the program. I will always remember the days we have spent in the field, memories shared, adventures experienced, ore-forming processes discussed, and classes taught during this time. Hopefully, we will keep sharing these moments and ore-forming process for many years in the future.

I would like to thank Professor Dr. Luvsanchultem Jargal, MSc Sodnom Oyunjgerel, MSc Nansalma Dashpuntsag, and all Prof. assoc. Prof of National University of Mongolia for their continuous support and encouragement throughout my studies.

This work has been supported by KIZUNA Program of the Japan International Cooperation Agency (JICA) during my research.

I have to thank fellow graduate students in resource geology laboratory, Takuya Matsukawa, Yuki Suzuki, Ryuko Asona and Takuma Oishi.

In the case of Chandmani Uul IOCG deposit, I also would like to thank the field work and observation/sampling of the drill cores at the mine site were made

possible by the assistance of the director B. Buyantogtokh, Zasag Chandmani Mines LLC, and senior geologist B. Tsogtmagnai, Bayan Tal project.

In the case of Date-Nagai W-skarn type deposit, some of the samples used in this study are collections in the possession of the Museum of Academic Material, Faculty of Engineering, Yamaguchi University. The authors express heartfelt thanks to Prof. R. Komatsu for his offer of facilities to use the skarn samples.

I owe a great deal to a lot of people. I must acknowledge to Prof. T. Murayama of the Center for Advanced Marine Core Research (CMCR), Kochi University, Drs. Y. Kubota and N. Suzuki of the National Museum of Nature and Science, Tsukuba, provided the mass spectrometer for the oxygen isotope analysis. A portion of this study was performed under the cooperative research program of CMCR (18A023, 18B022), and Dr. Yukiyasu Tsutsumi of the National Museum of Nature and Science, Tsukuba, provided the laser ablation inductively coupled plasma mass spectrometry (LA-ICP-MS) for U-Pb dating of the granitic rocks.

Finally, my thesis would not have come together without constant family support. Balancing life between being a graduate student and a mother was not straightforward at times. I have to thank all of the people who have helped me in the process, but most of all, I would like to thank my father and my mother for taking a good care of my family in the academic year of 2016-2019.

I would like to highlight my husband, Urjin Gansukh, for his constant support, sacrifice, and encouragement throughout these years. I would like to thank him for always being there for me wherever he was, making sure all of the problems were taken care of, and in general, being the biggest supporter of my career. I have to also thank my precious daughter and son, Gansukh Erdenezaya, Gansukh Erkhem-

Erdene for their constant entertainment and unintentional support. I thank all of you so much as you fill my life with joy and happiness, and I hope to enjoy our life together as long as I live.

## References

- Amantov, V. A., Blagonravov, V. A., Borzakovskiy, Yu. A., Durante, M.V., Zonenshain, L. P., Luvsandanzan, B., Matrosov, P. S., Suetenko, I. B., Filippova, I. B. and Hasin, R. A. (1970) Main feature of Palaeozoic stratigraphy of Mongolian People's Republic. In Zaitsev, N. S., Luvsandanzan, B., Marinov, N. A., Menner, V. V., Pavlova, T. G., Peive, A. V., Timofeev, P. P., Tomurtogoo, O. and Yanshin, A. L. (eds.) Stratigraphy and tectonics of the Mongolian People's Republic. Nauka, Moscow, 8–63.
- Armendáriz, M., Rosales, I., Bádenas, B., Piñuela, L., Aurell, M. and García-Ramos, J. C. (2013) An approach to estimate Lower Jurassic seawater oxygen–isotope composition using  $\delta^{18}\text{O}$  and Mg/Ca ratios of belemnite calcites (Early Pliensbachian, northern Spain). *Terra Nova*, 25, 439–445.
- Arévalo, C., Grocott, J., Martin, W., Pringle, M. and Taylor, G. (2006) Structural setting of the Candelaria Fe oxide Cu–Au deposit, Chilean Andes (27°30'S). *Econ. Geol.* 101, 815–841.
- Atherton, M. P. and Aguirre, L. (1992) Thermal and geotectonic setting of Cretaceous volcanic rocks near Ica, Peru, in relation to Andean crustal thinning. *J. South Amer. Earth Sci.*, 5, 47–69.
- Badarch, G., Cunningham, W. D. and Windley, B. F. (2002) A new terrane subdivision for Mongolia: implications for the Phanerozoic crustal growth of Central Asia. *J. Asian Earth Sci.* 21, 87–110.
- Barker, S. L. L., Dipple, G. M., Hickey, K. A., Lepore, W. A. and Vaughan, J. R. (2013) Applying stable isotopes to mineral exploration: Teaching an old dog new tricks. *Econ. Geol.*, 108, 1–9.

- Barton, M. D. (2014) Iron oxide (–Cu–Au–REE–P–Ag–U–Co) systems. In Scott S. D. (ed.) *Geochemistry of mineral deposits, Treatise on geochemistry* Vol. 10, 2nd ed., Elsevier, New York, 515–541.
- Barton, M. D. and Johnson, D. A. (1996) Evaporitic–source model for igneous–related Fe oxide– (REE–Cu–Au–U) mineralization. *Geology*, 24, 259–262.
- Benavides, J., Kyser, T. K., Clark, A. H., Oates, C. J., Zamora, R., Tranovschi, R. and Castillo, B. (2007) The Mantoverde iron oxide–copper–gold district, III Región, Chile: The role of regionally derived, nonmagmatic fluids in chalcopyrite mineralization. *Econ. Geol.*, 102, 415–440.
- Bookstrom, A. A. (1977) The magnetite deposits of El Romeral, Chile. *Econ. Geol.*, 72, 1101–1130.
- Bottinga, Y. and Javoy, M. (1973) Comments on oxygen isotope geothermometry. *Earth Planet. Sci. Lett.*, 20, 250–265.
- Bottinga, Y. and Javoy, M. (1975) Oxygen isotope partitioning among the minerals and triplets in igneous and metamorphic rocks. *Rev. Geophys. Space Phys.*, 13, 401–418.
- Bowman, J. R., Covert, J. J., Clark, A. H. and Mathieson, G. A. (1985a) The Can Tung E-zone sheelite skarn orebody, Tungsten, Northwest Territories: Oxygen, hydrogen, and carbon isotope studies. *Econ. Geol.*, 80, 1872–1895.
- Bowman, J. R., O’Neil, J. R. and Essene, E. J. (1985b) Contact skarn formation at Elkhorn, Montana II: Origin and evolution of C–O–H skarn fluids. *Amer. J. Sci.*, 285, 621–660.
- Brown, P. E. and Essene, E. J. (1985) Activity variations attending tungsten skarn formation, Pine Creek, California. *Contrib. Mineral. Petrol.*, 89, 358–369.

- Bumburuu, G., Lkhundev, Sh. and Burentugs, J. (1990) Results of 1:200,000 scale geological mapping and general prospecting in Dundgobi and Dornogobi. Geologic Information Center, Ulaanbaatar, Open-File Report 4377, 700p. (in Russian).
- Byamba, J., Lkhundev, Sh. and Tundev, S. (1990) New data on age of Upper Proterozoic deposits in Middle Gobi. *Doklady Akademii Nauk SSSR* 312, 428–431 (in Russian).
- Cembrano, J., González, G., Arancibia, G., Ahumada, I., Olivares, V. and Herrera, V. (2005) Fault zone development and strain partitioning in an extensional strike-slip duplex: A case study from the Mesozoic Atacama fault system, Northern Chile. *Tectonophysics*, 400, 105–125.
- Chacko, T., Cole, D. R. and Horita, J. (2001) Equilibrium oxygen, hydrogen and carbon isotope fractionation factors applicable to geological systems. *Rev. Miner. Geochem.*, 43, 1–81.
- Chappell, B. W. (1999) Aluminum saturation in I- and S-type granites and the characterization of fractionated haplogranites. *Lithos*, 46, 535–551.
- Charlie, D. and Rohan, W. (2006) Progress report of Chandmani Uul license block Mongolia. Unpublished Internal Report. IMMI, Ulaanbaatar, Report MR–2006–13, 33p.
- Chen, H. (2013) External sulphur in IOCG mineralization: Implications on definition and classification of the IOCG clan. *Ore Geol. Rev.*, 51, 74–78.
- Chen, H., Clark, A. H., Kyser, T. K., Ullrich, T. D., Baxter, R., Chen, Y. and Moody, T. C. (2010) Evolution of the giant Marcona–Mina Justa iron oxide–copper–gold district, south–central Peru. *Econ. Geol.*, 105, 155–185.

- Chen, H., Kyser, T. K. and Clark, A. H. (2011) Contrasting fluids and reservoirs in the continuous Marcona and Mina Justa iron oxide–Cu (–Ag–Au) deposits, south–central Perú. *Miner. Deposita*, 46, 677–706.
- Chiaradia, M., Banks, D., Cliff, R., Marschik, R. and Haller, A. (2006) Origin of fluids in iron oxide–copper–gold deposits: Constrains from  $\delta^{37}\text{Cl}$ ,  $^{87}\text{Sr}/^{86}\text{Sr}$ , and Cl/Br. *Miner. Deposita*, 41, 565–573.
- Collins, B. I. (1977) Formation of sheelite-bearing and sheelite-barren skarns at Lost Creek, Pioneer Mountains, Montana. *Econ. Geol.*, 72, 1505–1523.
- Dare, S. A. S., Barnes, S. J., Beaudoin, G., Méric, J., Boutroy, E. and Potvin–Doucet, C. (2014) Trace elements in magnetite as petrogenetic indicators. *Miner. Deposita*, 49, 785–796.
- Deer, W. A., Howie, R. A. and Zussman, J. (1992) *The rock-forming minerals*, 2nd ed., Pearson Education, London, 695p.
- Dejidmaa, G., Bujinlkham, B., Eviihuu, A., Enkhtuya, B., Ganbaatar, T., Munkh–Erdene, N. and Oyuntuya, N. (1996) Distribution map of deposits and occurrences in Mongolia (scale 1:1,000,000). Geologic Information Center, Mineral Resources Authority of Mongolia, Ministry of Industry and Trade of Mongolia, Ulaanbaatar, Open–File Report, 280 p.
- D’Errico, M. E., Lackey, J. S., Surpless, B. E., Loewy, S. L., Wooden, J. L., Barnes, J. D., Strickland, A. and Valley, J. W. (2012) A detailed record of shallow hydrothermal fluid flow in the Sierra Nevada magmatic arc from low- $\delta^{18}\text{O}$  skarn garnet. *Geology*, 40, 763–766.
- de Melo, G. H. C., Monteiro, L. V. S., Xavier, R. P., Moreto, C. P. N., Santiago, E. S. B., Dufrane, S. A., Aires, B. and Santos, A. F. F. (2017) Temporal evolution



- of the giant Salobo IOCG deposit, Carajás Province (Brazil): constraints from Paragenesis of hydrothermal alteration and U–Pb geochronology. *Miner. Deposita*, 52, 709–732.
- de Melo, G. H. C., Monteiro, L. V. S., Xavier, R. P., Moreto, C. P. N. and Santiago, E. (2019) Tracing fluid sources for the Salobo and Igarapé Bahia deposits: Implications for the genesis of the iron oxide–copper–gold deposits in the Carajás Province, Brazil. *Econ. Geol.*, 114, 697–718.
- Dupuis, C. and Beaudoin, G. (2011) Discriminant diagram for iron oxide trace element fingerprinting of mineral deposit types. *Miner. Deposita*, 46, 319–335.
- Dutton, A., Wilkinson, B. H., Welker, J. M., Bowen, G. J. and Lohmann, K. C. (2005) Spatial distribution and seasonal variation in  $^{18}\text{O}/^{16}\text{O}$  of modern precipitation and river water across the conterminous USA. *Hydrol. Process.*, 19, 4121–4146.
- Einaudi, M. T., Meinert, L. D and Newberry, R. J. (1981) Skarn deposits. In Skinner, B. J. (ed.) *Economic Geology 75th Anniversary Volume*. Economic Geology Publishing Company, El Paso, 317–391.
- González, E., Kojima, S., Ichii, Y., Tanaka, T., Fujimoto, Y. and Ogata, T. (2018) Silician magnetite from the Copiapó Nordeste Prospect of Northern Chile and its implication for ore–forming conditions of iron oxide–copper–gold deposits. *Minerals*, 8, 529.
- Groves, D. I., Bierlein, F. P., Meinert, L. D. and Hizman, M. W. (2010) Iron oxide copper–gold (IOCG) deposits through earth history: Implications for metallogenesis and sulfur saturation in primary magmas. *Econ. Geol.*, 105, 641–654.

- Hayashi, K., Maruyama, T., and Satoh, H. (2001) Precipitation of gold in a low-sulfidation epithermal gold deposits: insights from a submillimeter-scale oxygen isotope analysis of vein quartz. *Econ. Geol.*, 96, 211–216.
- Heidarian, H., Lentz, D., Alirezaei, S. and Peighambari, S. (2016) Using the chemical analysis of magnetite to constrain various stages in the formation and genesis of the Kiruna-type Chadormalu magnetite-apatite deposit, Bafq district, Central Iran. *Mineral. Petrol.*, 110, 927–942.
- Hitzman, M. W. (2000) Iron oxide–Cu–Au deposits: What, where, when, and why. In Porter, T. M. (ed.) *Hydrothermal iron oxide copper gold and related deposits: A global perspective*. Australian Mineral Foundation, Adelaide, 9–25.
- Hitzman, M. W., Oreskes, N. and Einaudi, M. T. (1992) Geological characteristics and tectonic setting of Proterozoic iron oxide (Cu–U–Au–REE) deposits. *Precamb. Res.*, 58, 241–287.
- Huang, X. –W., Sappin, A. –A., Boutory, É., Beaudoin, G., and Makvandi, S. (2019) Trace element composition of igneous and hydrothermal magnetite from porphyry deposits: Relationship to deposit subtype and magmatic affinity. *Econ. Geol.*, 114, 917–952.
- Irvine, T. N. and Barragar, R. A. (1971) A guide to the chemical classification of common volcanic rocks. *Can. J. Earth Sci.*, 8, 523–548.
- Ishihara, S. and Matsuhisa, Y. (2004) Oxygen isotopic constraints on the geneses of the Cretaceous granitoids in the Kitakami and Abukuma terrains, Northeast Japan. *Bull. Geol. Survey Japan*, 55, 57–66.
- Jaffrés, J. B. D., Shields, G. A. and Wallmann, K. (2007) The oxygen isotope evolution of seawater: A critical review of a long-standing controversy and an

improved geological water cycle model for the past 3.4 billion years. *Earth Sci. Rev.*, 83, 83–122.

Khasgerel, B. (2010) *Geology, Whole-rock geochemistry, Mineralogy and Stable Isotopes (O, H and S) of Sericitic and Advanced Argillic Alteration Zones, Oyu Tolgoi Porphyry Cu-Au Deposits, Mongolia*. Doctoral thesis. University of Tsukuba.

Knauth, L. P. and Lowe, D. R. (1978) Oxygen isotope geochemistry of cherts from the Onverwacht Group (3.4 billion years), Transvaal, South Africa, with implications for secular variations in the isotopic composition of cherts. *Earth Planet. Sci. Lett.*, 41, 209–222.

Knauth, L. P. and Roberts, S. K. (1991) The hydrogen and oxygen isotope history of the Silurian–Permian hydrosphere as determined by direct measurement of fossil water. In Taylor H. P. et al. (eds.) *Stable isotope geochemistry: A tribute to Samuel Epstein*. Geochemical Society, Spec. Publ., 3, 91–104.

Knipping, J. L., Bilenker, L. D., Simon, A. C., Reich, M., Barra, F., Deditius, A., Wälle, M., Heinrich, C., Holtz, F. and Munizaga, R. (2015) Trace elements in magnetite from massive iron oxide–apatite deposits indicate a combined formation by igneous and magmatic–hydrothermal processes. *Geochim. Cosmochim. Acta*, 171, 15–38.

Knipping, J. L., Fiege, A., Simon, A. C., Oeser, M., Reich, M. and Bilenker, L. D. (2019) In-situ iron isotope analyses reveal igneous and magmatic–hydrothermal growth of magnetite at the Los Colorados Kiruna-type iron oxide–apatite deposit, Chile. *Amer. Miner.*, 104, 471–484.

- Kubo, K., Yamamoto, T., Murata, Y. and Makino, M. (2014) Geology of the Kawamata district. Quadrangle Series, 1:50,000, Geological Survey of Japan, Tsukuba, 86p. (in Japanese with English abstract).
- La Cruz, N. L., Simon, A. C., Wolf, A. S., Barra, F. and Gagnon, J. E. (2019) The geochemistry of apatite from the Los Colorados iron oxide–apatite deposit, Chile: implications for ore genesis. *Miner. Deposita*, 54, 1143–1156.
- Li, Z. –Z., Qin, K. –Z., Li, G. –M., Jin, L. –Y., Song, G. –X. and Han, R. (2019) Inclusion of meteoric water triggers molybdenite precipitation in porphyry Mo deposits: A case study of the Chalukou giant Mo deposit. *Ore Geol. Rev.*, 109, 144–162.
- London, D. (2005) Granitic pegmatites: an assessment of current concepts and directions for the future. *Lithos*, 80, 281–303.
- Maniar, P. D. and Piccoli, P. M. (1989) Tectonic discrimination of granitoids. *Geol. Soc. Amer. Bull.*, 101, 635–643.
- Marangoanha, B., de Oliveira, D. C., de Oliveira, V. E. S., Galarza, M. A. and Lamarão (2019) Neoproterozoic A-type granitoids from Carajás province (Brazil): New insights from geochemistry, geochronology and microstructural analysis. *Precamb. Res.*, 324, 86–108.
- Marschik, R. and Fontboté, L. (2001) The Candelaria–Punta del Cobre iron oxide Cu–Au (–Zn–Ag) deposits, Chile. *Econ. Geol.*, 96, 1799–1826.
- Marschik, R., Fontignie, D., Chiaradia, M. and Voldet, P. (2003) Geochemical and Sr–Nd–O isotope composition of granitoids of the Early Cretaceous Copiapó plutonic complex (27°30'S), Chile. *J. South Amer. Earth Sci.*, 16, 381–398.

- Mathieson, G. A. and Clark, A. H. (1984) The Can Tung E-zone sheelite skarn orebody, Tungsten, Northwest Territories: A revised genetic model. *Econ. Geol.*, 79, 883-901.
- Matsuhisa, Y., Goldsmith, J. R. and Clayton, R. N. (1979) Oxygen isotope fractionation in the system quartz–albite–anorthite–water. *Geochim. Cosmochim. Acta*, 43, 1131–1140.
- Matthews, A., Goldsmith, J. R. and Clayton, R. N. (1983) Oxygen isotope fractionations involving pyroxenes: the calibration of mineral-pair geothermometers. *Geochim. Cosmochim. Acta*, 47, 631-644.
- Matthews, A. and Schliestedt, M. (1984) Evolution of blueschist and greenschist rocks of Sifnos, Cyclades, Greece. *Contrib. Mineral. Petrol.*, 88, 150–163.
- McDonough, W.F. and Sun, S.S. (1995) The composition of the Earth. *Chem. Geol.*, 120, 223–253.
- Meinert, L.D., Dipple, G.M and Nicolescu, S. (2005) World Skarn Deposits. In Hedenquist, J. W., Thompson, J. F. H., Goldfarb, R. J. and Richards, J. P. (eds.) *Economic Geology 100th Anniversary Volume*. Society of Economic Geologists Inc., Littleton, 299-336.
- Ménard, J. J. (1995) Relationship between altered pyroxene diorite and the magnetite mineralization in the Chilean iron belt, with emphasis on the El Algarrobo iron deposits (Atacama region, Chile). *Miner. Deposita*, 30, 268–274.
- Middlemost, E. A. K. (1994) Naming materials in the magma/igneous rock system. *Earth Sci. Rev.*, 37, 215–224.

- Ministry of Economy, Trade and Industry (METI) (1987) Report on rare metal resources: Eastern Abukuma area. 168 p. (In Japanese).
- Monecke, J., Reynolds, T. J., Tsuruoka, S., Bennett, M. M. and Skews, W. B. (2018) Quartz solubility in the H<sub>2</sub>O–NaCl systems: A framework for understanding vein formation in porphyry copper deposits. *Econ. Geol.*, 113, 1007–1046.
- Monteiro, L. V. S., Xavier, R. P., de Carvalho, E. R., Hitzman, M. W., Johnson, C. A., de Souza, C. R. and Torresi, I. (2008) Spatial and temporal zoning of hydrothermal alteration and mineralization in the Sossego iron oxide–copper–gold deposit, Carajás Mineral Province, Brazil: Paragenesis and stable isotope constraints. *Miner. Deposita*, 43, 129–159.
- Nadoll, P., Angerer, T., Mauk, J. L., French, D., and Walshe, J. (2014) The chemistry of hydrothermal magnetite: A review. *Ore Geol. Rev.*, 61, 1–32.
- Nesbitt, H. W. and Young, G. M. (1982) Early Proterozoic climates and plate motions inferred from major element chemistry of lutites. *Nature*, 299, 715–717.
- Newberry, R. J. and Swanson, S. E. (1986) Sheelite skarn granitoids: an evaluation of the role of magmatic source and process. *Ore Geol. Rev.*, 1, 57–81.
- Nokleberg, W. J. (1981) Geologic setting, petrology, and geochemistry of zoned tungsten-bearing skarns at the Strawberry mine, central Sierra Nevada, California. *Econ. Geol.*, 26, 111–133.
- Ohmoto, H. (1986) Stable isotope geochemistry of ore deposits. In Valley, J. W., Taylor, H. P. Jr. and O’Neil, J. R. (eds.) *Stable isotopes in high temperature geological processes*. *Rev. Mineral.*, 16, 491–559.

- O'Neil, J. R. and Taylor, H. P. Jr. (1969) Oxygen isotope equilibrium between muscovite and water. *Amer. Miner.*, 52, 1414-1437.
- Oyunjargal, L., Matsukura, K. and Hayashi, K. (2019) Oxygen isotopic study on the Date-Nagai skarn-type tungsten deposit, northeastern Japan. *Resour. Geol.*, 69, 448–459.
- Oyarzún, R., Oyarzún, J., Ménard, J. J. and Lillo, J. (2003) The Cretaceous iron belt of northern Chile: Role of oceanic plates, a superplume event, and a major shear zone. *Miner. Deposita*, 38, 640–646.
- Oyarzún, R., Rodriguez, M., Pincheria, M., Doblas, M. and Helle, S. (1999) The Candelaria (Cu–Fe–Au) and Punta de Cobre (Cu–Fe) deposits (Copiapó, Chile): a case for extension-related granitoid emplacement and mineralization processes?. *Miner. Deposita*, 34, 799–801.
- Öztürk, Y. Y., Helvacı, C. and Satır, M. (2008) The influence of meteoric water on skarn formation and late-stage hydrothermal alteration at the Evciler skarn occurrences, Kazdag, NW Turkey. *Ore Geol. Rev.*, 34, 271–284.
- Paterson, C. J. (1982) Oxygen isotopic evidence for the origin and evolution of a scheelite ore-forming fluid, Glenorchy, New Zealand. *Econ. Geol.*, 77, 1672-1678.
- Pearce, J. A., Harris, N. B. W. and Tindle, A. G. (1984) Trace element discrimination diagrams for the tectonic interpretation of granitic rocks. *J. Petrol.*, 25, 956–983.
- Pollard, P. J. (2006) An intrusion-related origin for Cu–Au mineralization in iron oxide–copper–gold (IOCG) provinces. *Miner. Deposita*, 41, 179–187.

- Rieger, A. A., Marschik, R., Díz, M., Hölzl, S., Chiradia, M., Akker, B. and Spangenberg, J. E. (2010) The hypogene iron oxide–copper–gold mineralization in the Mantoverde district, Northern Chile. *Econ. Geol.*, 105, 1271–1290.
- Rieger, A. A., Marschik, R. and Díaz, M. (2012) The evolution of the hydrothermal IOCG system in the Mantoverde district, northern Chile: New evidence from microthermometry and stable isotope geochemistry. *Miner. Deposita*, 47, 359–369.
- Robb, L. (2005) *Introduction to ore-forming processes*. Blackwell, Malden, 373p.
- Rojas–Agramonte, Y., Kroner, A., Demoux, A., Xia, X., Wang, W., Donskaya, T., Liu, D. and Sun, M. (2011) Detrital and xenocrystic zircon ages from Neoproterozoic to Palaeozoic arc terranes of Mongolia: significance for the origin of crustal fragments in the Central Asian Orogenic Belt. *Gondwana Res.*, 19, 751–763.
- Rojas, P., Barra, F., Deditius, A., Reich, M., Simon, A. C., Roberts, M. P. and Rojo, M. (2018) New contributions to the understanding of iron oxide–apatite deposits revealed by magnetite ore geochemistry at El Romeral deposit, Chile. *Ore Geol. Rev.*, 93, 413–435.
- Safanova, I. Y. and Santosh, M. (2014) Accretionary complexes in the Asia–Pacific region: tracing archives of ocean plate stratigraphy and tracking mantle plume. *Gondwana Res.*, 25, 126–158.
- Scheuber, E. and Andriessen, P. A. M. (1990) The kinematic and geodynamic significance of the Atacama fault zone, northern Chile. *J. Structural Geol.*, 12, 243–257.



- Scheuber, E., Hammerschmidt, K., and Friedrichsen, H. (1995)  $^{40}\text{Ar}/^{39}\text{Ar}$  and Rb–Sr analyses from ductile shear zones from the Atacama fault zone, northern Chile: The age of deformation. *Tectonophysics*, 250, 61–87.
- Shanks, W. C. III (2014) Stable isotope geochemistry of mineral deposits. In Scott S. D. (ed.) *Geochemistry of mineral deposits, Treatise on geochemistry Vol. 10*, 2nd ed., 59-85, Elsevier, New York.
- Shemesh, A., Kolodny, Y. and Luz, B. (1983) Oxygen isotope variations in phosphate of biogenic apatites. II. Phosphorite rocks. *Earth Planet. Sci. Lett.*, 64, 405–416.
- Sheppard, S. M. F. (1986) Characterization and isotopic variations in natural water. In Valley, J. W., Taylor, H. P. Jr. and O’Neil, J. R. (eds.) *Stable isotopes in high temperature geological processes. Rev. Mineral.*, 16, 165-183.
- Shieh, Y. and Zhang, G. (1991) Stable Isotope studies of quartz-vein type tungsten deposits in Dajishan Mine, Jiangxi Province, Southeast China. In H. P. Taylor, Jr., J. R. O’Neil and I. R. Kaplan (eds.) *Stable Isotope Geochemistry: A Tribute to Samuel Epstein. The Geochemical Society, Special Publication No.3*, 425-436.
- Shimazaki, H. and Kusakabe, M. (1993) Oxygen isotope study of the Tsumo Cu–Zn–Fe–W skarn deposits, Japan. *Resour. Geol.*, 43, 245-254.
- Shu, Q. and Lai, Y. (2017) Fluid inclusion and oxygen isotope constraints on the origin and hydrothermal evolution of the Haisugou porphyry Mo deposit in the northern Xilamulu district, NE China. *Geofluids*, 2017, ID4094582.
- Sillitoe, R. H. (2003) Iron oxide–copper–gold deposits: An Andean view. *Miner. Deposita*, 38, 787–812.

- Simon, A. C., Knipping, J., Reich, M., Barra, F., Dediitus, A. P., Bilenker, L. and Childress, T. (2018) Kiruna-type iron oxide-apatite (IOA) and iron oxide-copper-gold (IOCG) deposits form by a combination of igneous and magmatic-hydrothermal processes: evidence from the Chilean iron belt. In Arribas, A. M. and Maul, J. L. (eds.) *Metals, Minerals, and Society*. SEG Spec. Publ. 21, Society of Economic Geologists Inc., Littleton, 89–114.
- Sturm, M. B., Ganbaatar, O., Voigt, C. C. and Kaczensky, P. (2017) First field-based observations of  $\delta^2\text{H}$  and  $\delta^{18}\text{O}$  values of event-based precipitation, rivers and other water bodies in the Dzungarian Gobi, SW Mongolia. *Isotopes Environ. Health Studies*, 53, 157–171.
- Sun, S. S. and McDonough, W. F. (1989) Chemical and isotopic systematics of ocean basalts: Implications for mantle composition and processes. In Saunders, A. D. and Norry, M. J. (eds.) *Magmatism in the ocean basins*, Geological Society, London, Special Publ. 42, 313–345.
- Suzuki, Y. and Hayashi, K. (2019) Mineralogy, fluid inclusions, and sulfur isotopes of the Huanzala deposits, Peru: Early skarn and late polymetallic replacement style mineralizations. *Resour. Geol.*, 69, 249–269.
- Taylor, H. P. (1974) The application of oxygen and hydrogen isotope studies to problems of hydrothermal alteration and ore deposition. *Econ. Geol.*, 69, 843–883.
- Taylor, H.P. (1997) Oxygen and hydrogen isotope relationships in hydrothermal mineral deposits. In Barnes, H.L. (ed.) *Geochemistry of hydrothermal ore deposits*, 3rd ed., John Wiley & Sons, New York, 229–302.

- Taylor, B. E. and O'Neil, J. R. (1977) Stable isotope studies of metasomatic Ca-Fe-Al-Si skarns and associated metamorphic and igneous rocks, Osgood Mountain, Nevada. *Contrib. Mineral. Petrol.*, 63, 1-49.
- Thomas, C., Cole, D. R. and Horita, J. (2001) Equilibrium oxygen, hydrogen and carbon isotope fractionation factors applicable to geologic systems. *Rev. Mineral. Geochem.*, 43, 1-81.
- Tornos, F., Velasco, F. and Hanchar, J. M. (2016) Iron-rich melts, magmatic magnetite, and superheated hydrothermal systems: the El Laco deposit, Chile. *Geology*, 44, 427–430.
- Torresi, I., Xavier, R. P., Bortholoto, D. F. A. and Monteiro, L. V. S. (2012) Hydrothermal alteration, fluid inclusions and stable isotope systematics of the Alvo 118 iron oxide–copper–gold deposit, Carajás Mineral Province (Brazil): Implications for ore genesis. *Miner. Deposita*. 47, 299–323.
- Troll, V. R., Weis, F. A., Jonsson, E., Andersson, U. B., Afshin Majidi, S., Högdahl, K., Harris, C., Millet, M. –A., Saravanan Chinnasamy, S., Kooijman, E. and Nilsson, K. P. (2019) Global Fe–O isotope correlation reveals magmatic origin of Kiruna-type apatite–iron–oxide ores. *Nature Commun.* Tornos, doi.org/10.1038/s41467-019-09244-4.
- Ukhnaa, G. and Baasan, B. (2016) Iron deposits in Mongolia. GCOM, Ulaanbaatar, 283 p. (in Mongolian).
- Wesolowski, D. and Ohmoto, H. (1986) Calculated oxygen isotope fractionation factors between water and the minerals sheelite and powellite *Econ. Geol.*, 81, 471-477.

- Wilhem, C., Windley, B. F. and Stampfli, G. M. (2012) The Altaids of Central Asia: a tectonic and evolutionary innovative review. *Earth Sci. Rev.*, 113, 303–341.
- Williams, P. J., Barton, M. D., Jhonson, D. A., Fontboté, L., de Haller, A., Mark, G., Oliver, N. H. S. and Marschik, R. (2005) Iron oxide–copper–gold deposits: Geology, space–time distribution, and possible models of origin. In Hedenquist, J. W., Thompson, J. F. H., Goldfarb, R. J. and Richards, J. P. (eds.) *Economic Geology 100th Anniversary Volume*. Society of Economic Geologists Inc., Littleton, 371–405.
- Windley, B. F., Alexeive, D., Xiao, W., Kroner, A. and Badarch, G. (2007) Tectonic models for accretion of the Central Asian Orogenic Belt. *J. Geol. Soc. London*, 163, 31–34.
- Yabusaki, S. (2016) Distribution of stable isotopes of oxygen and hydrogen in spring water and groundwater at Fukushima Prefecture. *J. Center Regional Affairs Fukushima Univ.*, 27, 31-41. (in Japanese)
- Yamamoto, T. (1996) Stratigraphy and eruption style of Miocene volcanic rocks in the Ryozen district, NE Japan. *J. Geol. Soc. Japan*, 102, 730-750. (in Japanese with English abstract)
- Yamamoto, T. and Hoang, N. (2009) Synchronous Japan Sea opening Miocene fore-arc volcanism in the Abukuma Mountains, NE Japan: an advancing hot asthenosphere flow versus Pacific slab melting. *Lithos*

## Appendix I: Analytical data

**Table 2.1** Major element (in wt.% oxide) concentrations of the granitoids at the Chandmani Uul deposit.

Sample No.	CHU167	CHU179	CHU180	CHU203	CHU228	CHU 242	BT001	BT002	BT004	BT005	BT008	BT011	BT012	BT015	BT021
SiO <sub>2</sub>	61.78	61.95	63.44	64.99	71.1	65.69	63.85	61.69	62.99	61.85	61.75	58.36	61.83	62.59	61.48
Al <sub>2</sub> O <sub>3</sub>	16.64	16.41	15.98	13.91	14.3	16.33	15.66	15.45	15.27	15.96	15.69	15.11	16.49	15.65	15.42
Fe <sub>2</sub> O <sub>3</sub> (T)	2.38	5.08	4.77	2.31	2.16	4.83	5.03	4.66	4.69	4.2	4.7	6.03	4.11	5.22	4.37
MnO	0.109	0.094	0.1	0.121	0.04	0.097	0.044	0.079	0.07	0.082	0.056	0.124	0.104	0.097	0.118
MgO	3.65	1.83	1.55	0.99	0.39	1.62	0.73	1.36	1.37	1.58	2	1.71	1.39	1.68	1.5
CaO	4.23	3.07	3.04	5.12	1.47	1.76	2.21	3.07	2.77	3.92	2.88	4.83	2.83	4.34	3.05
Na <sub>2</sub> O	4.94	4	3.42	2.26	2.91	4.41	3.53	3.27	4.68	4.95	3.2	3.62	4.36	3.56	5.28
K <sub>2</sub> O	3.43	3.4	4.47	3.75	4.7	2.53	4.18	3.39	2.9	2.48	3.97	2.91	3.24	4.03	1.96
TiO <sub>2</sub>	0.3	0.479	0.43	0.362	0.251	0.494	0.489	0.446	0.389	0.435	0.473	0.427	0.412	0.456	0.435
P <sub>2</sub> O <sub>5</sub>	0.26	0.19	0.18	0.11	0.05	0.18	0.21	0.18	0.17	0.17	0.19	0.18	0.16	0.16	0.18
LOI	2.52	2.7	2.83	5.94	2.54	2.4	3.87	5.97	4.54	4.63	5.64	6.9	5.07	1.64	4.77
Total	100.24	99.20	100.21	99.86	99.91	100.34	99.80	99.57	99.84	100.26	100.55	100.20	100	99.42	98.56
Na <sub>2</sub> O+K <sub>2</sub> O	8.37	7.40	7.89	6.01	7.61	6.94	7.71	6.66	7.58	7.43	7.17	6.53	7.60	7.59	7.24
K <sub>2</sub> O/ Na <sub>2</sub> O	0.69	0.85	1.31	1.66	1.62	0.57	1.18	1.04	0.62	0.50	1.24	0.80	0.74	1.13	0.37
A/NK	1.41	1.60	1.53	1.79	1.45	1.63	1.52	1.71	1.41	1.47	1.64	1.66	1.54	1.53	1.43
A/CNK	0.85	1.04	1.00	0.81	1.14	1.24	1.09	1.06	0.96	0.89	1.06	0.84	1.04	0.86	0.94
CIA	46.0	50.9	50.0	44.9	53.3	55.3	52.2	51.4	49.0	47.1	51.5	45.8	51.0	46.4	48.5
δ <sup>18</sup> O(‰)	6.6	4.8	3.9	7.5	5.8	5.7	NA	NA	NA	NA	NA	NA	NA	NA	4.6

Notes: LOI- loss on ignition; NA: Not analyzed.

**Table 2.2.** Trace element (in ppm) compositions of the granitoids at the Chandmani Uul deposit.

Sample No.	CHU167	CHU179	CHU180	CHU203	CHU228	CHU 242	BT001	BT002	BT004	BT005	BT008	BT011	BT012	BT015	BT021
La	13	21	19.4	23.1	20.5	17	24.3	22.8	18	21.5	21.7	20	17.8	19.9	18.8
Ce	27.9	43.3	40.9	45.2	38.4	44.1	50.1	44.8	36.2	42.7	45	39.1	35.5	41.3	36.5
Pr	3.6	5.13	4.73	4.91	3.92	3.99	5.77	4.97	4.17	4.94	5.17	4.58	4.16	4.8	4.04
Nd	15.2	20	17.8	17.5	14.3	15.7	22.2	19.2	16.3	19	20.1	17.6	16.2	18.5	15.1
Sm	3.19	4.09	3.92	3.52	2.81	3.38	4.65	3.7	3.56	4.1	4.06	3.8	3.08	3.81	2.95
Eu	0.65	1.06	1.03	0.794	0.486	0.832	0.994	0.96	0.865	0.9	1.04	1.07	0.823	1	0.846
Gd	2.23	3.3	3.22	2.8	2.29	2.74	3.49	3.01	2.9	3.3	3.43	3.1	2.64	3.09	2.61
Tb	0.29	0.48	0.47	0.44	0.36	0.42	0.53	0.46	0.45	0.5	0.51	0.5	0.42	0.47	0.4
Dy	1.4	2.7	2.74	2.62	2.18	2.54	3.07	2.76	2.58	2.9	3.03	2.9	2.45	2.8	2.29
Ho	0.26	0.52	0.55	0.54	0.45	0.5	0.6	0.55	0.51	0.6	0.61	0.6	0.49	0.54	0.47
Er	0.75	1.49	1.69	1.75	1.4	1.52	1.74	1.72	1.61	1.8	1.79	1.8	1.52	1.6	1.45
Tm	0.107	0.228	0.247	0.253	0.211	0.241	0.273	0.268	0.259	0.29	0.298	0.28	0.248	0.243	0.233
Yb	0.76	1.57	1.82	1.77	1.45	1.71	1.9	1.75	1.74	2	2.07	1.9	1.78	1.78	1.71
Lu	0.128	0.25	0.298	0.295	0.226	0.277	0.306	0.283	0.29	0.34	0.345	0.31	0.272	0.289	0.279
Y	7.8	14.7	16.4	16.8	14.3	13.9	17.5	17.6	16.2	18	18.9	18	15.7	16.2	14.5
ΣREE	69.47	105.12	98.82	105.49	88.98	94.95	119.92	107.23	89.43	104.87	109.15	97.54	87.38	100.12	87.68
LREE/HREE	9.57	8.06	7.19	8.37	8.83	7.81	8.29	8.12	6.98	7.30	7.32	6.83	7.21	7.48	7.52
LaN/ YbN	1.69	2.07	2.15	2.60	2.82	2.13	2.16	2.34	2.18	2.23	2.13	2.24	2.17	2.12	2.45
Nb/La	0.71	0.85	0.86	0.75	0.57	0.81	0.72	0.85	0.80	0.72	0.83	0.92	0.86	0.86	0.91
(La/ Sm)N	0.98	0.99	1.02	0.99	0.98	1.27	1.00	0.99	0.99	0.98	1.01	0.96	0.98	1.00	0.98

δEu	0.71	0.85	0.86	0.75	0.57	0.81	0.72	0.85	0.80	0.72	0.83	0.92	0.86	0.86	0.91
δCe	0.97	0.98	1.01	0.98	0.97	1.26	0.99	0.98	0.98	0.97	1.00	0.95	0.97	0.99	0.97
Rb	81	107	111	151	187	86	114	112	91	66	114	83	92	87	68
Ba	1101	451	691	821	504	487	530	376	435	458	575	638	499	588	301
Th	2.59	6.5	8.54	9.33	16	8.5	10.7	8.22	9.24	8.8	10.1	7.3	8.53	8.97	8.55
U	1.03	1.88	3.1	5.03	3.06	1.91	2.41	1.43	2.47	2.7	2.34	1.8	1.9	3.21	1.67
Nb	1.4	5.5	5.3	5	6.1	7	6.7	5	4.6	6	5.1	7	6	6.3	5.4
Ta	0.09	0.39	0.35	0.38	0.62	0.46	0.45	0.31	0.28	0.4	0.34	0.4	0.44	0.48	0.41
Pb	18	22	25	13	9	20	11	11	19	15	7	23	24	10	7
Sr	252	396	507	173	305	563	255	354	382	488	263	459	283	526	274
Zr	62	147	147	146	145	150	153	139	148	141	147	118	126	141	138
Hf	1.6	3.6	3.5	3.5	3.7	3.6	3.8	3.2	3.5	3.8	3.5	2.9	3.2	3.3	3.4
Ga	17	18	17	15	16	17	17	17	16	17	18	17	18	18	16
V	166	114	100	50	26	98	100	101	88	88	108	104	95	108	82
Cr	160	80	210	60	80	70	120	70	140	190	100	90	< 20	230	90
Co	7	8	9	2	3	7	7	6	5	8	8	17	6	13	9
Ni	70	40	90	30	30	30	50	30	60	60	50	30	< 20	100	40

Notes: LaN/YbN and (La/Sm)N values are La/Yb ratios normalized to chondrite values after McDonough and Sun, 1995,  
Eu/Eu\*=2\*EuN/[SmN+GdN]; Ce/Ce=2\*CeN/[LaN+PrN].

**Table 2.3.** LA-ICP-MS analyzed data of age-known samples and calculated ages.

Labels	$^{206}\text{Pb}_c^{(1)}$ (%)	U (ppm)	Th (ppm)	Th/U	$^{238}\text{U}/^{206}\text{Pb}^*^{(1)}$		$^{207}\text{Pb}^*/^{206}\text{Pb}^*^{(1)}$			$^{238}\text{U}/^{206}\text{Pb}^* \text{ age}^{(1)}$ (Ma)			$^{238}\text{U}/^{206}\text{Pb}^* \text{ age}^{(2)}$ (Ma)		
CHU179-01	0.19	80	33	0.42	13.11	± 0.22	0.0581	± 0.0047		473.9	± 7.8		473.1	± 7.8	
CHU179-02	0.18	131	88	0.69	12.91	± 0.19	0.0558	± 0.0039		480.9	± 6.8		481.4	± 6.7	
CHU179-03	0.00	356	316	0.91	13.39	± 0.14	0.0584	± 0.0014		464.3	± 4.7		463.1	± 4.7	
CHU179-04.1	0.00	191	148	0.80	12.75	± 0.17	0.0573	± 0.0019		486.9	± 6.1		486.6	± 6.2	
CHU179-04.2	0.48	95	48	0.52	13.27	± 0.20	0.0539	± 0.0044		468.2	± 6.9		469.6	± 6.9	
CHU179-05.1	0.01	201	127	0.65	12.90	± 0.16	0.0578	± 0.0030		481.2	± 5.7		480.6	± 5.6	
CHU179-05.2	0.00	102	47	0.48	13.34	± 0.18	0.0588	± 0.0030		465.8	± 6.0		464.5	± 6.2	
CHU179-06	0.08	154	90	0.60	12.39	± 0.19	0.0580	± 0.0036		500.2	± 7.4		499.7	± 7.4	
CHU179-07#	0.13	127	55	0.44	13.00	± 0.20	0.0641	± 0.0037		477.9	± 7.0		473.7	± 7.0	
CHU179-08	1.05	91	42	0.47	13.52	± 0.25	0.0540	± 0.0050		459.9	± 8.3		461.2	± 8.3	
CHU179-09	0.08	214	133	0.64	12.94	± 0.15	0.0589	± 0.0033		479.8	± 5.3		478.6	± 5.3	
CHU179-10	0.30	188	125	0.68	13.43	± 0.20	0.0573	± 0.0036		462.9	± 6.7		462.4	± 6.6	
CHU179-11	0.00	173	96	0.57	12.94	± 0.17	0.0594	± 0.0022		480.0	± 6.2		478.4	± 6.3	
CHU179-12	0.00	208	124	0.61	12.90	± 0.19	0.0569	± 0.0020		481.5	± 6.9		481.4	± 7.0	
CHU179-13	0.00	130	62	0.49	12.36	± 0.18	0.0620	± 0.0026		501.4	± 7.1		498.6	± 7.2	
CHU179-14	0.00	137	93	0.70	12.80	± 0.22	0.0565	± 0.0026		485.0	± 8.1		485.0	± 8.1	
CHU179-15	2.14	266	144	0.56	12.81	± 0.17	0.0515	± 0.0041		484.7	± 6.2		487.9	± 6.1	
CHU179-16	0.00	282	210	0.76	13.03	± 0.15	0.0550	± 0.0018		476.8	± 5.2		476.8	± 5.2	
CHU179-17	0.00	247	163	0.68	13.01	± 0.17	0.0592	± 0.0017		477.4	± 6.0		476.0	± 6.0	
CHU179-18#	0.00	264	193	0.75	12.35	± 0.13	0.0635	± 0.0019		501.8	± 5.0		498.1	± 5.1	
CHU179-19	0.14	255	128	0.52	12.75	± 0.15	0.0553	± 0.0028		486.6	± 5.5		487.3	± 5.4	
CHU179-20	0.00	175	124	0.73	11.34	± 0.20	0.0559	± 0.0019		544.9	± 9.4		544.9	± 9.4	
CHU179-21	0.63	184	94	0.53	13.27	± 0.19	0.0580	± 0.0037		468.4	± 6.5		467.5	± 6.5	



CHU179-22	0.11	90	45	0.51	13.20	±	0.27	0.0595	±	0.0049	470.8	±	9.4	469.1	±	9.4
CHU179-23	0.58	106	53	0.51	12.14	±	0.23	0.0549	±	0.0045	510.1	±	9.2	511.7	±	9.2
CHU180-01	0.00	102	71	0.72	12.47	±	0.22	0.0582	±	0.0024	497.2	±	8.5	496.6	±	8.6
CHU180-02	0.00	88	47	0.54	12.87	±	0.22	0.0539	±	0.0030	482.4	±	7.8	482.4	±	7.8
CHU180-03#	0.95	177	97	0.56	12.91	±	0.17	0.0641	±	0.0036	480.9	±	6.2	476.7	±	6.2
CHU180-04	0.79	444	356	0.82	13.01	±	0.16	0.0598	±	0.0041	477.3	±	5.6	475.5	±	5.3
CHU180-05	0.00	144	87	0.62	13.03	±	0.20	0.0550	±	0.0021	476.8	±	6.9	476.8	±	6.9
CHU180-06	0.00	250	189	0.77	12.10	±	0.17	0.0600	±	0.0015	512.1	±	6.8	510.6	±	6.8
CHU180-07	0.00	106	52	0.50	12.57	±	0.21	0.0532	±	0.0026	493.5	±	7.8	493.5	±	7.8
CHU180-08.1	0.48	342	254	0.76	12.84	±	0.15	0.0581	±	0.0032	483.5	±	5.3	482.8	±	5.1
CHU180-08.2#	1.46	295	151	0.52	13.91	±	0.17	0.0693	±	0.0044	447.5	±	5.2	440.4	±	5.2
CHU180-09	0.00	182	92	0.52	12.64	±	0.18	0.0613	±	0.0024	490.8	±	6.7	488.3	±	6.8
CHU180-10.1#	0.00	260	163	0.64	13.29	±	0.15	0.0604	±	0.0016	467.8	±	5.3	465.6	±	5.3
CHU180-10.2#	3.57	314	253	0.83	13.93	±	0.18	0.0952	±	0.0056	446.9	±	5.6	426.2	±	5.3
CHU180-11.1	0.08	153	79	0.53	12.65	±	0.20	0.0574	±	0.0036	490.5	±	7.5	490.2	±	7.5
CHU180-11.2	0.00	179	143	0.82	12.98	±	0.19	0.0560	±	0.0018	478.3	±	6.6	478.3	±	6.6
CHU180-12	0.40	102	52	0.52	12.65	±	0.20	0.0507	±	0.0046	490.4	±	7.6	492.3	±	7.4
CHU180-13	0.00	100	51	0.52	12.44	±	0.20	0.0589	±	0.0029	498.5	±	7.7	497.5	±	7.9
CHU180-14	0.28	290	174	0.61	13.02	±	0.16	0.0593	±	0.0027	476.9	±	5.6	475.4	±	5.6
CHU180-15	0.23	61	26	0.44	12.52	±	0.28	0.0583	±	0.0057	495.4	±	10.6	494.7	±	10.5
CHU180-16	0.00	156	109	0.71	12.76	±	0.19	0.0553	±	0.0021	486.5	±	7.0	486.5	±	7.0
CHU180-17	0.00	126	96	0.78	12.71	±	0.18	0.0597	±	0.0023	488.4	±	6.7	486.8	±	6.8
CHU180-18.1	0.42	281	254	0.93	12.77	±	0.16	0.0633	±	0.0046	486.1	±	5.9	482.4	±	5.5
CHU180-18.2	0.00	234	139	0.61	12.75	±	0.17	0.0594	±	0.0038	486.7	±	6.3	485.3	±	6.1
CHU180-19	0.00	128	68	0.55	12.76	±	0.18	0.0619	±	0.0027	486.5	±	6.8	483.6	±	6.9
CHU180-20	0.56	114	68	0.61	13.04	±	0.23	0.0545	±	0.0046	476.4	±	8.2	477.6	±	8.1
CHU228-01.1	0.13	193	105	0.56	12.79	±	0.19	0.0578	±	0.0030	485.1	±	6.8	484.6	±	6.8
CHU228-01.2	0.43	532	231	0.45	12.94	±	0.14	0.0589	±	0.0020	479.7	±	5.0	478.5	±	5.0

CHU228-02	0.00	121	70	0.60	12.62	±	0.18	0.0554	±	0.0023	491.5	±	6.9	491.5	±	6.9
CHU228-03.1	0.53	173	125	0.74	13.18	±	0.19	0.0541	±	0.0043	471.4	±	6.5	472.7	±	6.3
CHU228-03.2#	0.00	197	115	0.60	12.60	±	0.17	0.0619	±	0.0020	492.4	±	6.3	489.5	±	6.3
CHU228-04	0.62	534	254	0.49	13.24	±	0.13	0.0560	±	0.0021	469.5	±	4.4	469.8	±	4.4
CHU228-05	0.60	299	222	0.76	13.39	±	0.17	0.0541	±	0.0029	464.2	±	5.6	465.5	±	5.5
CHU228-06.1	0.00	264	155	0.60	12.61	±	0.17	0.0586	±	0.0018	492.1	±	6.3	491.1	±	6.4
CHU228-06.2#	0.00	243	103	0.43	12.92	±	0.18	0.0611	±	0.0017	480.4	±	6.5	477.9	±	6.5
CHU228-07.1	1.81	313	179	0.59	12.75	±	0.17	0.0615	±	0.0047	486.9	±	6.1	484.3	±	6.1
CHU228-07.2	0.00	404	183	0.46	12.96	±	0.13	0.0587	±	0.0016	479.2	±	4.8	478.0	±	4.9
CHU228-08.1	0.15	299	62	0.21	12.51	±	0.19	0.0596	±	0.0018	495.8	±	7.1	494.3	±	7.1
CHU228-08.2#	0.00	419	282	0.69	13.76	±	0.13	0.0640	±	0.0017	452.2	±	4.2	447.9	±	4.3
CHU228-09	0.08	226	138	0.62	12.25	±	0.18	0.0604	±	0.0034	506.0	±	7.3	504.2	±	7.2
CHU228-10	0.00	199	140	0.72	13.32	±	0.15	0.0575	±	0.0017	466.6	±	4.9	465.9	±	5.0
CHU228-11	0.00	264	113	0.44	12.71	±	0.15	0.0577	±	0.0019	488.2	±	5.4	487.7	±	5.5
CHU228-12.1#	0.00	347	144	0.42	13.09	±	0.15	0.0599	±	0.0014	474.7	±	5.3	472.8	±	5.3
CHU228-12.2#	0.13	469	264	0.58	13.81	±	0.15	0.0714	±	0.0026	450.8	±	4.8	442.5	±	4.7
CHU228-13	0.02	133	55	0.43	12.80	±	0.19	0.0537	±	0.0040	485.1	±	7.0	485.1	±	6.8
CHU228-14#	0.40	349	211	0.62	13.16	±	0.19	0.0678	±	0.0031	472.1	±	6.5	465.8	±	6.4
CHU228-15	2.55	197	120	0.62	11.53	±	0.24	0.0777	±	0.0100	536.3	±	10.9	524.2	±	10.3
CHU228-16	0.78	207	110	0.55	12.94	±	0.17	0.0527	±	0.0034	480.0	±	6.2	482.3	±	6.2
CHU228-17	0.10	193	133	0.70	12.92	±	0.17	0.0592	±	0.0036	480.7	±	5.9	479.3	±	5.8
CHU228-18#	0.07	414	205	0.51	12.72	±	0.19	0.0629	±	0.0029	487.9	±	6.9	484.5	±	6.8
CHU228-19#	0.00	197	118	0.61	13.00	±	0.17	0.0612	±	0.0021	477.6	±	6.0	475.0	±	6.1
CHU228-20	0.00	109	59	0.55	13.00	±	0.20	0.0565	±	0.0027	477.9	±	7.2	477.9	±	7.2
CHU228-21	0.08	274	175	0.65	13.02	±	0.16	0.0592	±	0.0032	477.0	±	5.7	475.5	±	5.6
BT004-1	0.00	174	68	0.40	12.51	±	0.16	0.0555	±	0.0012	495.6	±	5.9	495.6	±	5.9
BT004-2	1.23	83	43	0.54	12.68	±	0.20	0.0569	±	0.0058	489.3	±	7.4	489.4	±	7.2
BT004-3	0.14	294	241	0.84	12.57	±	0.16	0.0552	±	0.0029	493.4	±	6.0	494.1	±	5.8

BT004-4	0.00	217	121	0.57	12.54	±	0.15	0.0590	±	0.0012	494.6	±	5.7	493.4	±	5.7
BT004-5	0.00	161	107	0.68	13.02	±	0.16	0.0593	±	0.0016	476.9	±	5.5	475.4	±	5.6
BT004-6.1	0.00	237	105	0.46	12.65	±	0.13	0.0569	±	0.0013	490.4	±	5.0	490.4	±	5.0
BT004-6.2	0.10	120	56	0.48	12.53	±	0.18	0.0586	±	0.0035	494.8	±	6.7	493.9	±	6.6
BT004-7	0.00	207	108	0.54	12.73	±	0.15	0.0548	±	0.0014	487.5	±	5.5	487.5	±	5.5
BT004-8	0.00	97	47	0.50	12.59	±	0.17	0.0649	±	0.0024	492.6	±	6.2	488.0	±	6.3
BT004-9	0.22	103	52	0.52	11.90	±	0.15	0.0550	±	0.0032	520.0	±	6.4	521.1	±	6.3
BT004-10	0.00	314	205	0.67	12.86	±	0.14	0.0581	±	0.0010	482.6	±	5.0	481.8	±	5.0
BT004-11	0.00	116	49	0.44	12.62	±	0.17	0.0574	±	0.0017	491.5	±	6.3	491.3	±	6.4
BT004-12	0.00	202	144	0.73	12.68	±	0.13	0.0558	±	0.0014	489.4	±	5.0	489.4	±	5.0
BT004-13	0.00	138	95	0.71	12.79	±	0.14	0.0557	±	0.0016	485.5	±	5.2	485.5	±	5.2
BT004-14	0.00	121	55	0.46	12.36	±	0.17	0.0577	±	0.0018	501.5	±	6.7	501.2	±	6.8
BT004-15	0.00	104	49	0.49	12.80	±	0.16	0.0550	±	0.0019	485.0	±	5.7	485.0	±	5.7
BT004-16	0.00	241	152	0.65	12.15	±	0.15	0.0567	±	0.0011	509.8	±	6.2	509.8	±	6.2
BT004-17.1	0.22	347	225	0.66	13.01	±	0.15	0.0564	±	0.0021	477.3	±	5.4	477.4	±	5.3
BT004-17.2	0.00	124	55	0.45	12.99	±	0.18	0.0549	±	0.0018	477.9	±	6.3	477.9	±	6.3
BT004-18	0.00	187	126	0.69	12.85	±	0.15	0.0569	±	0.0014	483.0	±	5.5	482.9	±	5.6
BT004-19.1	0.78	357	241	0.69	13.21	±	0.14	0.0573	±	0.0029	470.5	±	4.9	470.1	±	4.8
BT004-19.2	0.73	182	93	0.52	12.89	±	0.17	0.0569	±	0.0030	481.6	±	6.0	481.6	±	5.9
BT004-20	0.07	120	87	0.75	12.66	±	0.15	0.0629	±	0.0042	489.9	±	5.6	486.4	±	5.3
BT004-21#	0.00	102	50	0.50	13.07	±	0.17	0.0628	±	0.0020	475.3	±	5.9	471.8	±	6.0
BT004-22	0.00	208	134	0.66	12.89	±	0.15	0.0597	±	0.0015	481.7	±	5.2	480.0	±	5.3
BT004-23	0.22	280	155	0.57	12.76	±	0.13	0.0548	±	0.0020	486.4	±	4.7	487.4	±	4.6
BT004-24	0.00	89	38	0.43	13.02	±	0.17	0.0595	±	0.0020	477.1	±	5.9	475.5	±	6.0
BT006-1	0.00	300	250	0.86	12.83	±	0.14	0.0578	±	0.0011	483.8	±	5.1	483.2	±	5.2
BT006-2	0.00	95	48	0.52	12.85	±	0.19	0.0566	±	0.0018	483.1	±	6.9	483.1	±	6.9
BT006-3#	0.00	196	91	0.48	12.77	±	0.14	0.0598	±	0.0014	485.9	±	5.2	484.2	±	5.2
BT006-4	0.00	126	57	0.46	12.72	±	0.14	0.0606	±	0.0022	487.9	±	5.1	485.8	±	5.3

BT006-5	0.09	215	98	0.47	12.90	±	0.15	0.0577	±	0.0023	481.4	±	5.3	480.8	±	5.2
BT006-6	0.00	159	79	0.51	12.18	±	0.13	0.0554	±	0.0015	508.5	±	5.3	508.5	±	5.3
BT006-7	0.09	269	121	0.46	12.76	±	0.13	0.0578	±	0.0021	486.3	±	4.7	485.8	±	4.7
BT006-8	0.00	225	125	0.57	12.91	±	0.14	0.0556	±	0.0014	481.1	±	5.1	481.1	±	5.1
BT006-9	0.17	92	43	0.48	12.80	±	0.19	0.0585	±	0.0031	485.0	±	6.9	484.1	±	6.9
BT006-10	0.20	96	49	0.52	13.05	±	0.18	0.0592	±	0.0030	476.1	±	6.4	474.6	±	6.4
BT006-11	0.19	92	49	0.55	12.82	±	0.20	0.0559	±	0.0034	484.3	±	7.4	484.8	±	7.3
BT006-12	0.02	162	71	0.45	12.70	±	0.15	0.0586	±	0.0024	488.5	±	5.6	487.5	±	5.6
BT006-13	0.29	94	50	0.54	13.03	±	0.18	0.0562	±	0.0029	476.5	±	6.2	476.8	±	6.2
BT006-14	0.00	181	106	0.60	13.33	±	0.14	0.0569	±	0.0016	466.3	±	4.6	466.0	±	4.6
BT006-15	0.00	171	109	0.65	12.67	±	0.16	0.0545	±	0.0015	489.8	±	6.0	489.8	±	6.0
BT006-16.1	0.00	179	128	0.73	12.58	±	0.16	0.0579	±	0.0014	492.9	±	5.9	492.4	±	5.9
BT006-16.2	0.00	154	71	0.47	12.67	±	0.16	0.0570	±	0.0015	489.8	±	6.0	489.7	±	6.0
BT006-17	0.16	99	56	0.58	12.63	±	0.19	0.0524	±	0.0033	491.3	±	7.0	492.0	±	6.9
BT006-18	0.00	136	102	0.77	12.58	±	0.16	0.0545	±	0.0018	493.2	±	5.9	493.2	±	5.9
BT006-19	0.00	135	82	0.62	12.28	±	0.16	0.0574	±	0.0017	504.9	±	6.3	504.9	±	6.3
BT006-20	0.00	178	104	0.60	12.60	±	0.14	0.0570	±	0.0016	492.4	±	5.1	492.4	±	5.2
BT006-21	0.01	79	31	0.41	12.49	±	0.19	0.0542	±	0.0031	496.5	±	7.3	496.6	±	7.2
BT006-22	0.00	76	38	0.51	12.77	±	0.17	0.0549	±	0.0022	486.1	±	6.3	486.1	±	6.3
BT006-23	0.00	164	88	0.55	12.46	±	0.17	0.0567	±	0.0018	497.8	±	6.4	497.8	±	6.4
BT006-24	0.00	193	99	0.53	12.26	±	0.13	0.0562	±	0.0014	505.5	±	5.1	505.5	±	5.1
BT011-1.1	0.45	103	44	0.44	13.01	±	0.18	0.0569	±	0.0030	477.2	±	6.4	477.1	±	6.4
BT011-1.2	0.25	109	51	0.47	13.00	±	0.18	0.0543	±	0.0032	477.8	±	6.5	478.9	±	6.3
BT011-1.3	0.23	126	54	0.44	12.87	±	0.15	0.0565	±	0.0027	482.2	±	5.5	482.4	±	5.4
BT011-2.1#	0.00	180	141	0.80	12.83	±	0.14	0.0601	±	0.0015	483.7	±	4.9	481.8	±	5.0
BT011-2.2	3.30	141	98	0.71	13.15	±	0.16	0.0548	±	0.0043	472.6	±	5.7	473.8	±	5.6
BT011-2.3#	0.00	207	97	0.48	13.47	±	0.14	0.0595	±	0.0016	461.5	±	4.5	459.7	±	4.6
BT011-3	0.21	93	46	0.51	12.78	±	0.18	0.0542	±	0.0037	485.6	±	6.4	486.6	±	6.2

BT011-4	0.10	107	56	0.54	12.23	±	0.19	0.0554	±	0.0031	506.6	±	7.8	507.1	±	7.6
BT011-5.1	0.00	260	212	0.84	12.68	±	0.14	0.0564	±	0.0012	489.4	±	5.3	489.4	±	5.3
BT011-5.2	0.00	136	62	0.47	12.56	±	0.17	0.0566	±	0.0019	493.7	±	6.6	493.7	±	6.6
BT011-6.1	0.00	103	58	0.58	12.60	±	0.17	0.0563	±	0.0017	492.5	±	6.5	492.5	±	6.5
BT011-6.2	0.18	139	101	0.74	13.12	±	0.17	0.0557	±	0.0031	473.5	±	5.8	474.0	±	5.7
BT011-7.1	0.00	148	84	0.58	12.96	±	0.17	0.0599	±	0.0017	479.1	±	6.0	477.3	±	6.0
BT011-7.2	0.00	141	61	0.44	13.09	±	0.17	0.0575	±	0.0016	474.5	±	6.0	474.0	±	6.1
BT012-1#	0.00	105	52	0.51	12.85	±	0.18	0.0614	±	0.0021	482.9	±	6.5	480.3	±	6.6
BT012-2	0.02	100	43	0.44	12.93	±	0.18	0.0579	±	0.0032	480.3	±	6.4	479.6	±	6.4
BT012-3	0.06	222	115	0.53	13.31	±	0.13	0.0602	±	0.0023	467.2	±	4.4	465.0	±	4.3
BT012-4	0.00	147	79	0.55	12.93	±	0.16	0.0588	±	0.0017	480.3	±	5.8	479.1	±	5.8
BT012-5	0.00	507	561	1.14	13.10	±	0.12	0.0583	±	0.0011	474.3	±	4.1	473.3	±	4.2
BT012-6	0.00	138	101	0.76	12.91	±	0.14	0.0585	±	0.0016	480.8	±	5.0	479.8	±	5.1
BT012-7	2.44	114	57	0.52	13.24	±	0.19	0.0541	±	0.0051	469.4	±	6.5	470.8	±	6.5
BT012-8	0.12	134	69	0.53	12.53	±	0.16	0.0550	±	0.0029	494.9	±	6.1	495.5	±	6.0
BT012-9	0.25	95	45	0.49	13.13	±	0.17	0.0542	±	0.0036	473.2	±	5.9	474.3	±	5.7
BT012-10	0.00	77	35	0.47	13.08	±	0.20	0.0539	±	0.0022	475.0	±	7.0	475.0	±	7.0
BT012-11	0.96	164	112	0.70	12.75	±	0.16	0.0531	±	0.0029	486.6	±	5.9	488.8	±	5.8
BT012-12	0.55	96	50	0.54	12.72	±	0.16	0.0589	±	0.0041	487.9	±	6.1	486.8	±	5.9
BT012-13	0.00	277	219	0.81	12.65	±	0.12	0.0572	±	0.0012	490.5	±	4.5	490.4	±	4.6
BT012-14	0.77	80	48	0.61	13.02	±	0.19	0.0543	±	0.0050	477.1	±	6.8	478.4	±	6.6
BT012-15	0.65	104	51	0.50	12.78	±	0.17	0.0502	±	0.0035	485.5	±	6.2	488.6	±	6.1
BT012-16	0.00	101	57	0.58	13.09	±	0.16	0.0563	±	0.0016	474.7	±	5.7	474.7	±	5.7
BT012-17	0.16	123	57	0.48	12.84	±	0.17	0.0519	±	0.0025	483.4	±	6.2	484.1	±	6.1
BT012-18	0.00	109	50	0.47	13.03	±	0.17	0.0553	±	0.0027	476.7	±	6.0	476.7	±	5.9
BT012-19	0.00	91	45	0.50	12.54	±	0.19	0.0595	±	0.0020	494.4	±	7.3	493.0	±	7.4
BT012-20	0.00	195	106	0.56	12.50	±	0.15	0.0568	±	0.0012	496.2	±	5.8	496.2	±	5.8
BT012-21	0.00	96	50	0.53	12.76	±	0.17	0.0562	±	0.0019	486.4	±	6.2	486.4	±	6.2

BT012-22	0.02	122	61	0.51	13.15	±	0.18	0.0557	±	0.0028	472.5	±	6.3	472.6	±	6.2
BT012-23	0.00	218	127	0.60	12.87	±	0.16	0.0588	±	0.0013	482.3	±	5.6	481.1	±	5.6
BT012-24	0.22	103	47	0.47	13.08	±	0.20	0.0544	±	0.0032	475.1	±	6.9	476.1	±	6.8
BT012-25	0.30	99	62	0.64	13.00	±	0.19	0.0547	±	0.0035	477.7	±	6.9	478.8	±	6.8
BT012-26	0.00	124	52	0.43	12.83	±	0.18	0.0592	±	0.0018	483.8	±	6.6	482.5	±	6.6
BT012-27	2.12	114	58	0.52	13.40	±	0.18	0.0487	±	0.0065	464.1	±	5.9	468.4	±	5.7
BT015-1.1	0.00	110	53	0.50	12.55	±	0.16	0.0595	±	0.0021	494.2	±	6.1	492.7	±	6.2
BT015-1.2	0.77	97	44	0.46	13.07	±	0.17	0.0531	±	0.0035	475.4	±	6.0	477.5	±	6.0
BT015-2	0.00	135	77	0.58	12.93	±	0.16	0.0595	±	0.0021	480.3	±	5.8	478.7	±	5.9
BT015-3.1	0.00	144	82	0.58	12.06	±	0.14	0.0596	±	0.0018	513.6	±	5.9	512.3	±	5.9
BT015-3.2	0.00	93	50	0.55	12.81	±	0.17	0.0594	±	0.0021	484.7	±	6.4	483.2	±	6.5
BT015-4.1	0.00	196	130	0.68	12.79	±	0.15	0.0579	±	0.0015	485.2	±	5.5	484.6	±	5.6
BT015-4.2	0.00	299	182	0.62	12.72	±	0.13	0.0554	±	0.0011	487.8	±	4.6	487.8	±	4.6
BT015-5.1	0.00	200	146	0.75	12.85	±	0.14	0.0559	±	0.0015	483.0	±	5.1	483.0	±	5.1
BT015-5.2	0.00	80	45	0.58	12.72	±	0.19	0.0586	±	0.0026	487.8	±	7.0	486.8	±	7.1
BT015-6	0.00	216	140	0.66	12.42	±	0.14	0.0554	±	0.0014	499.1	±	5.5	499.1	±	5.5
BT015-7	0.00	232	121	0.54	12.66	±	0.12	0.0583	±	0.0014	490.0	±	4.5	489.2	±	4.6
BT015-8	0.34	115	75	0.67	12.75	±	0.12	0.0591	±	0.0032	486.7	±	4.4	485.4	±	4.3
BT015-9.1	0.00	99	49	0.51	12.90	±	0.17	0.0570	±	0.0019	481.3	±	6.2	481.2	±	6.2
BT015-9.2#	0.00	104	53	0.52	12.98	±	0.16	0.0615	±	0.0020	478.4	±	5.5	475.7	±	5.6
BT015-10.1	0.31	107	73	0.69	12.58	±	0.19	0.0533	±	0.0032	492.9	±	7.1	494.4	±	7.0
BT015-10.2	0.00	78	34	0.44	13.01	±	0.20	0.0563	±	0.0023	477.3	±	6.9	477.3	±	6.9
BT015-11.1	0.00	94	43	0.47	12.82	±	0.15	0.0557	±	0.0019	484.1	±	5.6	484.1	±	5.6
BT015-11.2#	0.00	310	225	0.74	13.23	±	0.14	0.0597	±	0.0012	469.6	±	4.8	467.8	±	4.8
BT015-12	0.26	149	103	0.70	12.43	±	0.15	0.0569	±	0.0030	499.0	±	6.0	499.1	±	5.8
BT015-13.1	0.10	113	61	0.55	12.45	±	0.21	0.0567	±	0.0031	497.9	±	7.9	498.2	±	7.8
BT015-13.2	0.00	97	45	0.48	12.66	±	0.17	0.0585	±	0.0019	490.1	±	6.5	489.2	±	6.6
BT015-14	1.42	261	160	0.63	12.88	±	0.17	0.0620	±	0.0041	482.1	±	6.2	479.2	±	6.1

BT015-15.1	0.00	109	80	0.75	12.74	±	0.18	0.0584	±	0.0018	487.0	±	6.5	486.1	±	6.5
BT015-15.2	0.31	99	54	0.56	13.09	±	0.16	0.0576	±	0.0037	474.6	±	5.6	474.1	±	5.5
BT016-1	0.00	111	65	0.61	12.81	±	0.16	0.0568	±	0.0020	484.5	±	5.7	484.5	±	5.7
BT016-2.1	2.68	96	38	0.41	12.50	±	0.23	0.0586	±	0.0050	496.1	±	8.7	495.4	±	8.7
BT016-2.2	0.01	87	28	0.34	12.32	±	0.18	0.0568	±	0.0028	503.1	±	7.1	503.1	±	7.0
BT016-3	0.00	150	73	0.50	13.22	±	0.15	0.0564	±	0.0015	470.1	±	5.3	470.1	±	5.3
BT016-4.1	0.00	203	147	0.74	12.63	±	0.14	0.0542	±	0.0014	491.0	±	5.4	491.0	±	5.4
BT016-4.2	1.23	247	161	0.67	12.88	±	0.14	0.0572	±	0.0035	482.0	±	5.2	481.9	±	5.1
BT016-5.1	0.64	264	192	0.75	13.59	±	0.13	0.0604	±	0.0026	457.8	±	4.3	455.5	±	4.2
BT016-5.2	0.51	238	127	0.55	13.65	±	0.12	0.0583	±	0.0026	455.8	±	4.0	454.6	±	3.9
BT016-6.1	0.18	120	70	0.60	12.85	±	0.19	0.0555	±	0.0033	482.9	±	7.0	483.7	±	6.9
BT016-6.2#	0.00	155	132	0.87	12.33	±	0.14	0.0660	±	0.0017	502.6	±	5.4	497.4	±	5.5
BT016-7.1	0.38	117	53	0.47	12.78	±	0.18	0.0542	±	0.0028	485.5	±	6.5	487.0	±	6.5
BT016-7.2	0.48	88	40	0.47	12.96	±	0.19	0.0532	±	0.0037	479.3	±	6.9	481.4	±	6.9
BT016-8	0.00	93	51	0.56	12.70	±	0.19	0.0563	±	0.0020	488.5	±	6.9	488.5	±	6.9
BT016-9#	0.00	180	127	0.72	12.68	±	0.16	0.0614	±	0.0017	489.3	±	5.9	486.7	±	6.0
BT016-10#	0.00	146	77	0.54	12.66	±	0.15	0.0539	±	0.0012	489.9	±	5.7	489.9	±	5.7
BT016-11	0.46	83	41	0.51	12.72	±	0.20	0.0593	±	0.0038	487.9	±	7.5	486.6	±	7.4
BT016-12	0.00	161	120	0.76	12.85	±	0.16	0.0571	±	0.0012	483.0	±	5.8	482.8	±	5.8
BT016-13	0.00	180	86	0.49	12.91	±	0.14	0.0580	±	0.0015	481.1	±	5.2	480.4	±	5.3
BT016-14	0.00	90	42	0.48	13.05	±	0.19	0.0563	±	0.0020	476.1	±	6.6	476.1	±	6.6
BT016-15	0.02	81	39	0.50	12.91	±	0.18	0.0604	±	0.0038	481.0	±	6.6	478.9	±	6.5
BT016-16#	0.00	165	124	0.77	13.26	±	0.17	0.0614	±	0.0021	468.9	±	5.8	466.1	±	5.9
BT016-17	0.00	129	96	0.77	12.96	±	0.19	0.0583	±	0.0018	479.1	±	6.8	478.2	±	6.8
BT016-18	0.06	203	105	0.53	12.64	±	0.18	0.0560	±	0.0022	491.0	±	6.6	491.2	±	6.5
BT016-19.1	0.00	242	168	0.71	13.33	±	0.14	0.0575	±	0.0011	466.2	±	4.7	465.5	±	4.7
BT016-19.2	0.00	114	63	0.57	12.97	±	0.19	0.0569	±	0.0016	478.7	±	6.8	478.5	±	6.8
BT016-20#	0.00	98	73	0.77	13.56	±	0.24	0.0666	±	0.0026	458.6	±	7.7	452.9	±	7.8

BT016-21	0.00	137	61	0.46	12.68	±	0.16	0.0569	±	0.0019	489.3	±	6.1	489.3	±	6.1
BT016-22.1	0.00	162	57	0.36	12.38	±	0.17	0.0569	±	0.0015	500.9	±	6.6	500.9	±	6.6
BT016-22.2	0.00	177	124	0.72	12.71	±	0.14	0.0582	±	0.0014	488.4	±	5.2	487.6	±	5.2
BT016-23	0.00	792	63	0.08	12.61	±	0.12	0.0578	±	0.0006	492.1	±	4.7	491.7	±	4.7
BT016-24	0.01	161	86	0.54	12.38	±	0.17	0.0589	±	0.0028	500.6	±	6.6	499.7	±	6.5
BT016-25	0.00	124	90	0.74	12.85	±	0.17	0.0601	±	0.0020	483.2	±	6.2	481.3	±	6.3
BT016-26	0.12	115	73	0.66	12.71	±	0.19	0.0567	±	0.0040	488.1	±	7.2	488.2	±	7.0
BT021-1.1	0.00	117	58	0.51	12.31	±	0.15	0.0575	±	0.0017	503.3	±	5.9	503.2	±	6.0
BT021-1.2	0.00	107	51	0.48	12.47	±	0.18	0.0566	±	0.0018	497.1	±	6.8	497.1	±	6.8
BT021-2	0.00	177	123	0.71	13.18	±	0.13	0.0563	±	0.0015	471.5	±	4.6	471.5	±	4.6
BT021-3	0.00	136	85	0.64	12.73	±	0.15	0.0555	±	0.0019	487.5	±	5.5	487.5	±	5.5
BT021-4	0.00	154	73	0.49	12.37	±	0.13	0.0560	±	0.0016	501.2	±	4.9	501.2	±	4.9
BT021-5	0.47	118	54	0.47	12.59	±	0.19	0.0531	±	0.0031	492.5	±	7.3	494.8	±	7.2
BT021-6	0.00	164	93	0.58	12.61	±	0.14	0.0578	±	0.0018	492.0	±	5.3	491.5	±	5.4
BT021-7	0.00	142	101	0.73	12.64	±	0.15	0.0576	±	0.0016	490.8	±	5.8	490.4	±	5.8
BT021-8	0.22	99	45	0.47	12.74	±	0.17	0.0554	±	0.0034	487.1	±	6.1	488.0	±	6.1
BT021-9	0.21	84	43	0.53	12.95	±	0.20	0.0549	±	0.0039	479.5	±	7.1	480.5	±	6.9
BT021-10#	0.00	186	131	0.73	12.96	±	0.14	0.0596	±	0.0014	479.0	±	4.9	477.4	±	4.9
BT021-11	0.00	204	112	0.56	12.63	±	0.16	0.0573	±	0.0014	491.2	±	6.0	491.0	±	6.0
BT021-12	0.08	108	59	0.56	12.73	±	0.18	0.0544	±	0.0030	487.4	±	6.6	487.7	±	6.5
BT021-13	0.00	192	140	0.75	12.73	±	0.14	0.0584	±	0.0014	487.4	±	5.3	486.5	±	5.4
BT021-14	0.11	124	82	0.67	12.57	±	0.17	0.0575	±	0.0032	493.3	±	6.3	493.0	±	6.2
BT021-15.1#	0.33	216	88	0.42	13.43	±	0.12	0.0610	±	0.0024	462.9	±	4.2	460.3	±	4.1
BT021-15.2	0.34	134	60	0.46	12.58	±	0.19	0.0575	±	0.0026	492.9	±	7.1	492.7	±	7.0
BT021-16	0.22	119	84	0.73	12.71	±	0.18	0.0554	±	0.0033	488.2	±	6.6	489.2	±	6.5
BT021-17	0.00	167	103	0.63	12.02	±	0.16	0.0581	±	0.0016	515.4	±	6.5	515.1	±	6.5
BT021-18	0.78	80	39	0.49	12.97	±	0.18	0.0547	±	0.0035	478.7	±	6.5	479.8	±	6.5
BT021-19	0.00	291	179	0.63	12.19	±	0.13	0.0589	±	0.0011	508.1	±	5.3	507.2	±	5.3



BT021-20	0.00	109	56	0.53	12.61	±	0.15	0.0556	±	0.0019	491.8	±	5.7	491.8	±	5.7
BT021-21.1	0.00	168	121	0.74	12.32	±	0.13	0.0563	±	0.0015	503.1	±	4.9	503.1	±	4.9
BT021-21.2	0.31	91	41	0.47	12.89	±	0.19	0.0577	±	0.0035	481.7	±	6.8	481.1	±	6.7
BT021-22	0.05	91	46	0.52	12.59	±	0.18	0.0579	±	0.0031	492.6	±	6.6	492.1	±	6.5
BT021-23	0.38	147	97	0.68	12.59	±	0.15	0.0550	±	0.0031	492.8	±	5.6	494.0	±	5.6
BT021-24	0.00	108	63	0.60	11.78	±	0.21	0.0596	±	0.0021	525.4	±	9.2	524.3	±	9.3

**Table 2.4.** Chemical composition of magnetite obtained by electron microprobe (EPMA) analyses at the Chandmani Uul deposit (in wt% oxide).

	Sample No.	Weight %															
		SiO <sub>2</sub>	TiO <sub>2</sub>	Al <sub>2</sub> O <sub>3</sub>	Cr <sub>2</sub> O <sub>3</sub>	V <sub>2</sub> O <sub>3</sub>	FeO*	MnO	MgO	CaO	ZnO	CuO	NiO	Total	Fe <sub>2</sub> O <sub>3</sub>	FeO	Total
Mushketovite	CHU130-1	2.59	0.04	0.82	0.02	0.01	88.92	0.00	0.24	0.61	0.10	0.08	0.00	93.43	64.59	30.81	99.90
	CHU130-2	1.69	0.00	0.29	0.01	0.01	91.29	0.03	0.10	0.32	0.06	0.07	0.00	93.85	66.82	31.17	100.55
	CHU130-3	0.14	0.00	0.03	0.00	0.02	92.54	0.00	0.00	0.00	0.10	0.07	0.00	92.90	64.27	34.71	99.34
	CHU130-4	0.03	0.00	0.03	0.00	0.01	93.18	0.01	0.01	0.00	0.06	0.02	0.00	93.36	64.69	34.97	99.84
	CHU130-5	2.08	0.03	0.52	0.06	0.00	89.56	0.08	0.21	0.44	0.07	0.05	0.00	93.10	62.75	33.10	99.39
	CHU130-6	0.17	0.00	0.03	0.00	0.00	93.29	0.02	0.00	0.00	0.05	0.08	0.03	93.67	64.79	34.99	100.16
	CHU130-7	0.11	0.00	0.03	0.00	0.03	92.99	0.02	0.02	0.00	0.04	0.07	0.00	93.31	64.59	34.87	99.78
	CHU134-1	0.13	0.01	0.00	0.00	0.05	93.75	0.01	0.00	0.00	0.04	0.00	0.01	94.00	65.16	35.12	100.53
	CHU134-2	0.07	0.00	0.02	0.00	0.02	93.40	0.00	0.03	0.00	0.07	0.02	0.00	93.61	64.84	35.05	100.11
	CHU134-3	0.09	0.00	0.03	0.00	0.02	93.20	0.02	0.00	0.00	0.03	0.08	0.06	93.53	64.69	34.99	100.01
	CHU134-4	1.79	0.04	0.36	0.00	0.00	91.05	0.05	0.11	0.31	0.03	0.05	0.00	93.80	63.81	33.64	100.20
	CHU134-5	1.83	0.07	0.37	0.00	0.01	91.57	0.01	0.08	0.25	0.02	0.02	0.00	94.21	64.32	33.69	100.65
	CHU136-11	2.66	0.11	0.81	0.03	0.02	89.70	0.04	0.24	0.62	0.04	0.03	0.00	94.28	63.13	32.89	100.60
	CHU136-12	0.54	0.01	0.10	0.00	0.01	93.23	0.00	0.03	0.00	0.00	0.05	0.00	93.96	64.99	34.75	100.48
	CHU136-13	1.94	0.03	0.31	0.02	0.00	91.16	0.06	0.16	0.28	0.02	0.05	0.00	94.02	63.90	33.66	100.41
	CHU136-14	3.02	0.10	0.96	0.00	0.01	88.52	0.08	0.25	0.73	0.00	0.03	0.00	93.69	62.43	32.35	99.95
	CHU136-15	0.20	0.03	0.07	0.04	0.03	93.36	0.01	0.00	0.00	0.00	0.01	0.01	93.76	64.98	34.89	100.27

	CHU136-16	2.21	0.08	0.66	0.04	0.00	90.16	0.04	0.09	0.37	0.00	0.03	0.01	93.69	63.52	33.00	100.05
	CHU136-17	2.60	0.09	0.90	0.00	0.02	88.85	0.02	0.15	0.59	0.00	0.04	0.00	93.25	62.68	32.45	99.53
Euhedral magnetite-1	CHU136-1	2.69	0.10	0.86	0.00	0.00	88.93	0.01	0.16	0.54	0.07	0.07	0.03	93.46	62.72	32.49	99.74
	CHU136-2	3.05	0.11	0.82	0.01	0.03	88.27	0.03	0.25	0.66	0.00	0.04	0.05	93.30	62.27	32.24	99.55
	CHU136-3	1.44	0.00	0.11	0.02	0.02	92.46	0.01	0.02	0.04	0.11	0.04	0.03	94.30	64.78	34.17	100.79
	CHU136-4	0.04	0.00	0.00	0.00	0.01	93.90	0.00	0.00	0.00	0.00	0.03	0.00	93.98	65.23	35.21	100.53
	CHU136-5	2.27	0.10	0.67	0.00	0.02	90.54	0.04	0.17	0.56	0.04	0.05	0.02	94.48	63.57	33.34	100.86
	CHU136-6	2.21	0.08	0.69	0.00	0.02	90.68	0.02	0.17	0.46	0.00	0.01	0.00	94.34	63.77	33.30	100.73
	CHU136-7	0.02	0.00	0.00	0.00	0.00	93.85	0.03	0.00	0.00	0.00	0.08	0.03	94.00	65.12	35.25	100.53
	CHU136-8	2.55	0.09	0.93	0.00	0.00	89.76	0.00	0.17	0.55	0.02	0.04	0.01	94.11	63.30	32.80	100.46
	CHU136-9	0.01	0.00	0.02	0.00	0.00	92.81	0.00	0.00	0.00	0.00	0.12	0.00	92.97	64.42	34.85	99.43
	CHU136-10	1.82	0.04	0.55	0.00	0.03	91.38	0.00	0.13	0.37	0.02	0.06	0.00	94.39	64.10	33.70	100.81

\* Total Fe as FeO, and is recalculated into FeO and Fe<sub>2</sub>O<sub>3</sub>.

**Table 2.4** (continue)

	Sample No.	Number of cations on the basis of 32O													
		Si	Ti	Al	Cr	V	Fe(III)	Fe(II)	Mn	Mg	Ca	Zn	Cu	Ni	Total
Mushketovite	CHU130-1	1.008	0.012	0.376	0.006	0.003	13.906	8.078	0.000	0.139	0.254	0.029	0.024	0.000	23.835
	CHU130-2	0.669	0.000	0.135	0.003	0.003	14.466	8.509	0.010	0.059	0.136	0.018	0.021	0.000	24.027
	CHU130-3	0.058	0.000	0.015	0.000	0.007	15.142	9.087	0.000	0.000	0.000	0.030	0.022	0.000	24.361
	CHU130-4	0.012	0.000	0.014	0.000	0.003	15.193	9.126	0.003	0.006	0.000	0.018	0.006	0.000	24.383
	CHU130-5	0.821	0.009	0.242	0.019	0.000	14.177	8.311	0.027	0.124	0.186	0.020	0.015	0.000	23.951
	CHU130-6	0.069	0.000	0.014	0.000	0.000	15.134	9.082	0.007	0.000	0.000	0.015	0.025	0.010	24.357
	CHU130-7	0.045	0.000	0.014	0.000	0.010	15.159	9.094	0.007	0.000	0.000	0.012	0.021	0.000	24.363
	CHU134-1	0.053	0.000	0.000	0.000	0.016	15.174	9.089	0.003	0.000	0.000	0.012	0.000	0.003	24.352
	CHU134-2	0.029	0.000	0.010	0.000	0.007	15.172	9.115	0.000	0.018	0.000	0.021	0.006	0.000	24.378
	CHU134-3	0.037	0.000	0.014	0.000	0.007	15.152	9.107	0.007	0.000	0.000	0.009	0.025	0.020	24.377
	CHU134-4	0.707	0.012	0.168	0.000	0.000	14.418	8.447	0.017	0.065	0.131	0.009	0.015	0.000	23.988
	CHU134-5	0.719	0.021	0.171	0.000	0.003	14.452	8.413	0.003	0.047	0.105	0.006	0.006	0.000	23.947
	CHU136-11	1.024	0.032	0.368	0.009	0.006	13.895	8.045	0.013	0.138	0.256	0.011	0.009	0.000	23.805
	CHU136-12	0.218	0.003	0.048	0.000	0.003	15.017	8.923	0.000	0.018	0.000	0.000	0.015	0.000	24.245
	CHU136-13	0.763	0.009	0.144	0.006	0.000	14.376	8.413	0.020	0.094	0.118	0.006	0.015	0.000	23.965
	CHU136-14	1.162	0.029	0.435	0.000	0.003	13.721	7.900	0.026	0.143	0.301	0.000	0.009	0.000	23.730
	CHU136-15	0.081	0.009	0.034	0.013	0.010	15.131	9.029	0.003	0.000	0.000	0.000	0.003	0.003	24.316
	CHU136-16	0.865	0.024	0.305	0.012	0.000	14.208	8.203	0.013	0.053	0.155	0.000	0.009	0.003	23.849
	CHU136-17	1.031	0.026	0.413	0.000	0.006	13.945	8.024	0.007	0.087	0.246	0.000	0.012	0.000	23.779

Euhedral magnetite-I	CHU136-1	1.045	0.029	0.394	0.000	0.000	13.918	8.014	0.003	0.093	0.225	0.020	0.021	0.009	23.770
	CHU136-2	1.179	0.032	0.374	0.003	0.009	13.754	7.913	0.010	0.144	0.273	0.000	0.012	0.016	23.719
	CHU136-3	0.571	0.000	0.051	0.006	0.006	14.705	8.619	0.003	0.012	0.017	0.032	0.012	0.010	24.044
	CHU136-4	0.016	0.000	0.000	0.000	0.003	15.217	9.128	0.000	0.000	0.000	0.000	0.009	0.000	24.374
	CHU136-5	0.880	0.029	0.306	0.000	0.006	14.085	8.210	0.013	0.098	0.232	0.011	0.015	0.006	23.893
	CHU136-6	0.858	0.023	0.316	0.000	0.006	14.159	8.215	0.007	0.098	0.191	0.000	0.003	0.000	23.878
	CHU136-7	0.008	0.000	0.000	0.000	0.000	15.197	9.143	0.010	0.000	0.000	0.000	0.025	0.010	24.393
	CHU136-8	0.985	0.026	0.423	0.000	0.000	13.968	8.045	0.000	0.098	0.228	0.006	0.012	0.003	23.793
	CHU136-9	0.004	0.000	0.010	0.000	0.000	15.201	9.139	0.000	0.000	0.000	0.000	0.037	0.000	24.391
	CHU136-10	0.712	0.012	0.254	0.000	0.009	14.347	8.383	0.000	0.076	0.155	0.006	0.018	0.000	23.971

**Table 2.5** Oxygen isotope values of minerals and those for ore-forming fluid.

Sample No.	Type of sample	Mineral	$\delta^{18}\text{O}$ (‰) of mineral	Temperature (°C)	$\delta^{18}\text{O}$ (‰) of water*
CHU112-1	Late vein	Quartz	12.9	Cau. Magnetite was cut by late-stage quartz vein	6.0
CHU112-2		Quartz	12.8		5.9
CHU112-5		Cau. Magnetite	2.6		10.7
CHU120-1	Type 3 ore	Mushketovite	-2.8		5.4
CHU120-2		Mushketovite	-0.3		7.8
CHU120-3		Mushketovite	-2.8		5.4
CHU120-4		Mushketovite	-2.5		5.7
CHU120-5		Mushketovite	-2.8		5.4
CHU120-6		Mushketovite	-3.1		5.1
CHU120-7		Mushketovite	1.2		9.4
CHU120-8		Mushketovite	-2.5		5.7
CHU122-2	Type 3 ore	Mushketovite	1.3		9.4
CHU122-4		Mushketovite	-0.4		7.8
CHU122-5		Mushketovite	2.2		10.4
CHU131-2	Type 3 ore	Epidote-1	4.5		4.0
CHU131-3		Epidote-1	4.8		4.3
CHU131-4		Epidote-1	4.4		3.9
CHU131-5		Epidote-1	4.5		4.0
CHU133-1	Type 3 ore	Mushketovite	-0.2		8.0

CHU133-3		Mushketovite	-2.9		5.3
CHU133-4		Mushketovite	1.7		9.8
CHU133-5		Mushketovite	-2.6		5.5
CHU133-6		Mushketovite	-2.3		5.8
CHU133-7		Mushketovite	-2.2		6.0
CHU133-8		Mushketovite	-3.1		5.1
CHU135-1		Mushketovite	-2.4		5.8
CHU135-2	Type 3 ore	Mushketovite	-3.3		4.9
CHU135-5		Mushketovite	-2.0		6.2
CHU135-7		Mushketovite	-0.1		8.0
CHU137-1		Quartz	10.4	Av. Quartz: 10.4‰	3.5
CHU137-6	Type 3 ore	Mushketovite	-3.8	Av. Mushketovite: - 4.4‰	4.4
CHU137-7		Mushketovite	-4.3	T: 310.8°C	3.9
CHU138-1		Epidote-1	4.3		3.9
CHU138-3		Epidote-1	4.7		4.2
CHU138-4	Host rock	Epidote-1	4.5		4.1
CHU138-5		Epidote-1	4.9		4.5
CHU138-7		Epidote-1	3.9		3.5
CHU138-8		Epidote-1	3.6		3.1
CHU146-2		Mushketovite	2.8		10.9
CHU146-3		Mushketovite	-0.7		7.5
CHU146-4		Mushketovite	1.9		10.1
CHU146-5	Type 3 ore	Mushketovite	0.9		9.1
CHU146-6		Mushketovite	0.5		8.7
CHU146-7		Mushketovite	-0.9		7.3
CHU146-8		Mushketovite	-0.5		7.7
CHU148-1	Type 3	Mushketovite	-1.4		6.8

CHU148-2		Mushketovite	-2.0		6.2
CHU148-3		Mushketovite	-1.5		6.7
CHU148-5		Mushketovite	-2.4		5.8
CHU148-6		Mushketovite	-2.2		6.0
CHU148-8		Mushketovite	-1.3		6.9
CHU150-8	Type 3 ore	Cau. Magnetite	-1.3		6.9
CHU156-2	Type 3 ore	Mushketovite	-2.8		5.4
CHU157-4	Type 3 ore	Mushketovite	-1.1		7.1
CHU158-1		Quartz	11.7		4.9
CHU158-5		Euh. Magnetite	-3.2		5.0
CHU158-6	Type 3 ore	Euh. Magnetite	-3.8	Av. Quartz: 11.7‰ Av. Euh.Magnetite: - 3.4‰ T: 298.7°C	4.4
CHU158-7		Euh. Magnetite	-3.6		4.6
CHU158-8		Euh. Magnetite	-3.1		5.1
CHU161-1		Quartz	11.6		4.7
CHU161-2		Quartz	11.6		4.7
CHU161-4		Mushketovite	-3.2		5.0
CHU161-5		Mushketovite	-3.7		4.4
CHU161-6	Type 3 ore	Mushketovite	-3.7	Av. Quartz: 11.6‰ Av. Mushketovite: - 3.5‰ T: 298.7°C	4.5
CHU161-7		Cau. Magnetite	-0.5		7.7
CHU161-8		Cau. Magnetite	-1.1		7.1
CHU161-9		Cau. Magnetite	0.2		8.4
CHU170-1	Type 3 ore	Quartz	10.6		3.7



CHU170-3		Quartz	12.5	Av. Quartz: 11.6‰ Av. Euh.Magnetite: - 3.0‰ T: 308.6°C	5.6
		Euh.			
CHU170-4		Magnetite	-2.9		5.3
		Euh.			
CHU170-5		Magnetite	-3.1		5.1
CHU218-1		Quartz	14.8	Av. Quartz: 14.7‰ Av. Mushketovite: - 5.6‰ T: 218.4°C	7.9
CHU218-2		Quartz	14.9		8.0
CHU218-4		Quartz	14.4		7.5
CHU218-5	Host rock	Mushketovite	-5.6		2.6
CHU218-6		Mushketovite	-5.4		2.8
CHU218-7		Mushketovite	-5.9		2.3
CHU218-8		Mushketovite	-5.4		2.8
CHU241-1		Epidote-2	6.6		6.2
CHU241-2		Epidote-2	6.2	Late vein	5.8
CHU241-4		Epidote-2	4.5		4.1
CHU241-6		Epidote-2	4.3		3.8
CHU241-7		Epidote-2	4.8		4.3
CHU241-8		Epidote-2	4.9		4.4

\* Calculated at T= 300°C; Mineral abbreviations: Euh.Mt-1, Euhedral magnetite-1; Euh.Mt-2, Euhedral magnetite-2; Mush, Mushketovite; Cau.Mt, Cauliflower magnetite; Q, Quartz; Epi-1, Epidote in alteration zone; Epi-2, Epidote in late vein.

**Table 2.6** Characteristics of IOCG mineralization of the Chandmani Uul deposit and major IOCG deposits in South America

IOCG sub-type	Ore deposit	Regional stress field	Related igneous rocks a) Igneous body b) Composition range c) Alkali-silica relationship d) Age	Wall rock alteration	Ore mineralogy	Source of ore-forming fluid	Reference
Hematite IOCG	Chandmani Uul Mongolia	In the stress field of Main Mongolian Lineament	a) Cambrian granitoids b) Diorite, granodiorite, and granite c) Sub-alkaline d) No age data	* Sericite * Sericite-chlorite * Epidote * Potassic	Mushketovite, magnetite with minor amount of chalcopyrite, pyrite	Magmatic water with significant contribution of meteoric components	This study
	Mantoverde Chile	Subsidiary segments of the related boundary-parallel Atacama fault system	a) Copiapó plutonic and Sierra Dieciocho plutonic complexes b) Diorite to quartzmonzonite c) Alkaline to sub-alkaline d) 127-97 Ma	* Sericite-chlorite * Potassic	Specular hematite, magnetite, chalcopyrite, pyrite, bornite	Magmatic water in early stages with incursion of a nonmagmatic fluid of meteoric or seawater origin in later stages	Benavides et al. (2007) Rieger et al. (2012)
	Alvo118 Brazil	In the Itacaunas shear belt	a) Estrela and Old Salobo granites b) Tonalite to monzogranite c) Sub-alkaline d) 2763-2573 Ma	* Quartz-sericite * Chlorite * Potassic * Sodic	Hematite, magnetite, chalcopyrite with chalcocite	Magmatic water, possibly with meteoric fluid contribution	Torresi et al. (2012)
Magnetite/hematite IOCG	Mina Justa Peru	In NW-SE trending Repetición and Mina Justa faults	a) Coastal batholith b) Monzonite to monzogranite c) No data d) 104-101 Ma	* Chlorite * Potassic * Sodic or sodic-calcic	Magnetite, mushketovite, pyrite, chalcopyrite, bornite, and chalcocite	Magmatic water is dominated in early mineralization stage, while basinal water related in later stages	Chen et al. (2010, 2011)

Magnetite IOCG	Candelaria Chile	In the stress field of Atacama fault zone	a) Copiapó pultonic complex b) Diorite, granodiorite, tonalite, monzodiorite, and quartzmonzonite c) Alkaline to sub-alkaline d) 119-97 Ma	* Chlorite * Potassic * Sodic or sodic- calcic	Magnetite, mushketovite, chalcopyrite, gold- rich electrum, and pyrite	Magmatic fluid	Oyarzún et al. (1999) Marschik and Fontbote (2001) Marschik et al. (2003)
	Salobo Brazil	In the Cinzento Transcurrent Share Zone	a) Old Salobo body b) Monzogranite to granodiorite c) Alkaline d) 2545-2537 Ma	*Silicification * Potassic * Sodic-calcic	Magnetite, bornite, chalcocite with minor chalcopyrite	Magmatic fluid	de Melo et al. (2017) de Melo et al. (2019) Marangoanha et al. (2019)
	Sossego Brazil	In NW-SE trending shear zone	a) Intrusive complex b) Gabbro, diabase, and acid intrusives c) No data d) >2.2 Ga	*Potassic * Chlorite * Sodic-calcic * Sodic	Magnetite, chalcopyrite, and pyrite	Formational and/or metamorphic fluid, possibly with magmatic fluid contribution	Monteiro et al. (2008)
	Marcona Peru	In NW-SE trending Repetición and Mina Justa faults	a) Andesitic magna b) Andesite and basaltic andesite c) No data d) 162-156 Ma	* Chlorite * Potassic * Sodic or sodic- calcic	Magnetite, pyrrhotite, pyrite with minor chalcopyrite	Magmatic water in early stage with involvement of seawater in later stage	Chen et al. (2010, 2011)

**Table 3.1** Chemical composition of garnet.

Sample No.	Wt %							Number of cations on the basis of 24O								Mole% of end member				
	SiO <sub>2</sub>	Al <sub>2</sub> O <sub>3</sub>	FeO	MnO	MgO	CaO	Total	Si	Al	Fe(III)	Fe(II)	Mn	Mg	Ca	Total	Prp	Alm	Sps	Grs	Adr
Garnet zone																				
1310-1	38.5	20.6	8.0	3.1	0.2	28.9	99.3	6.000	3.784	0.216	0.827	0.409	0.046	4.825	6.108	0.8	13.5	6.7	73.6	5.4
1310-3	37.8	20.5	9.0	5.3	0.3	27.0	99.9	5.921	3.784	0.295	0.884	0.703	0.070	4.531	6.187	1.1	14.3	11.4	65.8	7.4
1310-4	37.9	19.5	9.8	5.5	0.2	26.0	98.9	6.013	3.646	0.354	0.946	0.739	0.047	4.419	6.151	0.8	15.4	12.0	63.0	8.9
3244-1	38.9	20.4	4.2	0.7	0.2	35.7	100.1	5.965	3.687	0.348	0.190	0.091	0.046	5.865	6.192	0.7	3.1	1.5	86.0	8.7
3244-2	38.9	20.6	3.9	0.6	0.1	35.8	99.9	5.966	3.723	0.311	0.189	0.078	0.023	5.882	6.172	0.4	3.1	1.3	87.5	7.8
3244-5	38.9	21.1	4.3	0.9	0.2	35.6	101.0	5.913	3.780	0.308	0.239	0.116	0.045	5.797	6.197	0.7	3.9	1.9	85.9	7.7
3244-6	39.1	20.3	4.1	0.7	0.2	35.2	99.6	6.011	3.678	0.322	0.205	0.091	0.046	5.797	6.139	0.7	3.3	1.5	86.4	8.1
0617-1	39.0	18.3	5.4	1.4	0.4	34.8	99.3	6.081	3.363	0.637	0.067	0.185	0.093	5.813	6.157	1.5	1.1	3.0	78.5	15.9
0617-3	39.3	17.7	5.3	1.7	0.6	34.3	98.9	6.149	3.264	0.736	0.000	0.225	0.140	5.749	6.114	2.3	0.0	3.7	75.6	18.4
0617-4	39.1	18.7	5.3	1.7	0.5	34.6	99.9	6.056	3.414	0.586	0.100	0.223	0.115	5.742	6.180	1.9	1.6	3.6	78.2	14.7
0617-5	39.3	18.2	4.7	1.5	0.5	35.0	99.2	6.116	3.338	0.662	0.000	0.198	0.116	5.835	6.149	1.9	0.0	3.2	78.3	16.6
0617-6	38.8	18.0	5.1	1.7	0.5	34.7	98.8	6.085	3.327	0.673	0.000	0.226	0.117	5.830	6.172	1.9	0.0	3.7	77.6	16.8
0617-7	39.7	17.5	5.2	2.8	0.4	34.4	100.0	6.167	3.204	0.796	0.000	0.368	0.093	5.725	6.186	1.5	0.0	6.0	72.6	19.9
Vesuvianite-garnet zone																				
3298-1	37.6	20.0	11.4	4.6	0.0	25.6	99.2	5.953	3.740	0.307	1.204	0.622	0.012	4.340	6.177	0.2	19.5	10.1	62.6	7.7
3298-2	37.3	20.7	10.7	4.1	0.1	26.4	99.3	5.881	3.853	0.265	1.149	0.546	0.025	4.472	6.192	0.4	18.6	8.8	65.6	6.6
3298-4	38.0	20.1	11.6	3.9	0.1	26.5	100.2	5.961	3.707	0.332	1.185	0.522	0.030	4.448	6.185	0.5	19.2	8.4	63.6	8.3

3298-5	37.6	20.0	11.4	4.6	0.0	25.6	99.2	5.953	3.740	0.307	1.204	0.622	0.012	4.340	6.177	0.2	19.5	10.1	62.6	7.7
3298-6	37.3	20.7	10.7	4.1	0.1	26.4	99.3	5.881	3.853	0.265	1.149	0.546	0.025	4.472	6.192	0.4	18.6	8.8	65.6	6.6
0612-1	38.7	19.5	11.5	7.3	0.1	22.6	99.7	6.108	3.631	0.369	1.145	0.983	0.013	3.827	5.968	0.2	19.2	16.5	54.9	9.2
0612-2	37.8	20.0	12.5	10.5	0.1	18.4	99.3	6.045	3.770	0.230	1.438	1.417	0.022	3.148	6.025	0.4	23.9	23.5	46.5	5.7
0612-3	36.9	20.4	17.1	15.5	0.2	10.1	100.1	5.971	3.892	0.137	2.177	2.118	0.045	1.743	6.083	0.7	35.8	34.8	25.2	3.4
0612-4	37.5	19.9	13.0	11.2	0.1	17.5	99.3	6.021	3.760	0.240	1.512	1.529	0.028	3.009	6.077	0.5	24.9	25.2	43.5	6.0
Garnet-epidote zone																				
2169-1	37.4	20.4	14.3	12.6	0.1	14.7	99.5	6.004	3.868	0.132	1.783	1.713	0.032	2.529	6.058	0.5	29.4	28.3	38.5	3.3
2169-2	37.3	20.3	14.1	11.7	0.1	15.5	99.0	6.005	3.857	0.143	1.761	1.598	0.032	2.671	6.061	0.5	29.1	26.4	40.5	3.6
2169-3	37.3	20.0	13.8	13.7	0.1	14.1	99.0	6.030	3.812	0.188	1.680	1.879	0.035	2.440	6.034	0.6	27.8	31.1	35.7	4.7
2169-4	38.0	20.0	11.7	10.3	0.1	19.1	99.2	6.056	3.757	0.243	1.324	1.390	0.026	3.269	6.010	0.4	22.0	23.1	48.3	6.1
1510-1	38.2	18.1	14.6	12.2	0.6	16.6	100.3	6.128	3.422	0.578	1.380	1.657	0.143	2.853	6.034	2.4	22.9	27.5	32.8	14.5
1510-2	37.5	18.5	14.9	11.9	0.7	16.3	99.8	6.051	3.518	0.482	1.528	1.626	0.168	2.818	6.140	2.7	24.9	26.5	33.8	12.1
1510-3	37.8	18.4	14.2	13.5	0.7	15.0	99.6	6.107	3.503	0.497	1.422	1.847	0.169	2.596	6.034	2.8	23.6	30.6	30.6	12.4
1510-4	37.0	17.9	14.8	13.1	0.6	15.5	98.9	6.057	3.453	0.547	1.479	1.816	0.146	2.718	6.160	2.4	24.0	29.5	30.5	13.7
1510-7	37.3	17.9	14.4	13.8	0.7	14.8	98.9	6.095	3.447	0.553	1.415	1.910	0.171	2.591	6.086	2.8	23.2	31.4	28.8	13.8
1613-2	37.5	19.4	10.7	5.9	0.1	25.4	99.0	5.976	3.644	0.380	1.046	0.796	0.024	4.337	6.202	0.4	16.9	12.8	60.4	9.5
1613-3	37.4	19.9	11.7	6.1	0.1	24.1	99.3	5.948	3.730	0.321	1.235	0.822	0.024	4.107	6.186	0.4	20.0	13.3	58.3	8.0
1704-1	37.2	20.0	15.8	11.0	0.2	15.5	99.7	5.984	3.792	0.224	1.902	1.499	0.048	2.671	6.120	0.8	31.1	24.5	38.1	5.6
4963-1	38.9	18.8	11.2	5.5	0.1	24.5	99.0	6.164	3.511	0.489	0.995	0.738	0.024	4.159	5.916	0.4	16.8	12.5	58.1	12.2
4963-2	39.0	17.8	11.3	5.1	0.1	26.0	99.3	6.189	3.329	0.671	0.828	0.685	0.024	4.420	5.958	0.4	13.9	11.5	57.4	16.8

Mineral abbreviations: Prp, Pyrope; Alm, Almandine; Sps, Spessartine; Grs, Grossular, Adr, Andradite.

**Table 3.2** Chemical composition of clinopyroxene.

Sample No.	Wt%							Number of cations on the basis of 6O						Mole% of endmember		
	SiO <sub>2</sub>	Al <sub>2</sub> O <sub>3</sub>	FeO	MnO	MgO	CaO	Total	Si	Al	Fe	Mn	Mg	Ca	Diopside	Hedenbergite	Johannsenite
3244-10	51.7	0.1	13.9	0.6	8.8	24.4	99.5	2.002	0.005	0.450	0.020	0.508	1.012	51.9	46.0	2.0
3244-11	51.0	0.1	15.7	0.7	8.2	24.2	99.9	1.986	0.005	0.511	0.023	0.476	1.010	47.1	50.6	2.3
3244-12	52.3	0.1	12.3	0.7	9.9	24.5	99.8	2.003	0.005	0.394	0.023	0.565	1.005	57.5	40.1	2.3
3244-13	52.5	0.2	12.1	0.6	10.1	23.7	99.2	2.014	0.010	0.388	0.019	0.577	0.974	58.6	39.4	1.9
3244-14	50.6	0.2	11.8	0.8	11.3	25.1	99.8	1.948	0.009	0.380	0.026	0.648	1.035	61.5	36.1	2.5
3244-15	52.2	0.2	13.4	0.9	9.6	23.2	99.5	2.009	0.009	0.431	0.029	0.551	0.957	54.5	42.6	2.9
3244-16	51.3	0.1	14.6	1.4	7.7	24.3	99.4	2.003	0.005	0.477	0.046	0.448	1.016	46.1	49.1	4.7
3244-17	50.9	0.4	11.6	0.5	10.4	25.9	99.7	1.959	0.018	0.373	0.016	0.597	1.068	60.5	37.8	1.6
3244-18	52.7	0.2	11.0	0.5	10.7	24.0	99.1	2.014	0.010	0.351	0.007	0.609	0.982	63.0	36.3	0.7
3244-19	52.7	0.1	12.2	0.5	10.0	24.0	99.5	2.016	0.005	0.390	0.016	0.570	0.984	58.4	40.0	1.6
3244-20	52.1	0.1	12.6	0.7	9.8	23.7	99.0	2.010	0.005	0.406	0.023	0.564	0.980	56.8	40.9	2.3
0617-11	51.1	0.1	15.3	1.4	8.4	23.1	99.4	1.996	0.004	0.500	0.046	0.489	0.967	47.2	48.3	4.4
0617-12	51.7	0.2	13.2	0.6	10.1	23.6	99.4	1.993	0.009	0.426	0.020	0.580	0.975	56.5	41.5	1.9
0617-13	52.2	0.2	11.9	0.5	10.1	24.7	99.6	1.999	0.009	0.381	0.016	0.577	1.014	59.2	39.1	1.6
0617-14	52.6	0.2	11.8	0.5	10.4	23.8	99.3	2.012	0.009	0.377	0.016	0.593	0.975	60.1	38.2	1.6
0617-15	51.5	0.1	12.9	0.5	10.3	24.5	99.8	1.981	0.005	0.415	0.016	0.591	1.010	57.8	40.6	1.6
0617-16	52.1	0.2	12.0	0.5	11.1	23.9	99.8	1.989	0.009	0.383	0.016	0.632	0.978	61.3	37.1	1.6

**Table 3.3** Oxygen isotope values for minerals and skarn-forming fluid.

Sample No.	Oxygen isotopic value of mineral (‰)					Calculated oxygen isotopic value of water (‰)*			
	Garnet	Vesuvianite	Scheelite	Quartz	Muscovite	Garnet	Scheelite	Quartz	Muscovite
Garnet zone									
3244-1	7.1					9.0			
3244-2	7.7					9.5			
3244-3	4.5					6.4			
3244-4	4.9					6.7			
3244-5			1.0				2.4		
3244-6			1.3				2.7		
3244-11	5.5					7.3			
3244-12	4.9					6.8			
3244-13			0.6				2.0		
3244-14	4.4					6.2			
3244-15	5.9					7.7			
3244-16			2.4				3.8		
Vesuvianite-garnet zone									
3298-10	5.1					7.0			
3298-14		6.5							
3298-15	5.6					7.5			
3298-16		6.3							
3298-17		6.9							
3298-18	6.1					7.9			

3298-19	6.1			7.9	
3298-20		6.4			
3298-22	5.8			7.7	
3298-23			3.4		4.8
3298-26		5.9			
<hr/>					
Garnet-epidote zone					
2169a-2			1.1		2.5
2169a-3	5.7			7.6	
2169a-4	5.1			7.0	
2169a-5	5.7			7.6	
2169a-6	6.1			7.9	
2169a-7			0.4		1.8
2169a-9			1.1		2.6
2169a-10	5.8			7.7	
2169a-11			3.2		4.6
2169a-12			-0.3		1.2
2169a-13	6.0			7.8	
2169a-14	5.8			7.6	
2169a-15	5.9			7.7	
2169b-1	5.7			7.6	
2169b-2	5.8			7.7	
2169b-4			6.0		-1.3
2169b-6			6.6		-0.7
2169b-8				8.2	4.5
4963-1	6.1			8.0	
4963-2	5.6			7.4	



4963-3			10.9			3.6
4963-4			10.8			3.5
4963-5		1.6			3.1	
4963-6		1.9			3.3	
4963-7	5.7			7.5		
4963-8	5.4			7.2		
4963-9			10.7			3.4
4963-10			10.5			3.2
4963-11	5.8			7.7		
11452b-1	6.0			7.9		
11452b-3						
11452b-4						
11452b-5	6.0			7.9		
11452b-6	6.8			8.7		
11452b-8						
3300a-3			8.5			1.2
3300a-9			10.4			3.1
3300a-12		0.4			1.9	
3300a-14		1.1			2.6	
3300a-15	5.0			6.9		
3300b-2			10.5			3.2
3300b-3			10.3			3.0
3300b-5		1.8			3.2	
3300b-7	4.2			6.1		

---

\* Calculated at T= 288°C